The Hong Kong Polytechnic University

Department of Applied Physics

H_2 Sensors Made of Pd Films on Micro-Structured Templates and Supersonic Cluster Beam Deposited Oxide Films

ZHAO Meng

A thesis submitted in partial fulfillment of the requirements for the degree of Doctor of Philosophy

June 2012

CERTIFICATE OF ORIGINALITY

I hereby declare that this thesis is my own work and that, to the best of my knowledge and belief, it reproduces no material previously published or written, nor material that has been accepted for the award of any other degree or diploma, except where due acknowledgement has been made in the text.

_____(Signed)

ZHAO Meng (Name of student)

Abstract

Hydrogen (H_2) is widely used in industrial applications and renewable energy research. H_2 is a highly explosive gas, such that H_2 sensing technology is particularly envisaged for monitoring leakage and preventing explosion. From a thorough literature review, it was found that the performance of most commercialized H_2 sensors cannot reach the projected requirements for future applications. New sensor materials are needed to be developed to enhance the sensor response; shorten the response time; and improve selectivity for the detection of a target gas. They are also required to be miniaturizable.

In recent years, two types of H_2 sensors attract great attention. They are:

(i) Palladium- (Pd-) based sensors utilizing the H_2 induced lattice expansion (HILE) effect to close the structural discontinuity in the sensor to produce percolation-like resistance drop; and

(ii) Nano metal oxide (MO_x) sensors utilizing the large sensor area and porosity to achieve high sensor response and fast response rate.

However, difficulties were encountered in the development of both sensor types, which greatly hinder their practical applications. This project consists of the following three major parts with respective considerations to alleviate the problems.

The first part of the study is to fabricate and test a Pd-based HILE-type H_2

sensors designed to have the following features. (i) They have structural discontinuity in the form of isolation gaps with precisely controllable dimension, such that the sensors' performance is also controllable as a consequence. (ii) The Pd-based sensor elements were made on a compliant substrate, so that when the sensor element underwent a HILE process, the substrate can be deformed more readily to accelerate the sensor response. The compliance of the substrate also helps to release part of the stresses induced when reacting with H_2, such that the sensor's performance is more stable. (iii) The fabrication method employed was compatible to silicon-based micromachining technique, so that the sensor was miniaturizable and mass-producible. In practice, these ideas were realized by depositing a Pd film onto a single silicon (Si) pillar or a 2-dimensional Si pillar array, with the pillar(s) to have large height-to-thickness ratio up to 30. It was verified experimentally that the sensor response was controlled by tuning the dimension of the spacing around the pillars and the thickness of the Pd layer. The response time can be shorter than 1 s. The sensor output remains stable over quite many numbers of switching cycles. The sensors were produced with Si micromachining techniques and were demonstrated to be miniaturizable. Their sensor performance was compared with other existing HILE-type H_2 sensors. The effects of adding of a gold/chromium (Au/Cr) buffer layer for stabilizing the sensor structure, operation temperature and ambient gas on the H_2 sensing performance were also investigated.

The second part of the study was initiated by a finding from literatures. Many MO_x-based H_2 sensors were claimed to have nanostructures in terms of either having nano-sized gas sensing species or a highly porous structure. These two conditions are expected to facilitate achievements of stronger sensor response and faster response rate respectively, but no one single "nano" sensor type reported to date can satisfy all of them concomitantly. In our work, we solved this difficulty by using supersonic cluster beam deposition (SCBD) to produce Pd-coated nanocluster-assembled highly porous tungsten oxide films (Pd/SCBD WO_3). Structural analysis shows that an SCBD WO_3 film is constructed of loosely connected genuine WO_3 nanoclusters of 3–5 nm in diameter, and the film structure has a porosity as high as 66%. Therefore, the Pd/SCBD WO_3 film has a larger sensor response and shorter response time than those of most reported nano MO_x-based sensors. The sensor signal is stable over at least 2400 switching circles. Other performances, such as selectivity, relative humidity dependence and ambient pressure dependence were also studied. Possible physical mechanisms involved in the detection processes are discussed.

In the third part of the study, we prepared Pd coated sputtered WO_3 (Pd/sputtered WO_3) films to examine whether the oxide films produced by sputtering technique can be made to have satisfactory H_2 sensing performance comparable to that of other nano-structured highly porous H_2 sensor materials. The substrate temperature and sputtering pressure were varied when preparing the oxide films. The

structure and H_2 sensing performances of the Pd/sputtered WO_3 film samples were investigated as functions of these two parameters. Efforts are made on correlating the film structure and the H_2 sensing properties. Results were compared with those of Pd/SCBD WO_3 films to examine the feasibility of making high-quality H_2 sensors with sputtering technique.

List of Publications

1. **Meng ZHAO**, Jianxing HUANG, Monhan WONG, Yuming TANG, and Chungwo ONG, Versatile computer-controlled system for characterization of gas sensing materials, *Review of Scientific Instruments*, 82 (2011) 105001.
2. **Meng ZHAO**, Jianxing HUANG and Chungwo ONG, Room-temperature resistive H_2 sensing response of Pd/WO_3 nanocluster-based highly porous film, *Nanotechnology*, 23 (2012) 315503.
3. **Meng ZHAO**, Jianxing HUANG and Chungwo ONG, Improved H_2-sensing performance of nanocluster-based highly porous tungsten oxide films operating at moderate temperature, *Sensors and Actuators B: Chemical*, 174 (2012) 65-73.
4. **Meng ZHAO**, Jianxing HUANG and Chungwo ONG, Preparation and structure dependence of H_2 sensing properties of catalyst-coated metal oxide films submitted to *Sensors and Actuators B: Chemical*, under minor revision, 2012.
5. **Meng ZHAO**, Jianxing HUANG, Chungwo ONG, Microstructure Dependence of Hydrogen Sensing Properties of Palladium Functionalized Tungsten Oxide Films. Materials Research Society Symposium Proceedings, volume 1406, 2011 MRS fall meeting, 2011, Boston, USA.

6. Chungwo ONG, **Meng ZHAO**, Gas sensor with a highly porous structure constructed of catalyst-capped metal-oxide nanoclusters. US Patent, Application No. 13365277.
7. Chungwo ONG, **Meng ZHAO**, H_2 sensor based on a Pd-based coating of controllable connectivity made on a template of tailorable compliance. CN Patent, Application No. 201210161122X.

Acknowledgements

I am and will forever be indebted to Dr. C. W. Ong, my supervisor, not only for his invaluable guidance throughout my Ph.D. study, but also for his kind help in my life. Without his profound knowledge and academic insight, my research would not go on smoothly.

I would like to thank Dr. Jianxing Huang, Dr. Yuming Tang and Miss Yanli Xu for their technical supports over sample fabrication, measurements and their encouragements throughout the course of my study. I also like to express my appreciation to the Mr. Matthew M. H. Wong for his participation in building up the gas sensor measurement system, particularly in the part of automation.

I would like to thank Mr. M. N. Yeung of Materials Research Centre and all staff involved for their technical support.

I would also like to express my sincere gratitude to my friends and colleagues in our department for their help and discussion for my research work. They include, Dr. Steve Huang, Dr. Zhenhua Sun, Mr. Vincent Chan, Dr. Peng Lin, Dr. Wen Huang, Dr. Wei Lu, Dr. Jinhua Li, Dr. Gloria Xin and Dr. Wenchao Liu.

As last, I would like to dedicate this thesis to the family members, my soon-to-born baby, wife, parents and sister. I love all of you forever with all of my heart.

Table of Contents

List of Figures

List of Tables

Chapter 1 Introduction

1.1 Demands of H_2 sensing technology

Hydrogen (H_2) is highly explosive and has a lower explosion limit of 4% in air. The danger of H_2 arises from its large diffusivity of 0.61 cm^2s^{-1} (4 times to that of methane) and low ignition energy of 0.02 mJ in air (1/14 to that of methane) [1]. Reliable early warning of H_2 leakage is important to prevent explosion and ensure the safety of lives [2-7]. The following is a list of applications of H_2 or places using H_2 where H_2 sensors are needed for safety monitoring.

(i) H_2 plants over the world giving around 50 million tons throughput annually.

(ii) Workplaces in which H_2 is stored and used, including H_2 refilling stations, factories of H_2-powered machineries, laboratories engaged in green energy research, fossil fuel refinement factories and food processing factories etc.

(iii) Oxygen-hydrogen welding and plasma cutting industries, heat treatments etc.

(iv) Semiconductor industries and research labs involving thermal and plasma-assisted chemical vapour deposition processes.

(v) Household environment for monitoring the H_2 component in coal gas instead of another component, carbon monoxide, for detecting the leakage of the admixture. Note that more than 10 million households in Mainland China are

using coal gas. For this application, the potential market size of H_2 sensors could be over USD 1 billion.

(vi) The sale of H_2 fuel cell (HFC) is predicted to rise sharply from the year of 2015 associated with development of the market of H_2-driven vehicles [8, 9], where H_2 sensors are needed to monitor the level of H_2 concentration in the carriages. For H_2-driven vehicles solely, the potential market size is estimated to be 4 billion.

(vii) Spacecrafts using liquid H_2 for power generation.

(viii)Motors in power plants using H_2 as a coolant.

1.2 Projected requirements of performance of H_2 sensors in future applications

Along with the development of gas sensing technology, more parameters are recognized to be required for indicating the performance of a gas sensor. They are summarized in the following. The projected benchmarks of these parameters give guidelines of research work for seeking improvement. Different groups of parameters are emphasized according to specific applications.

(a) ***Lower detection limit (LDL)*** is the lowest detectable gas concentration. It is preferred to be as small as possible, especially in the application of detecting leakage of a hazardous gas. An LDL of 0.4% is suggested by the US

Department of Energy (DoE) for general H_2 safety monitoring [2]. A lower LDL < 0.1% is required by the manufacturers of automobiles [6].

(b) ***Upper detection limit (UDL)*** is the highest detected gas concentration before the sensing response gets saturated. Achievement of a higher UDL in general can broaden the dynamic range of the sensor. A H_2 sensor for safety monitoring is generally required to have a UDL of 4% [2, 6].

(c) ***Sensor response (S)*** of a gas sensor can be defined in different ways depending on their operation principles and uses. It is generally expressed in terms of the change of a physical property of the sensor material, e.g. resistance or optical transmittance, which value is varied with change of the concentration of the target gas. For a H_2 sensor, S can be defined as $(R_o - R_{H_2})/R_{H_2}$, where R_o is the base resistance in the H_2-free environment, and R_{H_2} is the resistance stabilized in an environment containing H_2 of a specific concentration.

(d) ***Normalized sensor response (NS)*** can be defined as S divided by the concentration of the detected gas. NS is more convenient than S in comparing the gas sensing performances of different sensors, because it is a normalized quantity reflecting representing the material's property. It is preferred to be as large as possible.

(e) ***Response time ($t_{respond}$)*** is defined in this thesis as the time required for sensor signal (e.g. resistance) to go through 90% of the total change $(R_o - R_{H_2})$. The

US DoE suggests that a H_2 sensor for safety monitoring should have a response time of 1 s at 4% H_2 or 60 s at 1% H_2 [2]. The benchmark proposed by automobile manufacturers is 1 s for the normal working condition of their products [6].

(f) ***Recovery time ($t_{recover}$)*** is the time required for the sensor signal (e.g. resistance) to increase by 90% of the total change ($R_o - R_{H_2}$). The US DoE suggests that a H_2 sensor for safety monitoring needs to have a $t_{recover}$ of 60 s disregarding the H_2 concentration [2]. On the other hand, the automobile manufacturers ask specifically for a $t_{recover}$ as short as 3 s for the normal working condition of their products [6].

(g) ***Stability*** can be defined in two different ways. (i) In static mode of operation, it is the duration in which the output of a sensor at a specific target gas concentration remains stable [10-12]. (ii) In cyclic mode of operation where the sensor is alternatively exposed to the detected gas and background atmosphere repeatedly, durability is defined as the number of cycles showing a stable range of response. We note that there is still no a common standard for assessing the durability of a gas sensor for both of these operation modes, such that data reported by different labs are not easily compared. Measurements in this aspect are time consuming. For these reasons, data of the cyclic stability of gas sensors are relatively less reported. In some papers involving investigations on gas

sensor's stability, the numbers of switching cycles carried out in the tests are too little, such that possible drift of signal with time is not really revealed [13-17]. In future research work, more efforts should be made to set up a certain common standard of measurement for specifying the stability of a gas sensor. On this basis, studies should be performed to search for new gas sensing materials of improved static and cyclic durability [12].

(h) ***Selectivity*** reflects the ability of a gas sensor to resist interference from interferants, which may be combustion gases, reducing gases and volatile organic compound vapours etc.

(i) ***Atmospheric pressure dependence*** of the output of a sensor should be as weak as possible for the sensor to be used over a range of elevation associated with a change of atmospheric pressure. One important example is a H_2 sensor used in a H_2-driven vehicle designed to travel over a range of altitude up to 9000 m from sea level. The corresponding range of the change of atmospheric pressure is 30.7 and 101 kPa [6].

(j) ***Working temperature*** has two definitions in this thesis. (i) It can be defined as the temperature of the sensing element $T_{operate}$ during operation. Some sensors are required to work at an elevated $T_{operate}$ with the use of a heater. They also are designed to have flame arrester and controlling circuits, and hence are more costly and bulky. The output may show thermal drift due to annealing effect or

fluctuation of $T_{operate}$. (ii) Working temperature can also be defined as the environment temperature, $T_{environ}$, which may vary from a few negative tens of deg.C (coldest places on earth) to over 100^{o}C (beside to an engine) [6]. Efforts should be made not only to produce new sensors of lower $T_{operate}$ close to the ambient temperature to avoid the said drawbacks; but should also be made to reduce the $T_{environ}$ dependence of the output.

(k) ***Relative humidity (RH) dependence*** of a gas sensor should be as weak as possible to avoid the influence of moisture on the output of the sensor and degradation of its performance.

(l) ***Batch-to-batch reproducibility*** indicates how good the performance of the sensors produced in different runs with the same processes/settings can be reproduced. Efforts should be made to try out new fabrication methods of good batch-to-batch reproducibility to help promote the yield and lower the cost of production.

(m) ***Miniaturizability*** of sensors is essential for the products to be producible with highly integrated processes so as to reduce the cost of production. A small gas sensor can also be operated with a lower power consumption, and is more likely to be used in a battery-powered portable appliance.

(n) ***Power consumption*** of a sensor is preferred to be as low as possible to diminish the drawbacks and cost due to the needs of a heater and related power controlling components.

(o) ***Price*** of a gas sensor is required to be as low as possible.

1.3 Commercialized H_2 sensors—performance and deficiencies

The performance indexes of major commercialized H_2 sensor products are reviewed and commented in the following.

A ***Pd-based resistivity-type H_2 sensor*** [2, 17-29] relies on the change of electrical resistivity of the material to detect H_2. The study of H-Pd system has a long history. In 1866, Graham reported that hydrogen can readily permeate into Pd [30]. A piece of Pd can absorb and retain hydrogen over 800 times of its own volume. This process starts with catalytic dissociation of H_2 molecules. H atoms are produced, which further diffuse into the lattice of Pd. When the H-to-Pd ratio in the solid solution is below 2.5%, the solid is in an α-phase [31]. It has a face center cubic (FCC) structure with a lattice constant lying in the range of 0.388–0.39 nm. The H atoms are located at interstitial sites without altering the FCC structure [32]. If more H atoms are incorporated, a β-phase starts to be formed, which coexists with the α-phase to form a two-phase mixture. The β-phase also has a FCC structure, in which

the incorporated H atoms are still at interstitial sites. However, the lattice constant is increased by 3% compared with that of the α-phase and has a magnitude of 0.401 nm — it can be slightly increased by further incorporation of H atoms. A substantial volume expansion is resulted, and the phenomenon is named as hydrogen induced lattice expansion (HILE) or volume breathing effect. Until the H content is increased to 40%, the α-phase disappears entirely, but only the β-phase is left.

The resistance of the substance is also changed with the H content. In the α-phase with H content below 2.5%, ρ increases with increasing H content, and finally reaches a level of 1.05 times of that of the metal phase [33, 34]. When the H content is further increased to 40% such that the structure is entirely transformed to the β-phase, ρ is around 1.8 times of that of the metal phase. This mechanism is referred to as the α-to-β (Pd-to-PdH) phase transition effect.

A Pd-based resistivity-type H_2 sensor is insensitive to interferants, atmospheric pressure and relative humidity RH. It can work at relatively low $T_{operate}$. The batch-to-batch reproducible is fairly satisfactory. Furthermore, it can be in thin film form to realize miniaturization and mass production. However, it has a low normalized sensor response NS ~ 7.6×10^{-7}/ppm (measured at 2% H_2) [35]; a long response time ~ 60 s; strong $T_{environ}$ dependence; high power consumption and high production cost.

A ***metal-oxide- (MO_x-) type H_2 sensor*** [3-6, 36-53] adsorbs oxygen molecules O_2 on its surface. The surface-sorbed oxygen molecules trap free electrons from the

oxide grains to form negative ions, e.g. O_2^-, O^- and O^{2-}. A depletion layer is thus formed at the surface of the oxide. The sensor shows a high resistance at this stage. When H_2 molecules appear to react with the oxygen ions and remove part of them, such that free electrons are released and return to the oxide. The depletion region becomes thinner. The resistance of the material drops as a consequence with a magnitude depending on the surrounding H_2 concentration.

A sensor of this type has a high normalized sensor response NS ~ 0.15/ppm (measured at 2% H_2) [51], and a considerably short response time of 5–10 s. However, the output is readily interfered by the presence of other reducing gases, and is also dependent prominently on atmospheric pressure $T_{environ}$ and RH [36-53]. Furthermore, it needs to work at an elevated $T_{operate}$, which may lead to thermal instability of the output. The sensor is relatively bulky; not easily miniaturized, high power consuming (~ 500 mW) and costly [3-7]. Thick film process is usually employed to fabricate the devices, but batch-to-batch reproducibility is generally not satisfactory.

An ***electrochemical- (EC-) type H_2 sensor*** contains a working electrode and a counter electrode immersed in an electrolyte [5-7, 54-56]. H atoms are produced by dissociating H_2 molecules from the environment at the electrodes, and then enter the electrolyte to generate an amperometric [54-56] or a potentiometric signal [55].

The output is insensitive to the variations of atmospheric pressure, $T_{environ}$ or

RH. An EC-type H_2 sensor can work at a $T_{operate}$ close to the ambient temperature, and does not need a heater and controlling circuit. However, it has a low normalized sensor response NS ~ 0.002/ppm (at 1.15% H_2) [55], and is readily interfered by other reducing gases. Batch-to-batch reproducibility is not satisfactory. Miniaturization is not easily realized, and the production cost is relatively high.

A ***catalytic combustion- (CC-) type H_2 sensor*** [5-7, 57-59] is made of a surface catalyzed material, which is heated up to an elevated $T_{operate}$. Some H_2 molecules in the surrounding are oxidized on the surface, causing the sensor's temperature to rise. The change of temperature is sensed by a platinum (Pt) thermometer adhered to the sensor.

A CC-type sensor is insensitive to atmospheric pressure, $T_{environ}$ and relative humidity RH. The production process is satisfactorily reproducible. However, its normalized sensor response NS is low, i.e. $< 5.3\times10^{-4}$/ppm (at 1% H_2) [57] and $T_{operate}$ is high, i.e. a few hundreds of deg.C. Its output is easily affected by the presence of other combustion gases. It is difficult to be miniaturized. Power consumption is high, i.e. > 500 mW. The production cost is high.

A ***thermal conductivity- (TC-) type H_2 sensor*** [5-7, 60] monitors the thermal conductivity of a gas sample. Since the thermal conductivity of H_2 is the largest among all gases, inclusion of H_2 in the sample gas can cause a substantial difference of the thermal conduction from the expected value of the background. The measured

result can be used to determine H_2 concentration in the environment.

A sensor of this type has the same advantages as those of a Pd-based resistivity-type H_2 sensor. However, it has a low normalized sensor response ~ 2.5×10^{-6}/ppm (at 10% He) [60] with a strong $T_{environ}$ dependence. The response time is in the range of 30–60 s, which is too long for the device to be applied in a H_2-driven vehicle. The life time of it is almost the shortest compared to other H_2 sensor types. Miniaturization of this type of sensors is difficult. Power consumption is relatively high (> 500 mW). Production cost is also high.

This review indicates that commercialized H_2 sensor products do not meet all the projected benchmarks of H_2 sensors for future use [2, 6]. The deficiencies are summarized in the following:

(a) ***Response time***. Commercialized MO_x type H_2 sensor has the shortest response time of 5 s, while those of others are usually about tens of seconds. They are much longer than the target value of 1 s proposed by automobile manufacturers.

(b) ***Selectivity***. The commercialized MO_x type, EC type and CC type H_2 sensors have poor selectivity, which greatly hinders their applicability in practice.

(c) ***Sensor response***. The normalized sensor responses NS of commercialized EC type, CC type, TC type and Pd-based resistive-type H_2 sensors are much smaller than that of the commercialized MO_x type H_2 sensors. Further efforts are needed to improve the sensor response in order to get lower LDL.

(d) ***Anti-inference ability***. H_2 sensors for future use are required to be insensitive to the change of ambient conditions, including the change of ambient pressure from 60 to 120 KPa and relative humidity RH. However, most commercialized H_2 sensors are found not working properly below 70 KPa, but strongly affected by moisture [3, 4].

(e) ***Miniaturizability, low power consumption and price***. Miniaturizability of sensors is important in lowering the production cost; increasing the throughput and reducing power consumption. For this reason, production process to be employed is preferred to be compatible with silicon-based micro-machining techniques. Miniaturization of MO_x-based sensor and Pd-based H_2 sensor is possible, but the former usually needs a flame arrestor which limits the overall size of the device; and the latter has other drawbacks like long response time and low sensor response etc.

1.4 Research frontier of Pd-based HILE-type H_2 sensors

1.4.1 Working principle and guideline of design

When the H content in palladium hydride Pd-H increases, the resistivity rises, and at the same time the volume also expands (HILE effect). The former mechanism has been used to produce commercialized H_2 sensors, the latter mechanism is applied

in research to develop Pd-based HILE-type H_2 sensors.

In the research of Pd-based HILE-type H_2 sensors, Pd-based materials containing were made to have nano discontinuity of 0–500 nm (referred to as isolation gaps afterwards). They could be in the forms of nanowires with electrically isolated gaps [61-70]; film of dispersive Pd clusters or porous film constructed of loosely connected Pd nanoparticles [71-85]; or Pd film of isolation gaps deposited on a patterned substrate [86-90] etc. When these materials are put into contact with H_2, HILE effect occurs to alter the electrical connectivity of the structures, such that percolation-like resistance drop could occur when the isolation gaps are closed. Reversed response occurs during dehydrogenation. This mechanism is designated as "HILE-mechanism" to differentiate it from the former one designated as "resistivity-mechanism" in this thesis.

Note that the HILE-mechanism is also accompanied by resistivity-mechanism. They give opposite resistive responses to determine the final resistance of the Pd-based material. The contribution of the HILE-mechanism can greatly exceed that of the resistivity-mechanism if the size of the isolation gaps is large enough. It is also observed that the resistive response of an HILE-type sensor with certain degree of initial connectivity is dominated by the resistivity-mechanism at low H_2 concentration, and is then dominated by the HILE-mechanism when the H_2 concentration is increased to exceed a threshold value [72, 73, 75, 76, 79, 80, 88, 90-

92]. This critical point of operation is referred to the onset of the HILE mode.

The requirements of the sensor's performance for a specific application and miniaturizability of the device should be taken into consideration when designing an HILE-type H_2 sensor, which lead to the following guidelines.

(i) The size and distribution of the isolation gaps in the Pd-based material should be specified according to the target lower detection limit LDL; upper detection limit UDL and normalized sensor response NS.

(ii) The substrate surface pattern could be designed to exhibit certain degree of compliance to absorb part of the strains caused by the HILE process in order to achieve short response time and improve the stability of the sensor response.

(iii) The fabrication process is preferred to be highly integrated to fulfill the needs of large throughput realized with a low-cost production process; satisfactory batch-to-batch reproducibility; and miniaturization of the products for the convenience of use. Employment of Si based micro-fabrication technology is most preferred.

1.4.2 Categories of HILE-type H_2 sensors

Ever since the pioneer work of Favier in 2001 [62], HILE-type sensors of various designed have been investigated. They are basically classified into five groups as summarized in the following according to their designs and H_2 sensing

performance.

Type-I: Stress induced fracture [61-70]**.** A sensor of this type is composed of Pd nanowires deposited on a film. Cracks of sizes in the order of tens to hundreds nm are created successively in the nanowires due to the stresses generated at the interface between the Pd nanowires and the substrate during hydridation and dehydridation processes. With this dimension of isolation gaps, resistive switching usually occurs when at H_2 concentration is high enough to initiate the α-to-β phase transition. The LDL of H_2 concentration detectable with the sensors as reported in literature is about 2% at 300K. Further increase in H_2 concentration causes little change in the resistance, where the UDL value is limited to around 5%.

The disadvantage of this sensor type is the poor control of the size and number of the cracks according to the way that they are generated, such that the sensor response is not controllable. Even worse, the crack size and number change continuously during use, and hence the sensing properties are unstable. Furthermore, batch-to-batch reproducibility in production is not satisfactory. Si-based micro-fabrication technology is difficult to be applied for production.

Type-II: Discontinuous or highly porous films on nanowires [71-85]**.** A sensor of this type is made of a discontinuous [71-78]; or a highly porous Pd film [79-83]; or loosely assembled nanowires [84, 85]. The Pd film in fact contains numerous partially closed isolation gaps. The connectivity is thereby highly sensitive

to the volume change due to the HILE effect. As a consequence, the LDL of the sensor can be as low as several ppm. However, the NS of the sensor is typically 1000 times smaller than that of a type-I sensor.

The size of the isolation gaps in such a film sensor is difficult to control, and are difficult to be aligned. In addition, their size and number change continuously with increasing duration of use, leading to poor stability of the sensor response. Though the fabrication of the sensor can be accomplished with Si-based micro fabrication technology, the size and number density of the isolation gaps in the Pd film, and thus the sensing performance, are highly sensitive to the uniformity of film thickness. This imposes more stringent requirements on the control of the fabrication process.

Type-III: Coating on a patterned substrate. A sensor of this type is fabricated by depositing a Pd coating on a patterned substrate, such as a porous Si substrate; anodic aluminum oxide substrates; Si cantilevers or polymer coated electrodes [86-90]. Some of its performance indexes can be varied in broad ranges through adjusting the isolation gap width in the pattern. With larger isolation gaps [86, 87], it behaves like a type-I sensor for having high LDL, low UDL and large NS. The revise holds if the isolation gap width is narrow [88-90].

For some of type-III sensors made to have wider isolation gaps, both the width and distribution of the gaps can be controlled precisely [86, 87], and can be fabricated with Si-based micro-fabrication technology. However, due to the use of

rigid substrate, the value of $t_{respond}$ is too long (> 100s) and the durability is not guaranteed as well.

Type-IV: Mono-atomic layer capped Pd nanoparticle assembled film. A sensor of this type is fabricated by drop casting of mono-atomic layer capped Pd nanoparticles on a substrate [92-94]. Upon exposure to H_2, the Pd nanoparticles penetrate through the mono-atomic layer to get contact with the adjacent one so as to reduce the overall resistance of the material. With this configuration, the LDL is ≥ 0.1% and UDL reaches 10%. The NS is very low due to the small gap width similar to that of a type-II sensor. The $t_{respond}$ is in the range of 10–60 s. The gap width and distributions are completely uncontrollable due to the poor reproducibility associated with the drop casting method. It is also not compatible to the Si-based micro fabrication technology.

Type-V: Focus ion beam milling. A sensor of this type is made to have an isolation gap in Pd by using focus ion beam (FIB) milling [95]. The gaps width varies from 25 to 70 nm depending on the beam current. The typical LDL is 2% and NS is high due to the large gap width. The $t_{respond}$ of the sensor is as long as 100 s, because the Pd sensor element adheres firmly to the substrate. Though FIB milling can have good control on the configuration of the isolation gaps, it is not suitable to be used for mass production.

1.5 Research frontier of nano MO_x-based H_2 sensors

Nano metal oxide (MO_x) materials are widely used to develop new H_2 sensors in recent years based on two conceptions. The first one is that a nano MO_x has a large effective surface area to react with the target gas, and hence the sensor response is strong. Further, if the characteristic dimension (L) of the nano-sized species forming the material is close to two times of the thickness of the depletion layer of the MO_x material (usually ≈ several nanometers), the species are basically depleted in air, such that the resistance can drop from a very high R_o during hydrogenation to give a large sensor response S. Note that L is referred to the diameter of the nanoclusters, nanowires, nanorods or nanofibers; or the thickness of nnaobelts forming the nano MO_x. The second concept is that if the said nano-sized species are loosely connected to form a highly porous structure, the target gas molecules can diffuse agilely inside the structure to result in a fast response rate, or equivalently a short $t_{respond}$.

Our literature review shows that many gas sensors claimed to be made of "nano" materials or to have "nano" structures cannot realize the above two conditions concomitantly. Some of them are confirmed to have high porosity with fast response rate, but the sizes of the gas sensing species are not really in the nano scale, such that the values of S are not as spectacular as expected. Some examples are: Pt coated WO_3 film made of nanoclusters with L ≈ 35 to 65 nm showing a small

normalized sensor response NS of 8.9×10^{-7}/ppm [96]; Pt coated molecular beam expitaxy ZnO "nanorods" of L ≈ 50–150 nm showing a low NS of 2×10^{-4}/ppm [97]; metal organic chemical vapor deposited ZnO single-crystal nanorods of L of 30–150 nm showing a low NS of 1.6×10^{-4}/ppm [16]; chemical vapor deposited single-crystalline ZnO nanowire with L ≈ 100 nm showing a low NS of 5.2×10^{-3}/ppm [98]; thermally evaporated single-crystalline SnO_2 nano-belt with a thickness of 80 nm and width of 330 nm showing a low NS of 3.3×10^{-5}/ppm [99]; and a weave of TiO_2 nanofibers prepared by hot-pressed electro-spinning with L ~ 300 nm, showing a low NS of 2×10^{-3}/ppm [100].

Some other MO_x-based H_2 sensors are found to contain small enough genuine nano gas sensing species and show high S values, but the matrixes in which the nano species are embedded are too dense to give fast response rates. Some examples are: sol-gel film made of Pd-doped WO_3 nanoclusters with L ~ 20 nm embedded in a dense matrix showing a long $t_{respond}$ ~ 1300 s [101]; sol-gel Pt-coated thin film made of In_2O_3-doped SnO_2 nanoclusters with L of 6–7 nm embedded in a dense matrix, showing a long $t_{respond}$ of 10000 s [102]; sol-gel Pt-coated thin film made of In_2O_3-doped SnO_2 nanoclusters of L ~ 3 nm embedded in a dense matrix showing a long $t_{respond}$ of 500 s [103]; and sol-gel film made of indium-tin oxide ($InSnO_2$) nanoclusters embedded in a dense matrix showing a long $t_{respond}$ of 500–1000 s [65].

One further remark is that some sensors made of 1-D nano gas sensing species

(like nanowires) are quite often prepared by employing the "pick-and-drop" process, where the species are dispersed in a liquid and then transferred onto a substrate [42, 48], followed by a post-annealing process. This method is difficult to control the quantity and the uniformity and distribution of the species in the sensor structure. Hence, reproducibility in mass production is not ensured.

1.6 Scope of this study

Based on the frontier research of H_2 sensors summarized above, this project is organized to consist of three major parts.

Part 1: Pd thin film of controllable connectivity deposited on compliant Si pillar(s).

The methods for preparing HILE-type H_2 sensors employed so far cannot give effective and precise control of the connectivity of the Pd films, so that the sensor response, dynamic range of detection and response rate etc. are lack of control. We tried out a new method to alleviate this problem by depositing Pd films on a Si pillar or a 2-dimensional Si pillar array made on a Si wafer, with the isolation gap width surrounding the pillar(s) to be precisely produced with Si micromachining technique.

With this approach, the connectivity of the Pd film can be controlled in a precise manner, and hence the sensing properties can be tailored more flexibly. The Si pillar(s) has a large height-to-thickness ratio and hence is compliant to allow the stresses generated in the Pd film due to HILE to be released more readily.

The H_2 sensing properties were investigated as functions of the pattern of the underlying Si pillar (single or 2-D array, and the size of isolation spacing); the thickness of Pd layer, the presence of an Au/Cr buffer layer before addition of the top Pd layer, and operation temperature etc. The durability of the sensor prototypes is one of the focal points to study. The key results are compared with those of the commercialized H_2 sensor products and research results reported by other groups.

Part 2: palladium-coated nanocluster-assembled highly porous tungsten oxide films

In this part of study, we hope to realize the idea of producing MO_x thin film H_2 sensors constructed of genuine nano-sized clusters and having an extremely high porosity concomitantly, in order to achieve both high sensor response and response rate.

In practice, WO_3 films were prepared by using supersonic cluster beam deposition (SCBD), which was further coated with a sputtered palladium (Pd) thin film. The WO_3 film is constructed of loosely connected tungsten oxide (WO_3) nanoclusters, such that the structure is expected to have a very large porosity. The sensor response, recovery rates, cyclic stability, operation temperature dependence, ambient pressure dependence, relative humidity dependence, selectivity against various organic compound (VOC) vapours etc. of the sensor prototypes were measured. Possible physical mechanisms involved in the detection processes are discussed. The key results are compared with those of the commercialized H_2 sensor

products and research results reported by other groups.

Part 3: Pd-coated sputtered tungsten oxide films

This part of study is aimed at examining whether Pd-coated WO_3 films prepared by using sputtering technique can be made to have satisfactory sensor response, response and recovery times in H_2 sensing. Sputtering technique is concerned because it is a typical thin film fabrication technique widely used in industries. It is also flexible in tailoring the film structure and properties through adjusting substrate temperature and sputtering pressure for deposition.

All the above-mentioned sensing properties of the device prototypes were measured. Results are correlated with the structural parameters of the films, including crystallization, film thickness, surface roughness and Pd thickness etc. Data are compared with those of Pd/SCBD WO_3 films. Guidelines for producing high-quality Pd-coated WO_3 film for H_2 sensing are presented.

The thesis are organized to present an thorough review of the field and the rationales for using the approaches in Chapter 1; sample fabrication and characterization techniques in Chapter 2 and 3; results of the above mentioned Part 1 to 3 in Chapter 4 to 6; and an overall conclusions in Chapter 7.

Chapter 2 Experimental methods I—Fabrication of hydrogen sensors

We fabricated two major types of hydrogen sensors. A sensor of the first type is made of a palladium (Pd) film deposited on a silicon (Si) pillar or a 2-dimensional Si pillar array. The Si pillar(s) has a high aspect ratio and hence can be bent readily to release some stresses induced by volume expansion of Pd coating during hydridation. A sensor of the second type has a tungsten oxide film coated with a Pd catalytic layer (Pd/WO_3). Furthermore, the WO_3 layer of a second type sensor was fabricated by using supersonic cluster beam deposition (SCBD) or magnetron sputtering. Details of sample fabrication are described in this section.

2.1 Pd coating of controllable connectivity on compliant silicon pillar array

A sensor is made by depositing a Pd film of controllable connectivity on a compliant Si pillar array or a Si pillar array with the following steps (Figure 2.1).

Step 1: 1-μm thick silicon dioxide (SiO_2) was grown on both sides of a 4-inch n-type <100> Si wafer by wet thermal oxidation. They serve as the etching mask in an ensuing Si deep etching process. The oxidation process was performed in an ASM A400 oxidation furnace at 1100^{o}C for 200 min.

Step 2: Photo-lithography was performed to produce a pattern on a photoresist (PR) layer. PR AZ703 was dropped and spin coated onto the silicon wafer spinning at 4000 rpm for 30 s to give a 1-μm coating. After prebaked at 90^{o}C for 60 s, the wafer was transferred to an aligner (SUSS Microtec MA6-2, I line) and exposed to 31 mW/cm^{2} of UV light for 3 s. The wafer was then post-baked at 110^{o}C for 1 min. Standard development process followed.

Step 3: The PR pattern was transferred to the thermal SiO_2 layer by applying reactive ion etching with an STS multiplex Advanced Oxide Ether system. The settings of the process were listed in Table 2.1. By using this recipe, the etching rate of SiO_2 was about 0.2 μm min^{-1}, faster than that for Si by more than 100 times.

Step 4: The residual photo-resist of step 3 was stripped off by applying reaction ion etching in the PS210 microwave plasma system.

Table 2.1 Parameters used in the dry etching process of the SiO_2 layer.

Gas	Flow rate (sccm)	Coil power (W)	Platen Power (W)	Chamber pressure (mTorr)	Duration (s)	Etching rate (μm/min)
C_4F_8	10	935	130	4	390	0.2
He	174					
H_2	8					

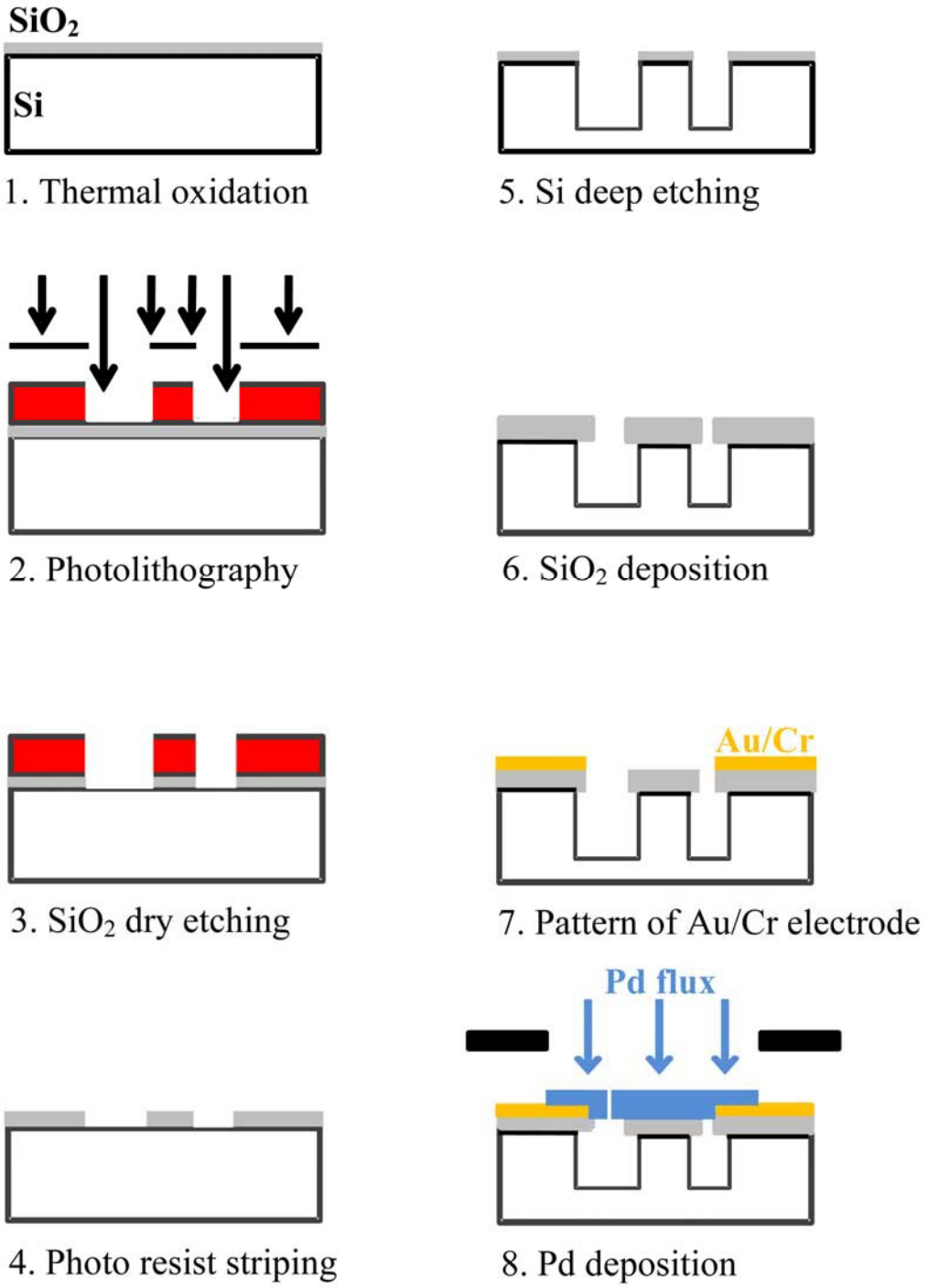

Figure 2.1 Flow chart of fabrication process of Pd coating of controllable connectivity on a compliant silicon pillar

Step 5: Template of high-aspect ratio (HAR) silicon micro-pillars was fabricated with an STS multiplex Advanced Silicon Etcher. The Bosch process [104-109], named after the company (Robert Bosch GmbH), was employed. A complete run was composed of repeated passivating-etching cycles. In the passivating step, Figure 2.2 (a), C_4F_8 gas was admitted into the chamber and decomposed in the plasma to result in a teflon-like polymer layer on both the bottom and the sidewall of the etched trench. In the etching step, Figure 2.2 (b), SF_6-O_2 mixture was introduced into the chamber and ionized in the plasma. Meanwhile, a negative voltage was applied to the sample plate. Positively charged ions, e.g. SF_6^+ et al., were accelerated to bombard the polymer layer. As a result, the teflon-like polymer layer at the bottom of the trench was removed to expose the underlying Si, which was further etched isotropically by the active species in the plasma (fluorine radical et. al.). Rapid switching between passivating and etching cycles realizes HAR etching of bulk silicon. The parameters used in our study were listed Table 2.2. It should be noted that, to minimize the undercut of the silicon micro-pillars, a C_4F_8 gas flow was added into the etching gas in the first 3 min of the process, with the flow rate ramped from 15 to 0 sccm in a step-wise manner. The durations of the passivating cycles and etching cycles were set at 6 and 8 s respectively, giving an average etching rate of about 2.5 μm per min.

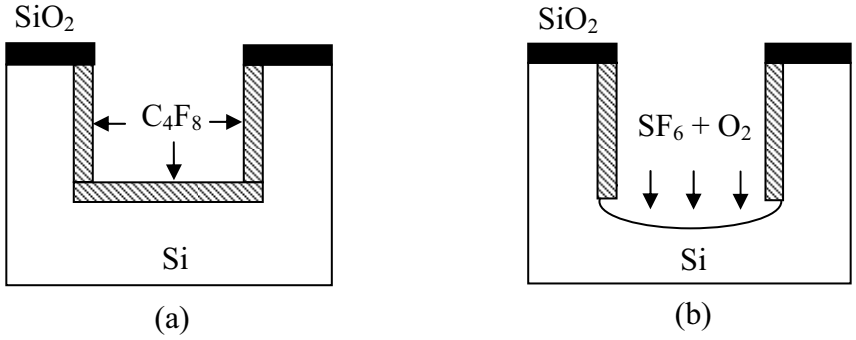

Figure 2.2 (a) and (b) passivating-etching cycle of a standard Bosch process.

Table 2.2 Parameters used in the deep etching of Si.

Cycle	Gas	Flow rate (sccm)	Coil power (W)	Platen Power (W)	Chamber pressure (mTorr)	Duration (s)	Etching rate (μm/min)
Passivating	C_4F_8	100	600	0	18	6	2.5
	SF_6	0					
	O_2	0					
Etching	C_4F_8	15/0	800	11	33	8	
	SF_6	130					
	O_2	14					

Step 6: A SiO_2 buffer layer was then sputtered onto the top of the Si micro-pillar template to narrow down the width of the inter-pillar separations. The SiO_2 buffer layer was deposited in a homemade three-head magnetron sputtering system

as shown in Figure 2.3. The system has a stainless steel chamber connected to a turbo molecular pump backed with a rotary pump. It is equipped with a Baratron type capacitance pressure sensor. A sputtering guns was radio frequency (RF) powered and used to sputter the SiO_2 coating. The chamber was first pumped down to a base pressure of 10^{-6} Torr. Argon (Ar, 99.995%) and oxygen (O_2, 99.995%) gases with flow rates in a ratio of 7.5 to 10 sccm were admitted into the chamber by using two mass flow controllers (MKS model: 1179A). The conductance of the high vacuum valve was adjusted to stabilize the pressure at 3 mTorr. The sputter gun was then turned on at a power level of 250 W for 5 min to pre-clean the surface of the Si target. The shutter in front of the target was then opened to start depositing SiO_2 until the expected film thickness was reached. The substrate holder was rotated with a motor throughout the deposition process to ensure the uniformity of the film thickness. The substrate temperature (T_s) can be adjusted by means of a resistive heater regulated with a proportional-integration-differentiation (PID) temperature controller. The preparation conditions were listed in Table 2.3.

Step 7: Au/Cr electrodes were added for electrical measurements. An Au/Cr bi-layer was first sputtered onto the sample by using two DC powered sputtering guns of the sputtering system with the conditions listed in Table 2.3. The thicknesses of the Cr and Au films were made to be 10 and 100 nm respectively. Photoresist (PR) AZ5204 was spin-coated onto the film at a spin rate of 3000 rpm for 30 s to result in

a thickness of ≈ 1μm. The sample was prebaked at 115°C for 1 min. The pattern of the electrodes was transferred to the PR layer with a UV aligner, and the pattern was developed without post-baking the PR layer. The unprotected part of the Au/Cr bi-layer was selective etched by using commercialized Au and Cr etchants. Finally, the residual PR was completely removed by using a PS210 Microwave plasma system.

Step 8: A top Pd layer was sputtered onto specified locations on the Si wafer by using a stainless steel shadow mask with the preparation conditions listed in Table 2.3. To avoid contamination of Pd due to the PR or its by-products, the standard micro-fabrication process was not adopted in patterning the Pd layer. The thickness of the Pd layer is set to partly or completely close the isolation gaps between the Si pillar(s) to make the sample to show the target gas sensing properties.

Table 2.3 Preparation parameters used for depositing the SiO_2, Cr, Au, and Pd films.

Materials	Source type	Power (W)	Gas	Flow rate (sccm)	Pressure (mTorr)	T_s (^oC)	Sample holder	Deposition rate (nm/min)
SiO_2	RF	250	O_2 Ar	10 7.5	3	100	Rotating	400
Cr	DC	140	Ar	10	10	100	Rotating	2.5
Au	DC	100	Ar	10	10	100	Rotating	15
Pd	DC	100	Ar	10	6	100	Static	20

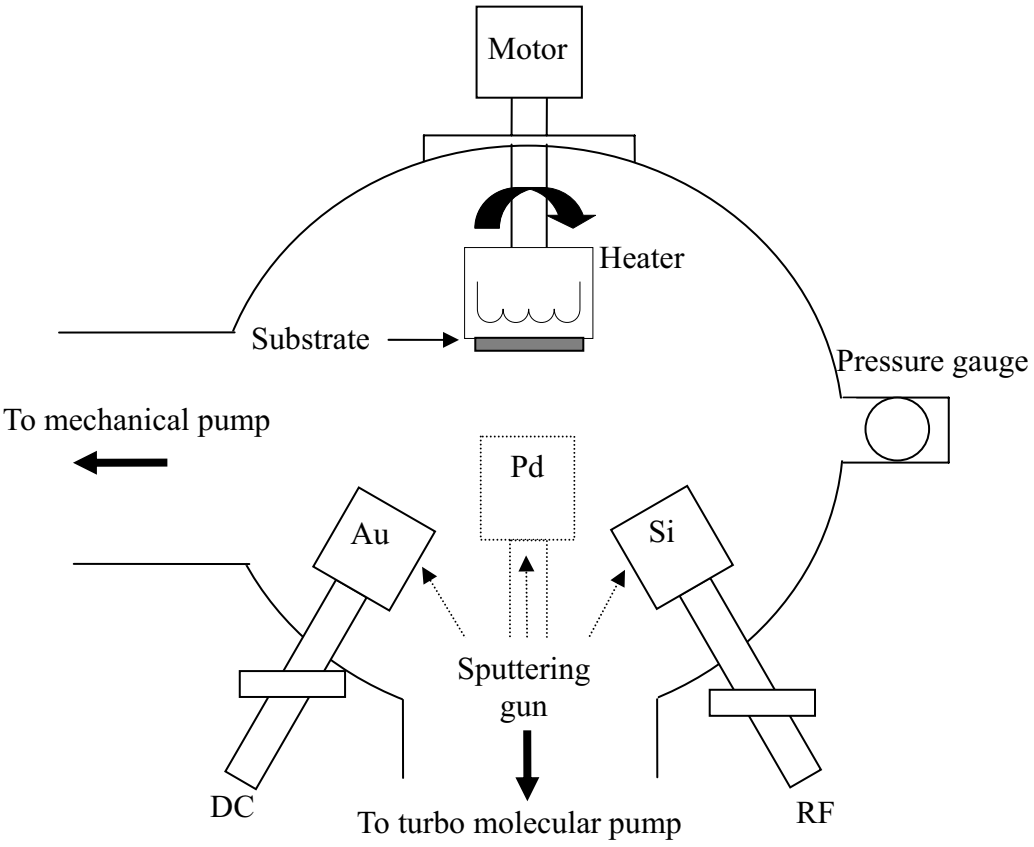

Figure 2.3 Schematic diagram of the magnetron sputtering system used for thin film deposition.

2.2 Pd/SCBD WO_3 film hydrogen sensors

2.2.1 Fabrication of Pd/SCBD WO_3 films

A supersonic cluster beam deposition (SCBD) system (Tethis, Italy) was used to fabricate WO_3 films [110-117]. In this system, a tungsten metal rod (1/4 inch in diameter and 99.95% purity) was mounted inside a chamber of a Pulsed Micro-plasma Cluster Source (Figure 2.4). The metal rod was rotated with a motor. Pulses of Ar gas were admitted into it at a frequency of 5 Hz. Meanwhile, electric pulses of -900 V were applied to the target at the same frequency with a delay of 220 μs relative to the gas pulses. Micro-plasma pulses were thus generated to erode the metal target by removing tungsten atoms from it. The atoms were condensed into nanoclusters and carried by the gas flow to enter an Expansion Chamber. In this chamber, supersonic expansion of the gas flow occurred. After passing through a set of aerodynamic lens, only the nanoclusters of diameters falling in a specific range were selected. They formed a beam of nanoclusters, and finally entered a Deposition Chamber and were deposited on a substrate (Corning 7059 glass slide or SiO_2 coated Si wafers with pre-patterned inter-digital electrode). These nanoclusters were of low kinetic energies. Consequently, they were not deformed in the deposition process. They were also rather immobile to relocate over the substrate surface, such that they were loosely packed together to form a film of a high porosity. A post-annealing

process is performed with a quartz tube furnace to stabilize the film structure. Meanwhile, high purity oxygen 99.99% was introduced into the quartz tube at a flow rate of 2 sccm. The annealing temperature and duration were 250^{o}C and 12 hrs, respectively. Then a thin Pd layer with a nominal thickness about 5 nm was sputtered onto the SCBD WO_3 films. The sputtering parameters for the Pd catalyst layer were listed in Table 2.4.

Corning 7059 glass slide or SiO_2-coated Si wafer were used as the substrates. For some samples, a pair of inter-digital electrodes (IDE) were made on a substrate surface first. A film sensor is produced by depositing an SCBD WO_3 film on a substrate. For those without using IDEs, two silver paste electrodes, each with a width of 4 mm, separated by 5 mm, were made on the top of the Pd film. The device was surface mounted onto a printed circuit board, with the contact pads wire bonded to the external circuit by using a wire bonder (ASM AB-502).

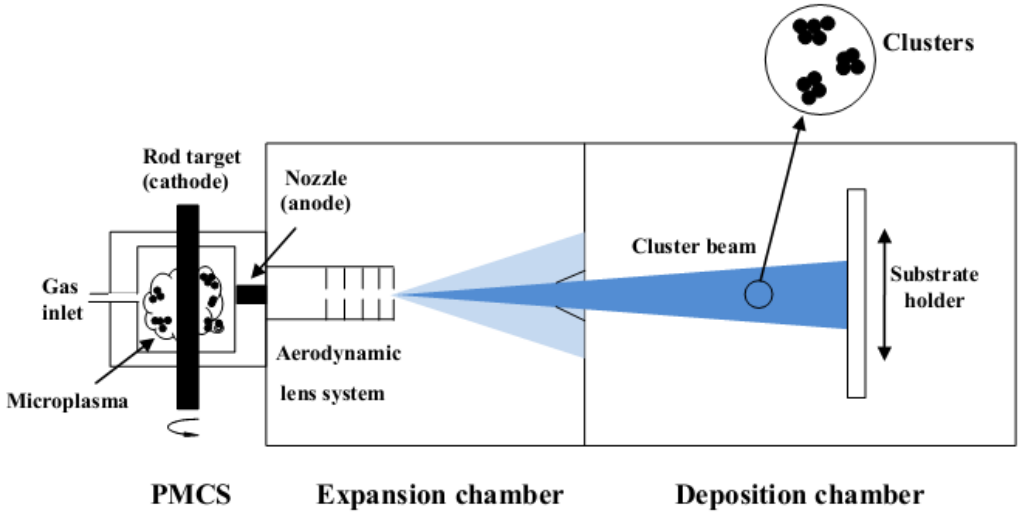

Figure 2.4 Schematic diagram of SCBD system.

Table 2.4 Preparation parameters of Pd, Au and Ti films.

Material	Source type	Power (W)	Gas	Flow rate (sccm)	Pressure (mTorr)	T_s (^oC)	Sample holder	Deposition rate (nm/min)
Pd	DC	50	Ar	10	10	20	Rotating	5
Ti	DC	100	Ar	10	10	20	Rotating	1.7
Au	DC	100	Ar	10	10	20	Rotating	15

2.2.2 Fabrication of inter-digital electrodes (IDE)

IDEs were used for some samples in order to reduce the base resistance of oxide films. The fabrication process of the IDEs is described in the following.

Step 1: A 1-μm thick photoresist (PR) AZ5204 layer was first spin-coated onto a Si wafer coated with a 500-nm SiO_2 layer with a spin rate of 3000 rpm for 30 s. It was then prebaked at 115^{o}C for 1 min. UV exposure was applied to transfer the IDE pattern to the PR layer. The sample was then post-baked at 110^{o}C for 1 min, followed by a development process. Finally, the residual PR was completely removed in a PS210 Microwave Plasma System (PVA Tepla America Inc).

Step 2: An Au/Ti bi-layer was sputtered onto the patterned substrate by using the parameters listed in Table 2.4. The thicknesses of the Au and Ti layers were 100 and 25 nm respectively. The wafer was then soaked in acetone (purity 99.5%). The metal covering PR without being exposed to UV was flushed away, and the IDE

pattern was left. The wafer was further cleaned and diced with a dicing system (DISCO DAD 321).

Figure 2.5 (a) is an SEM image of the IDE on a SiO_2/Si substrate, which have an overall dimension of 1.8×1.8 mm^2. It contains 70 pairs of electrodes. The spacing and width of the fingers are 5 and 10 μm respectively, Figures 2.5 (b–c). Figure 2.6 is a photo of a diced Pd/SCBD WO_3 film with IDEs. The overall dimension is ≈ 2.2 × 2.2 mm^2. Such a device is ready for wire bonding to the external circuit and subsequent gas sensing measurements.

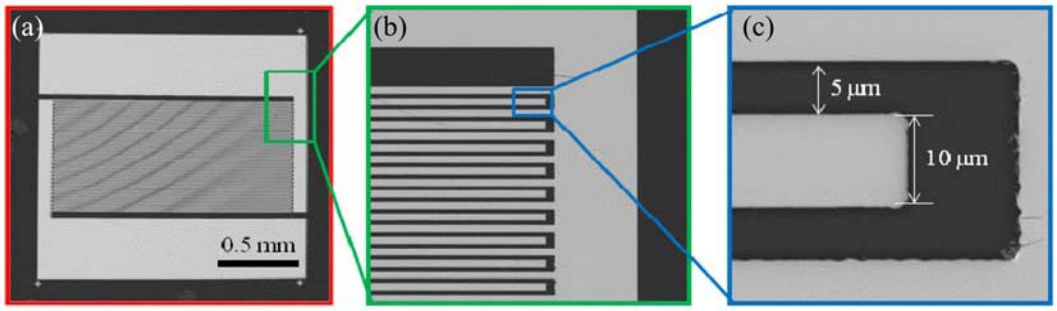

Figure 2.5 SEM images of IDE fabricated on SiO_2/Si substrates.

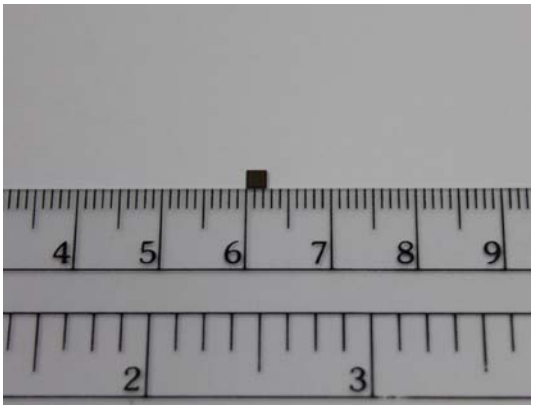

Figure 2.6 A photo of a Pd/SCBD WO_3 film having IDE on a SiO_2/Si substrates.

2.3 Pd/sputtered WO_3 film hydrogen sensors

Pd/sputtered WO_3 films were fabricated by using a magnetron sputtering system depicted in Figure 2.3. Tungsten (W, purity 99.95%) and Pd metal discs (purity 99.95%) of 2" in diameter were used as the targets. The substrates were Corning 7059 glass slides. The working gas was 20% argon-80% oxygen mixture. The sputtering pressure P_s and substrate temperature T_s were varied in the ranges of 3–60 mTorr and 50–550^{o}C. Each sputtering process lasted for 20 min. In each run, a WO_3 film was deposited first, and the chamber was then pumped down to 10^{-6} Torr. Pure Ar gas was then admitted into the chamber to sputter a Pd film. P_s was switched to 10 mTorr, but the setting of T_s was unchanged. The deposition time was 15 s to give a nominal thickness of ≈ 1.15 nm. The deposition conditions of the samples were tabulated in Table 2.5. At last, two 4 mm-wide silver paste electrodes 5 mm apart were made on the film surface.

Table 2.5 Fabrication conditions of the Pd/sputtered WO_3 films.

Sample code	WO_3				Pd			
	Gas	Flow rate (sccm)	T_s (^oC)	P_s (mTorr)	Gas	Flow rate (sccm)	T_s (^oC)	P_s (mTorr)
WO50-3	Ar	5	50	3	Ar	10	50	10
WO50-10	O_2	20	50	10			50	
WO50-30			50	30			50	
WO50-60			50	60			50	
WO350-3			350	3			350	
WO350-10			350	10			350	
WO350-30			350	30			350	
WO350-60			350	60			350	
WO550-3			550	3			550	
WO550-10			550	10			550	
WO550-30			550	30			550	
WO550-60			550	60			550	

Chapter 3 Experimental methods II—Characterization and gas sensing property measurements

3.1 Thickness measurements

The thickness of a film was measured with a surface profiler (KLA Tensor P-10). The depth resolution of measurement is 0.1 nm. It has a diamond stylus, which when travels across the edge of the film on a flat substrate, would experience a vertical displacement (Figure 3.1). An electrical signal is generated from a magnet-coil coupler to give an estimate the step height.

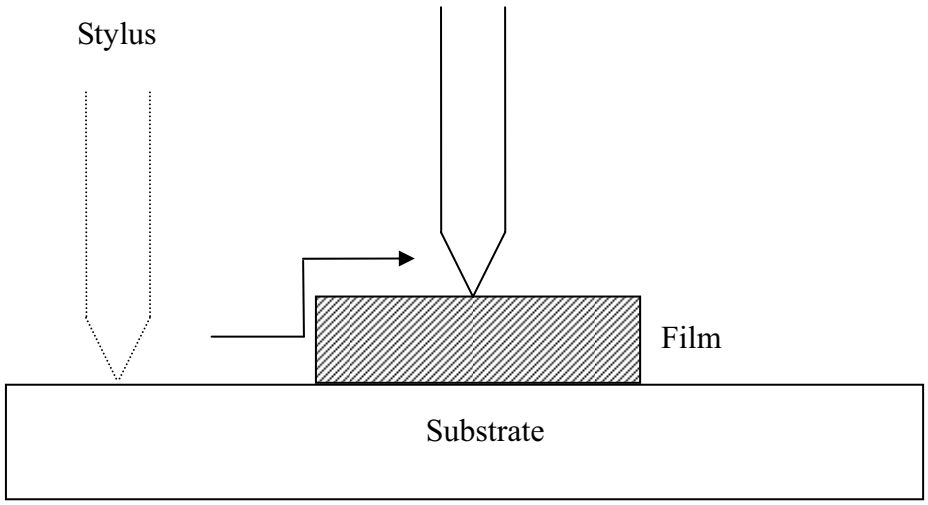

Figure 3.1 Schematic diagram of film thickness measurement by using a surface profiler.

3.2 X-ray diffraction

A Rigaku SmartLab (with Cu Kα radiation source of λ = 0.15418 nm) was used to investigate the X-ray diffraction (XRD) patterns of the films and their phases. The glancing-angle configuration (i.e. 2θ-scan) was employed. The glancing angle was adjusted to maximize the signal. A diffraction peak occurs when the Bragg condition

$$2\,d\sin\theta = \lambda \tag{3.1}$$

is satisfied, where d is the lattice spacing and θ the diffraction angle (Figure 3.2). The crystallite size L is estimated according to:

$$L = \frac{\lambda}{FWHM\cos\theta} \tag{3.2}$$

with FWHM being the full width at half maximum.

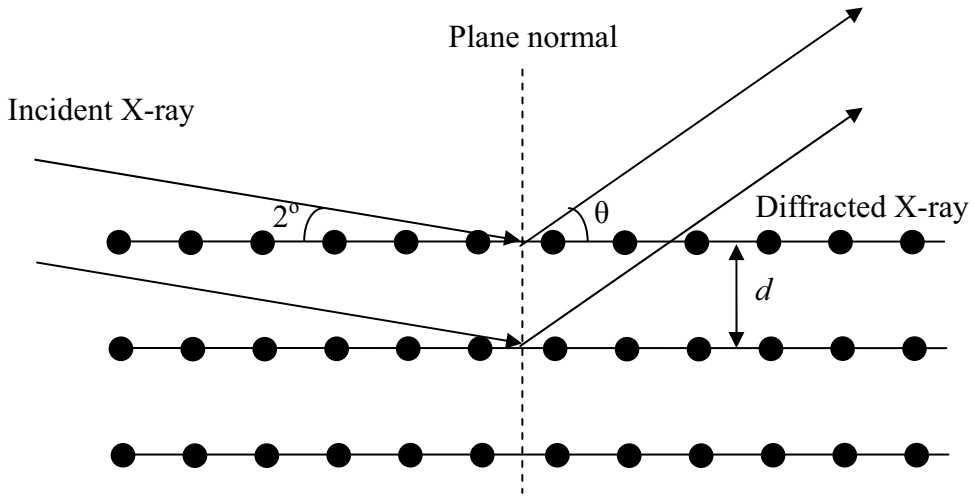

Figure 3.2 Schematic diagram showing the principle of X-ray diffraction.

3.3 Atomic force microscopy

The surface morphology and root mean square roughness (z_{rms}) of the samples were observed with an atomic force microscope (AFM, Vecco Nanoscope VIII system). The roughness of a film surface z_{rms} is expressed as:

$$z_{\mathrm{RMS}} = \sqrt{\sum_i \frac{z_i^2}{n}} \tag{3.3}$$

where z_i is the vertical height relative to the mean position, and n the number of the data points collected over $2 \times 2\ \mu m^2$.

3.4 Scanning and transmission electron microscopy

Figure 3.3 shows the phenomena associated with electron beam bombardment on a surface, from which information on topography, structure, composition et al. of the material can be achieved. In this study, a JEOL JSM-6335F field emission scanning electron microscopy (SEM) system was used to produce scanning electron micrographs of the film samples. A JEOL JEM-2011 transmission electron microscopy (TEM) system was used to collect structural information of the Pd/SCBD WO_3 films through observing the bright field images (due to un-scattered electrons) and selected area electron diffraction (SAED) patterns (due to elastically scattered electrons). The acceleration voltage was 200 kV.

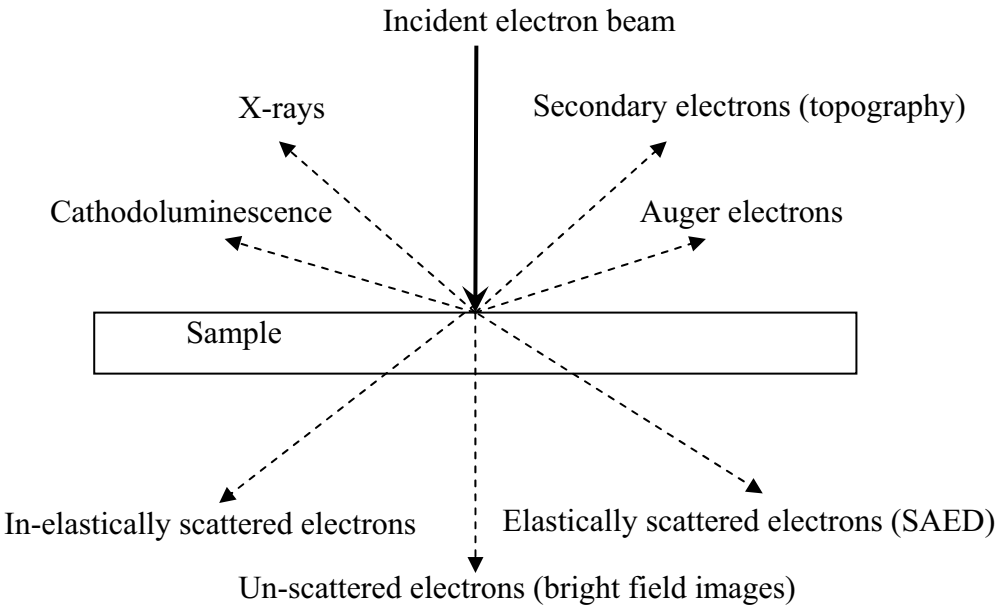

Figure 3.3 The interactions between incident electron beam and the sample.

3.5 Mirco-Rman spectroscopy

A HORIBA Jobin Yvon HR800 micro-Raman system was used to record the Raman spectra of the WO_3 films. It was operated in the backscattering geometry. The excitation beam was focused to give a spot size of 15 μm on a film surface. In general, photons may be scattered elastically without frequency shift (Rayleigh scattering); or scattered inelastically with positive or negative frequency shift (Stokes or anti-Stokes Raman scattering as shown in Figure 3.4). Molecules tend to be at the ground state, so that the Stokes Raman scattering signal is usually stronger. In this study, the data were used to analyze the relative abundances of bulk stretching

mode of the W^{6+}-O bonds and surface stretching mode of the W^{6+}=O terminal bonds of the WO_3 film samples according to the relative intensities of the two peaks. Results give qualitative information on surface-to-volume ratio of the film structure.

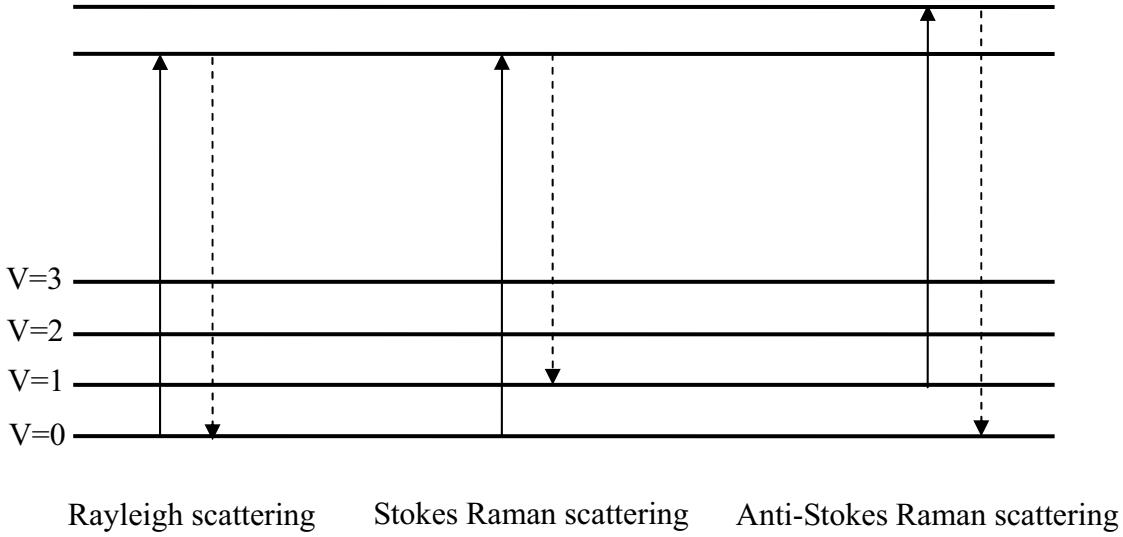

Figure 3.4 Schematic illustration of Rayleigh, Stokes, and Anti-Stokes Raman scattering.

3.6 Porosity measurements

The MO_x films could have very different porosity, which affects their gas sensing properties significantly. In this work, two methods were used to estimate the porosity of the WO_3 films. They are the Clausius-Mosotti equation method and mass-equivalent thickness method.

3.6.1 Clausius-Mosotti equation method

In this method, the refractive index n_f of the WO_3 films was first measured by using a Metricon 2010 prism coupler (Figure 3.5). A film sample was held by pressing it with a pressure of 50 psi against the prism base by means of a pneumatic coupling head, leaving an air gap around 100–200 nm between the sample and prism. An incident laser beam (wavelength λ = 632.8 nm) strikes on the base of a prism and is reflected onto a photo detector. The incident angle, α, can be adjusted continuously with a motorized rotary table. At a certain α, the light can be coupled into the film and enters the optical propagation modes. When sharp dips in the reflection spectrum are observed, the reflective index n_f is obtained as:

$$(2\pi/\lambda)n_f \cdot \cos\alpha \cdot t + \Psi_{10} + \Psi_{12} = m\pi \qquad m = 0, 1, 2, \ldots \tag{3.4}$$

where t is the film thickness and Ψ_{10} and Ψ_{12} are the Fresnel phase shifts at film-air and film-substrate interfaces. From the data of at least two modes, n_f and t can be calculated. Note that the samples used in this experiment were made on glass with a refractive index n_g = 1.53 at 632.8 nm.

Porosity of a film, θ, can be expressed as $(N_c - N_f)/N_c$, where N_f and N_c are the number densities of WO_3 molecules in the film and bulk WO_3 crystal respectively. It is related to the reflective indexes through the Clausius-Mosotti equation [118]:

$$(N_c - N_f)/N_c = 1 - \left(\frac{n_f^2 - 1}{n_f^2 + 2}\right)/\left(\frac{n_c^2 - 1}{n_c^2 + 2}\right) \tag{3.5}$$

where $n_c = 2.5$ is the refractive indexes of the film and bulk WO_3 crystal. From the measured n_f, the value of $(N_c - N_f)/N_c = \theta$ can be derived. Note that for the measurements of n_f, a set of film samples with thicknesses exceeding 700 nm was prepared. Hence, the distance travelled by the light beam in the film is comparable with the wavelength of 632.8 nm of the laser beam used in the measurements, such the result obtained can be used to represent the refractive index of a bulk material and the Clausius-Mossotti relation is applicable in estimating the value of θ.

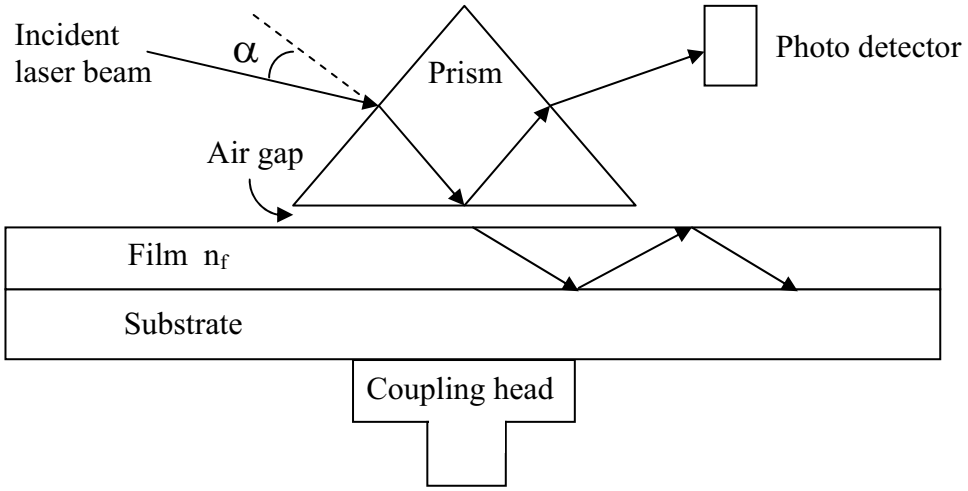

Figure 3.5 Schematic illustration of the working principle of the Metricon 2010 prism coupler.

3.6.2 Mass-equivalent thickness method

This method is suitable to be used for a highly porous sample (e.g. SCBD WO_3 film). It is better than the prism coupled method for no need to apply a force to hold

the sample during measurement, such that the film material is not deformed and error is avoided. It starts with measuring the mass of an as-deposited tungsten metal film with a quartz monitor. After oxidation, the mass of the WO_3 film was calculated. The mass-equivalent thickness of the WO_3 film was then derived. It was compared with the real thickness directly read out from a TEM image or an α-step surface profiler (Tencor P-10, accuracy ±1 nm). The former one was constantly smaller, and the porosity of the SCBD WO_3 film was estimated from the fraction difference between them.

3.7 Gas sensor characterization system

A home-made system was used to characterize the gas sensing properties of our film samples. The setup allows electrical and optical response of a sensor to be determined concurrently. It also allows gas concentrations (including interferants), temperature, total pressure, photo illumination and relative humidity to be varied independently in broad ranges. Performance indexes of a gas sensor, including sensor response, stability, selectivity, response time and recovery time, can be measured and correlated with various measurement conditions. It is computerized for the ease of performing long lasting or multi-cycle measurements to facilitate stability tests. Rapid gas exchange is realized by coordinating the operation of a rotary pump (for fast evacuation) and electrical/pneumatic valves for accurate determination of

response rate. More details are given in the following.

3.7.1 Configuration of the system

Figure 3.6 is a block diagram of the system. The pipeline consists of several sets of MKS mass flow controllers (MFCs) and valve assemblies (V). Each of the parts labeled as "MFC1" and "MFC2" contains two MFCs working in the ranges of 0–20 and 0–200 sccm of flow rate respectively, allowing the gas flow to be controlled in a broad range. Each of the valve assemblies labeled as V1–V14 has a bellow pneumatic valve (Swagelok, Model SS-4BK-1C) activated with a 3-way solenoid valve (SMC, Model VT307-5G-01). The system also has a mixing chamber and a sealed water chamber. A gas mixture sample containing the target gas, interferant(s) and balancing gas with specific compositions is formed in the mixing chamber. Moisture can be introduced by passing the gas sample through the water chamber. P1 is a capacitive absolute pressure sensor working in a range of 0–10 Torr (MKS, Model 122A-12225). P2 to P4 are MEMS-type pressure sensors working in a range of 0–2 atmospheric pressure (Honeywell, Model ASDX030A24R). This combination allows the pressure in the measurement chamber varying in a broad range to be determined.

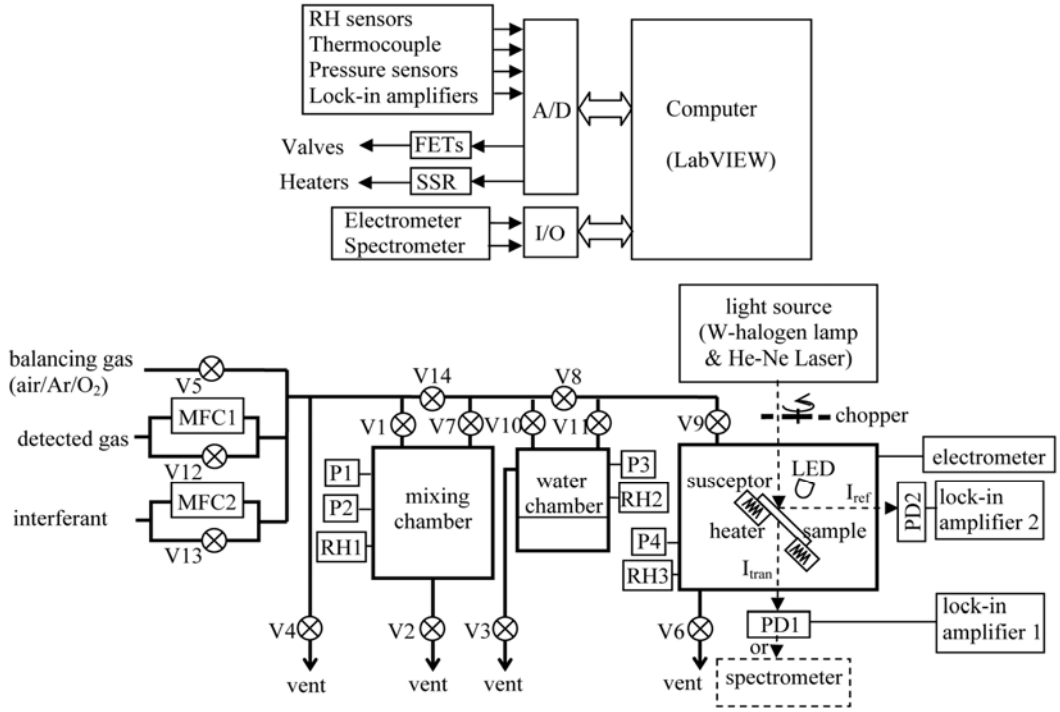

Figure 3.6 Gas sensor measurement system. V: valve; MFC: mass flow controller; P: pressure sensor; RH: relative humidity sensor; PD: photodiode; A/D: analog digital converter; FET: field effect transistor; SSR: solid state relay; I_{ref}: reflected light beam; I_{tran}: transmitting light beam.

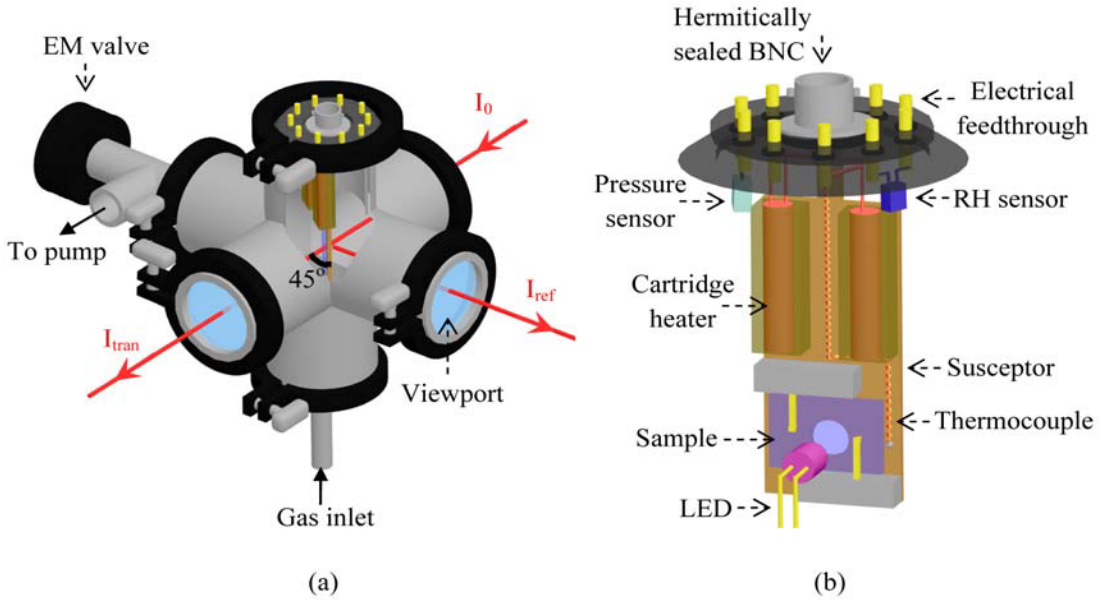

Figure 3.7 (a) Measurement chamber, (b) Top flange and the attached components.

Figure 3.7 (a) is a 3-D drawing of the 6-way measurement chamber of the measurement system. The electrical feedthroughs are mounted on the flanges. Three of them are equipped with glass viewports for optical measurements. One flange has a ¼" pipe for gas admission. One flange is mounted with an electromagnetic (EM) valve and connected to a 2-stage mechanical pump for venting. Figure 3.7 (b) shows the top flange, which has a hermitically sealed BNC socket at the center position for the measurements of the sample's resistance; and electrodes connected to two cartridge heaters (Hawco, Model HS25-2); a K-type thermocouple, a pressure sensor (Honeywell Model ASDX030A24R), an relative humidity (RH) sensor (Sencera, 805H5V5, detection range of 0–100%), and an LED. The sample holder is made of a copper plate equipped with two cartridge heaters which has good thermal contact with the copper plate.

In a measurement, the film resistance across the electrode gap was recorded with a Keithley Model 617 electrometer. The process was fully automated with a computer program compiled in LabVIEW 2010. The condition of a test is specified with pressure, temperature and RH in the chamber. The pressures in the mixing chamber, water chamber and measurement chamber can be detected by using Sensor P1 to P4. Temperature of the sample was detected by a thermocouple adhered to the sample holder. RH value was determined by Sensor RH1 to RH3. These data were sent to the computer through an analogue digital (A/D) module (NI, Model USB-

6281) as shown in Figure 3.6. The computer program generated feedback signals to control the valves for evacuating the chambers; and mixing up the target gas, interferant(s) and balancing gas according to the desired composition. The temperature was used to modify the duty cycle of an MOSFET-solid state relay (SSR) to keep the sample at the desired measurement temperature. The resistive change of the film was recorded and displayed.

3.7.2 Basic operation and control

We describe a typical measurement process as follows.

Step1: Valve V1, V2 and V3 are opened to pump down the mixing chamber and water chamber with the rotary pump. The valves are then closed after the measurement chamber reaches a pressure ≈ 0.15 Torr. Meanwhile, all other valves and MFCs are closed.

Step 2: MFC1 is activated to feed the detected gas into the pipeline. The flow is initially unstable, so that V4 is opened for about 10 s to wait for the flow to be steady. It is then closed and at the same time V1 is opened to release the detected gas into the mixing chamber. Until the pressure detected by P1/P2 reaches the set point, MFC1 and V1 are closed to stop the gas flow. The number of moles of the detected gas in the chamber is derived either from the duration of the flow or the pressure detected. A required amount of certain interferant can also be introduced with similar

process through another channel controlled by MFC2.

Step 3: A balancing gas, e.g. air, pure oxygen or argon, is fed into the mixing chamber by opening V5 and V1. The valves are closed after reaching the targeted pressure. The molar ratio of the constituents in the mixture, namely gas sample in the test, is fixed.

Step 4: The measurement chamber is then pumped down by opening V6. Until the pressure drops to ≈ 0.15 Torr, Valve V7, V8 and V9 are opened to release the gas sample into the measurement chamber and react with the gas sensing material. The valves are finally closed at equilibrium.

Step 5: This step is applied if the influence of RH on the gas sensing properties of a material is investigated. Valves V7 and V10 are opened for the gas sample to enter the water chamber for adding some moisture. The level of RH is detected. The measurement chamber is pumped down by opening V6. Until reaching a pressure ≈ 0.15 Torr, V6 is closed, and V11 and V9 are opened to release the gas sample to react with the gas sensing material. Valve V7, V10, V11 and V9 are closed at equilibrium.

Step 6: The resistive and/or optical responses of the sample material are recorded.

This basic testing process can be modified and recombined with great flexibility to meet the purposes of various studies.

3.7.3 Some remarks on the system

Flexibility and versatility: Our system is flexible in controlling many measurement parameters to vary independently in broad ranges, including concentration of the detected gas component, temperature, RH, content of interferant, type of balancing gas, total pressure, and intensity and wavelength of assisting light beam. It is thereby powerful in revealing the influences of different operation conditions on the gas sensing properties of a sample.

Control of gas composition: The gas mixing technique facilitates adjustment of the composition the sample gas mixture. Let us start with 4% H_2-Ar (or N_2) bottled gas. To dilute the gas, one could release the gas to a chamber by using the 20-sccm MFC. The accuracy of the MFC is 2% of the full span of an MFC, namely 0.4 sccm of the mixture, or equivalently 0.016 sccm of a net H_2 flow. If the flow lasts for 10 s, a volume of 0.0067 cm^3 of H_2 is injected into the chamber. More balancing gas is then introduced to dilute H_2. If the final pressure is 1 atmospheric pressure, and the volume of the mixing zone is 2350 cm^3, the H_2 concentration attained is ≈ 1 ppm. The dynamic range of H_2 concentration available is 1–40000 ppm. The maximum value is achieved by directly using the undiluted gas from the bottle. Further dilution of H_2-containing testing gas can be attained if starting from a bottle containing more dilute H_2.

Low consumption of gas: The consumption of gases is very low compared

with continuous gas flow technique employed by many other groups [3, 119-123]. A measurement applying continuous flow method needs to keep the gas flow to continue throughout the test. Consider a net H_2 flow of 0.016 sccm as an example. A balancing gas flow of 16000 sccm is required to dilute H_2 to 1 ppm. To perform a measurement condition under 1 atmospheric pressure, a typical cylinder containing 6.8 m^3 would exhaust in about 7 hours, such that the test is uneconomical. Contrarily, in our system, the target gas mixture is confined in a closed system mostly to allow the response signal to approach equilibrium. Consumption of gas only occurs when changing the gaseous atmosphere through pumping, which involves very little consumption of the gas.

Accuracy in response time measurement: Accurate determination of response time of a gas sensor depends significantly on how fast the gaseous atmosphere can be changed from one to another in a test. In continuous flow method without pumping [119, 121], the change of target concentration relies on diffusion and hence is not sharp enough. In our system, evacuation of the measurement chamber is accomplished with a vacuum process, allowing rapid exchange between the sample gas admixture and background gas inside the measurement chamber. The accuracy of response time measured with our system is thereby limited by the maximum acquisition rate of the electrometer (Keithley Model 617) used for collecting the signals, which is known to be 1 s.

Chapter 4 H_2 sensors made of a Pd film of controllable connectivity deposited on compliant Si pillar(s)

The importance of Pd-based HILE-type hydrogen sensors has been pointed out in "Introduction". A sensor of this type contains electrical isolation gaps (like gaps or clacks), which can be closed in a H_2-containing environment due to the HILE effect, such that a sharp resistance drop is induced. The sensor has a high sensor response and fast response rate. However, when it is exposed alternatively to the H_2-free background and a H_2-containing environment, the volume of the Pd film fluctuates, causing successive enlargement of the width of the isolation gaps and subsequently instability of the sensor response [16, 62, 68, 72, 75, 84, 85, 93, 95]. We tried to alleviate these problems by employing a new approach with the following features to fabricate HILE-type sensors.

(i) A Pd thin film is deposited on the top of a single Si pillar or a 2-dimensional (2-D) Si pillar array. The size and distribution of the isolation gaps in the film become adjustable by changing the dimension of the Si pillar(s); the thicknesses of an insulating buffer layer and the Pd film.

(ii) The Si pillar(s) is made to have a large height-to-thickness ratio and is easily bent for releasing some stresses generated by the HILE effect.

(iii) The fabrication process is based on typical Si-based micromachining technology and physical vapor deposition, and hence is potentially scalable.

Results associated with the sensors based on a single Si pillar and 2-D Si pillar arrays are presented in Sections 4.1 and 4.2 respectively.

4.1 H_2 sensor made of a Pd film deposited on a Si pillar

4.1.1 Device design and working principle

The design of the sensor based on a Pd film on a single Si pillar is shown in Figure 4.1 (a). The structure achieved in each step of the fabrication process is described as follows.

(i) A Si pillar with a width of 1 mm and thickness of 2500 nm is fabricated on a Si wafer [Figures 4.2 (a–b)]. The widths of the two isolation gaps beside the pillar are 2000 and 2600 nm respectively.

(ii) The pillar has a height of about 75 μm as seen in the cross-sectional SEM image [Figure 4.2 (c)]. The height-to-thickness ratio is as large as 30, making the pillar to be very compliant.

(iii) A 3-μm thick SiO_2 buffer layer was sputtered on the tip of the pillar. The isolation gap sizes beside the pillar were reduced to 430 and 900 nm respectively [Figure 4.2 (d)]. It is worth noting that their magnitudes can be

adjusted in a controllable manner by varying the thicknesses of the pillar and the SiO_2 layer through adjusting the parameters set in the micro fabrication processes and the conditions of the sputtering process (e.g. sputtering power, pressure and substrate temperature). The pillar has a mushroom-headed shape [Figure 4.2 (e)], which is more achievable with physical vapour deposition process rather than chemical vapour deposition or thermal oxidation processes.

(iv) Figure 4.2 (e) shows the Au/Cr bi-layered electrodes produced on the two sides of the pillar. The thicknesses of the Au and Cr layers are 100 and 10 nm respectively.

(v) Finally, a 1200-nm Pd layer was sputtered on top [Figure 4.2 (f)]. Its adhesion to the substrate is enhanced by the presence of the Au/Cr layer. One of the isolation gaps is founded to be closed by the Pd film, and the width of the other was further reduced to 300 nm. The Au/Cr electrodes were then wire-bonded to a print circuit board for electrical measurements.

The two Au/Cr electrodes are electrically isolated in a H_2-free background. When the structure is exposed to H_2 of high enough concentration, the Pd film would experience a volume expansion. The Si pillar is pushed from one side, such that it is bend to close the isolation gap on the other side. Electrical short between across the electrodes occurs to result in a percolation-like resistance drop.

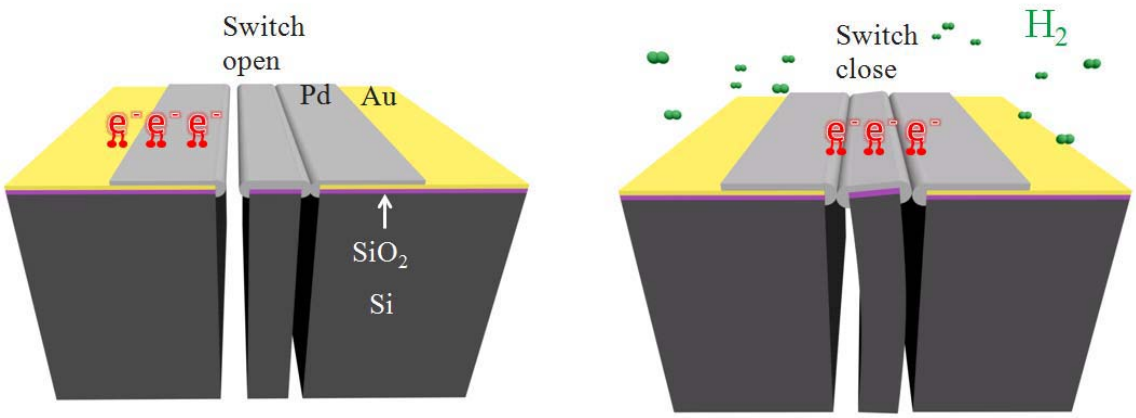

Figure 4.1 Skematic diagrams showing the structure and working prinicple of a H_2 sensor made of a Pd film deposited on a 1-D Si pillar in (a) H_2-free background and (b) H_2-containing environment.

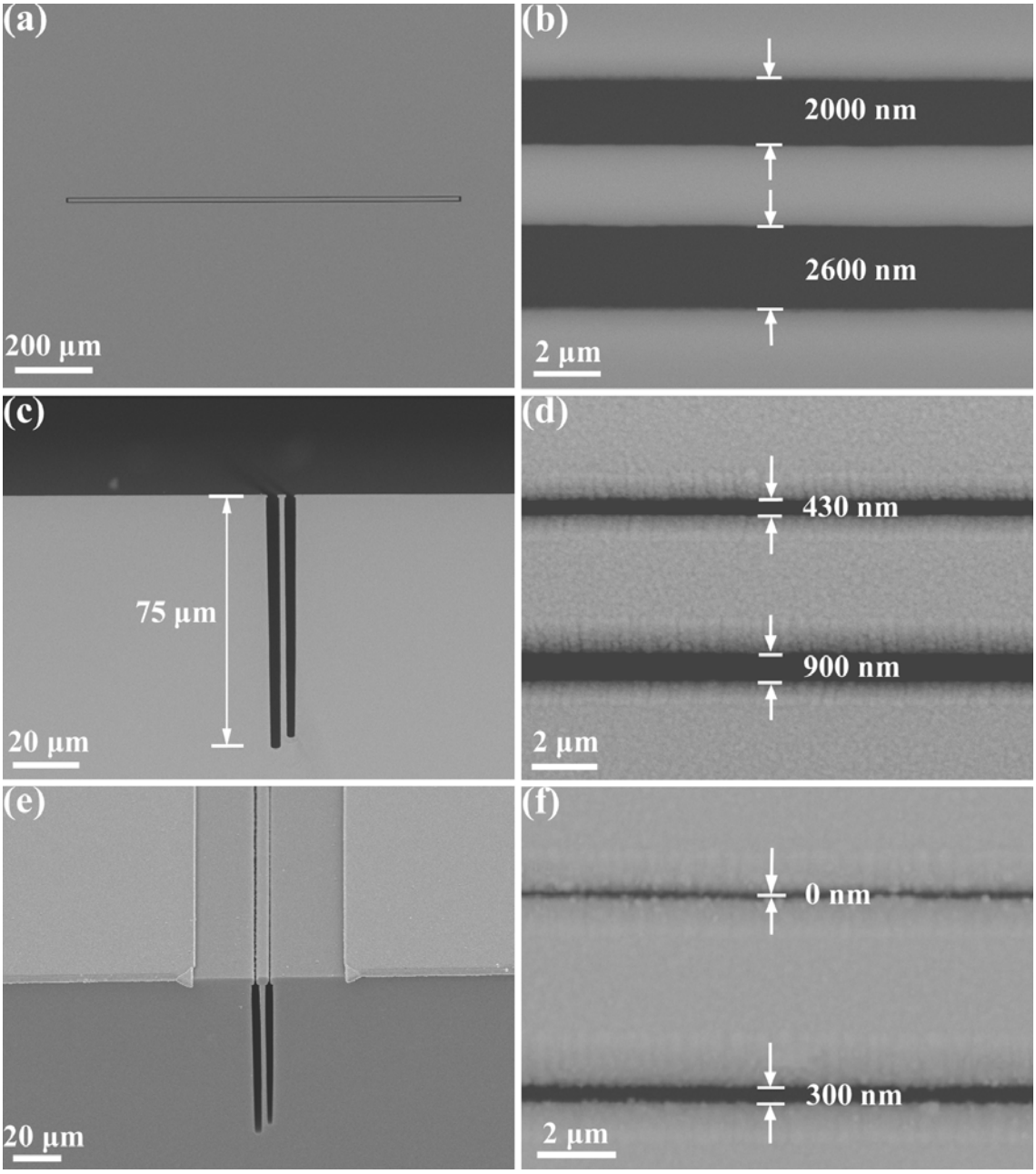

Figure 4.2 SEM images captured at different steps of fabrication of the sensor with a Pd film on a single Si pillar. (a, b) Top view of the Si pillar. (c) Cross-sectional view of the pillar. (d) Top view showing reduction of gap size by adding a SiO_2 layer. (e) Cross-sectional view showing the mushroom-headed geometry of the pillar and the Au/Cr electrodes. (f) Top view after deposition of a Pd film.

4.1.2 Results and discussion

4.1.2.1 Temperature dependences of sensor response, response and recovery times

The resistive sensor response of the sensor exposed to 4% H_2 in air measured at operation temperature $T_{operate}$ = 20, 40 and 60°C are shown in Figure 4.3, from which the $T_{operate}$ dependences of the base resistance in air R_o; the stabilized sensor resistance at 4% H_2 $R_{4\%H_2}$; sensor response S; response time $t_{respond}$ and recovery time $t_{recover}$ are derived and tabulated in Table 4.1. More details are described in the following.

Consider R_o first. The values measured at the three $T_{operate}$ are all around 21 kΩ, indicating that R_o is practically independent on $T_{operate}$.

Next, consider $R_{4\%H_2}$. The values measured at the three $T_{operate}$ are considerably smaller than R_o by more than 1000 times. Furthermore, when $T_{operate}$ increases from 20 to 60°C, $R_{4\%H_2}$ increases from 7.85 to 20.71 Ω. We further interpret this result as follows. According to Sieverts' law [22], the relative content of H to Pd in the hydride is:

$$\left(\frac{\mathrm{H}}{\mathrm{Pd}}\right)_{at} = K_s \times \sqrt{P_{H_2}} \qquad (4.1)$$

P_{H_2} is the H_2 partial pressure, and K_s is the Sieverts constant which depends on $T_{operate}$ in the form of:

$$\ln K_S = \frac{\Delta_s S}{R} - \frac{\Delta_s H}{RT_{\text{operate}}} \tag{4.2}$$

where $\Delta_s S$ and $\Delta_s H$ are the entropy and enthalpy, and R is the molar gas constant. Hydridation of Pd in a H_2-containing environment is a spontaneous process, so that $\Delta_s H$ is negative. From Eqs. 4.1 and 4.2, $(H/Pd)_{at}$ would drop with increasing $T_{operate}$. Consequently, in a hydridation process, the magnitude of the increase of the film resistance relative to R_o due to increase of the resistivity of the material is smaller. At the same time, magnitude of drop of the film resistance relative to R_o due to increase in connectivity of the Pd film caused by the HILE effect is also smaller. The sum of the resistance changes due to these two effects determines the overall change of the film resistance change in the process. In the present case, the HILE effect dominates, so that the stabilized resistance $R_{4\%H_2}$ is lower than R_o and hence $R_o - R_{4\%H_2}$ is positive. Furthermore, the magnitude of $R_o - R_{4\%H_2}$ decreases with increasing $T_{operate}$. This quantity is used to calculate the sensor response, S, defined as $(R_o - R_{4\%H_2})/R_{4\%H_2}$, which magnitude is reduced with increasing $T_{operate}$ as a consequence.

Both the $t_{respond}$ and $t_{recover}$ are found to decrease with $T_{operate}$. The inset of the Figure 4.3 shows details of the sensor's resistance with time. For a hydridation process carried out at 20°C, the sensor resistance first drops slowly from 21 kΩ to 19.5 kΩ within 46 s, and then drops abruptly to 25 Ω within 1 s. The former stage is for the Pd film to accumulate enough hydrogen content, until isolation gap is closed to produce a sudden short circuit-like response. The effective response time is

regarded to be 46 s. This effective response time is reduced to 5 s for a measurement carried out at 40°C, and is further reduced to < 1 s at 60°C.

The value of $t_{recover}$ is even more sensitive to the $T_{operate}$. In particular, at 20°C, $t_{recover}$ is longer than 1000 s, but becomes as short as 3 s at 60°C. The strong $T_{operate}$ dependences of the response and recovery times are expected because the adsorption, dissociation and hydrogen dissolution processes are accelerated by increasing $T_{operate}$.

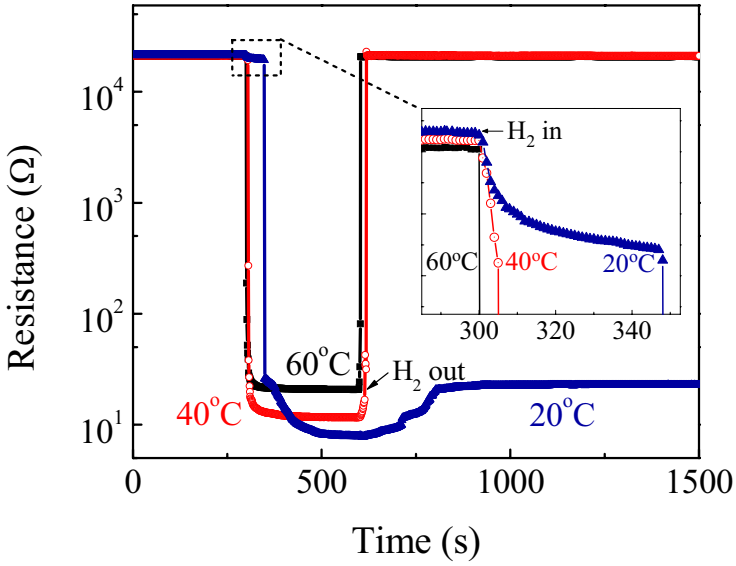

Figure 4.3 Resistive sensor response to 4% H_2 in air measured at 20, 40 and 60°C.

Table 4.1 Summary of sensor performance indexes measured at 20, 40 and 60°C respectively.

$T_{operate}$ (°C)	R_o (Ω)	$R_{4\%H_2}$ (Ω)	S	$t_{respond}$ (s)	$t_{recover}$ (s)
20	21270	7.85	2710	46	> 1000
40	21182	11.62	1823	6	16
60	21040	20.71	1016	< 1	3

4.1.2.2 Stability of sensor response

Figure 4.4 shows the resistive response of the sensor observed in a cyclic test performed at 60°C. The film sensor was exposed to 4% H_2 balanced in air and air alternatively. It is seen that the sensor response did not show any degradation over 30 switching cycles. This is an excellent feature superior to all reported HILE-type H_2 sensors. The supreme stability of the sensor can be explained by the following two reasons.

(i) From the theory of continuum mechanics, the deflection of the tip of the pillar z is

$$z = W H^3/(3EI) \tag{4.3}$$

where W is the force applied to the tip of the pillar in the lateral direction; H = 75 μm the length of the Si pillar; E = 200 GPa the Young's modulus of Si; and $I = ab^3/12$ the second moment of the pillar with a = 1000 μm and b = 2.5 μm being its width and thickness. The sensor design requires z = 0.3 μm to close the isolation gap and to start giving signal for H_2. W is estimated to be as small as 5.6×10^{-4} N. This force can be provided by an out-of-plane volume expansion of the Pd film as shown in Figure 4.5. The related normal compressive stress generated in the Pd film is estimated to be W/(ta) = 4.6 MPa, where t = 1.2 μm is the Pd film thickness. This value is far below the yield strength of Pd-H, i.e. 100 MPa. The sensor working at H_2 concentration around the onset level is

thereby expected to have satisfactory stability.

(ii) All of the HILE-type Pd-based H_2 sensors developed to date rely on in-plane strains to close the isolation gaps. If the sensor is made to have a film on a rigid substrate, the in-plane strains produced by the HILE effect would be accompanied by shear stresses [68, 72, 87, 90, 95]. Peeling off of the film could occur if the adhesion of the film to the substrate is not strong enough [25, 29, 68]. Plastic strains could also occur. All these deformations would result in irreversible change in the gas sensing properties of the materials. On the other hand, the operation of our sensor relies mainly on out-of-plane strains and hence is relatively less affected by the shear strength of the film-substrate interface. Furthermore, the out-of-plane normal strain of a film on substrate is usually larger than the corresponding in-plan normal strain (as if the former is magnified by the latter) [72]. As a consequent, the in-plane strain in our sensor corresponding to the onset of resistance rise in H_2 detection is smaller than those of other Pd-based HILE-type sensors relying mainly on the in-plane normal strains.

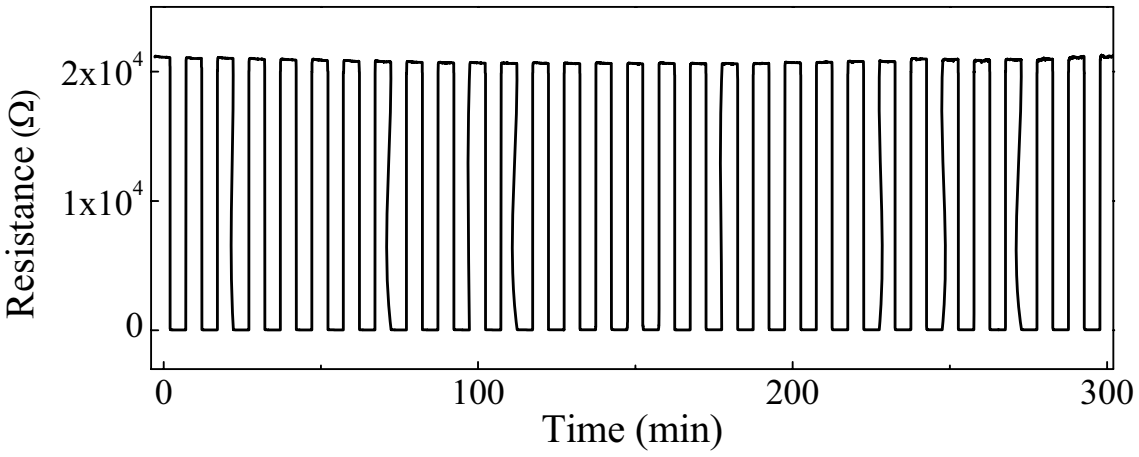

Figure 4.4 Resistive response of the sensor observed in cyclic tests performed at 60°C, by exposing the sensor to 4% H_2 (balanced in air) and air alternatively.

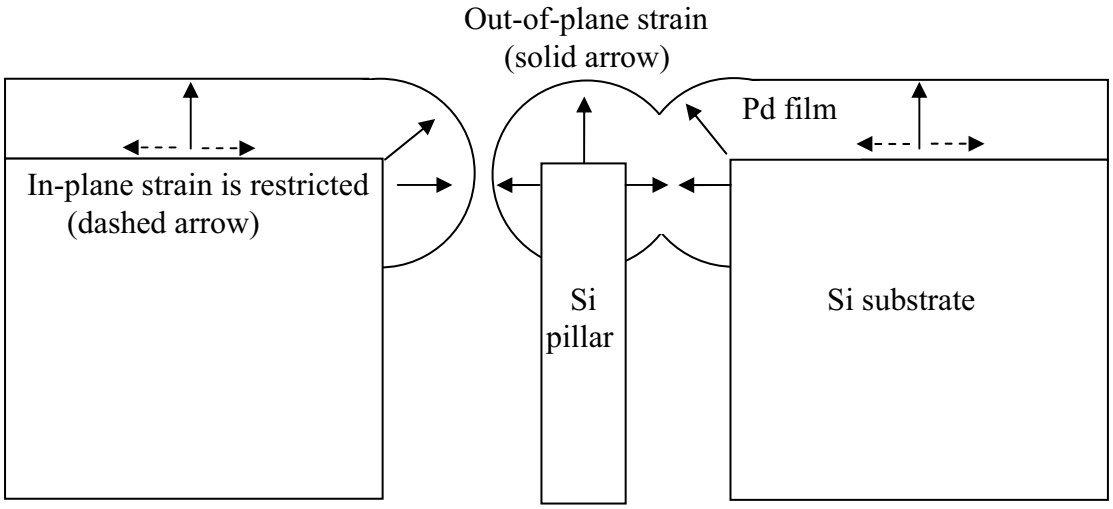

Figure 4.5 Proposed strain model for the H_2 sensor with a Pd film on a Si pillar.

4.2 H_2 sensors made of a Pd film deposited on 2-D Si pillar array

The H_2 concentration corresponding to the onset of the resistance rise for the above sensor with a single Pd-coated pillar is 4% (in air), which is determined by the width of the isolation gap ≈ 300 nm in this case. In another part of the study, we further fabricated sensor having Pd films deposited on 2-D Si pillar arrays with smaller isolation gap widths < 300 nm in order to demonstrate the feasibility of tailoring the detection range of H_2 concentration; sensor response; and response and recovery times through varying the pattern of the pillar array and the thickness of the Pd coating. Results are presented in this section.

4.2.1 Device structure and working principle

The configuration of a H_2 sensor made of a Pd film deposited on equally spaced Si pillars arranged in a 2-D array is shown schematically in Figure 4.6 (a).

Five samples, named as Sample A to E, were prepared for this part of study. Their structural information is tabulated in Table 4.2. The structure Sample A produced in each step in the fabrication process is described in the following as a typical example.

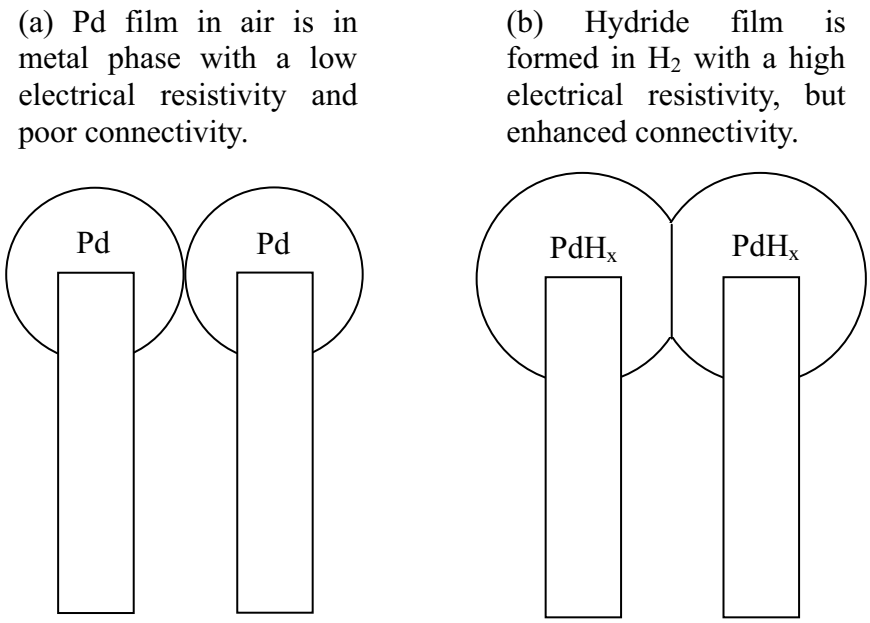

Figure 4.6 Skematic diagram of (a) the structure and (b) working principle of a H_2 sensor made of a Pd film deposited on a 2-D Si pillar array.

Table 4.2 Summary of the structural information of sensors used as H_2 concentration sensors.

Sample code	Initial Si pillar isolation gap width (nm)	SiO_2-isolation gap width (nm)	Buffer layer under the Pd film	Pd film thickness (nm)	Pd-isolation gap width (nm)
A	2200	100	No	400	0
B		150	No	400	50
C		300	No	400	150
D		300	Au/Cr 50/5nm	800	50
E		100	Au/Cr 50/5nm	400	0

Figures 4.7 (a–b) are the top views of a 2-D Si pillar array of different magnifications. Each pillar has a square-shape cross section with the edge size = 5 μm. The initial isolation gap width is 2.2 μm. Figure 4.7 (c) shows the cross-sectional view of pillar array. Figure 4.7 (d) is the top view of the array after depositing a 2.5-μm thick SiO_2 buffer layer on top. The isolation gap (SiO_2-isolation gap) width is reduced to 100 nm. Note that it was varied from 100 nm to 300 nm for Sample A to E (Table 4.2). Figure 4.7 (e) verifies that the sputtered SiO_2 layer is mainly located at the tips of the pillars, such that the Si pillars exhibit a mushroom-headed shape. One further sees that the Si pillars have a length of 60 μm, leading to a height-to-thickness ratio as high as 12:1. Figure 4.7 (f) is the top view of the Si pillar array after deposition of the Pd film. For Sample A, it is 400-nm thick and has even narrower isolation gaps, referred to as the Pd-isolation gaps hereafter. Figure 4.7 (g) is the image taken after adding the Pd film. Figure 4.7 (h) is the overall view of an assembly of nine such devices having Si pillar array of different Pd-isolation gap widths. In addition, for Sample D and E, an 50-nm Au/5-nm Cr buffer layer is deposited prior to the deposition of the Pd film, which functions are further described in section 4.2.2.2.

At the as-preparation stage, the isolation gaps in the Pd film are made to be partially closed, such that its (mechanical and electrical) connectivity and the in-plane electrical resistance is very sensitive to the degree of ensuing hydridation

process. The sensor is thereby capable of detecting H_2 concentration much lower than the onset value of the previous one based on one single Si pillar. Notice that the increase in electrical resistivity associated with increasing degree of hydridation persists (resistivity-mechanism). It leads to an opposite resistive response to cancel out part of the signal due to the HILE-mechanism. The actual sensor's response is the combination of the two.

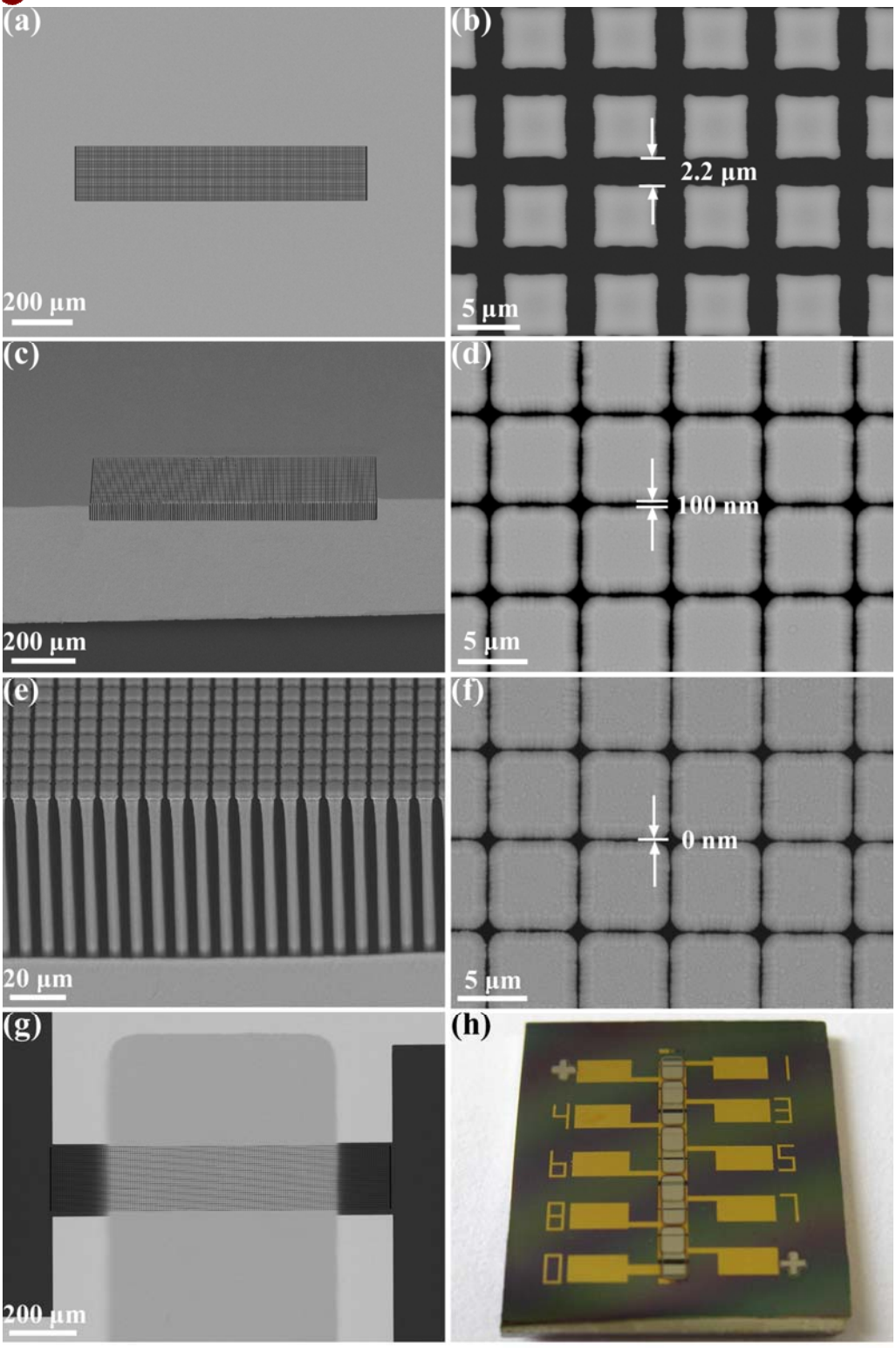

Figure 4.7 SEM images of the Si pillars (a–c) before and (d–e) after adding an SiO_2; (f) after adding a Pd film; (g) top view of as-fabricated device; and (h) an overall view of a chip carrying a few sensors having a dimension of 1.5×1.2 cm^2.

4.2.2 Results and discussion

4.2.2.1 Effect of Pd connectivity on the sensor performance

It is found that the H_2 sensing properties of the sensors are controlled by the (electrical and mechanical) connectivity of the Pd layer, which can be varied by adjusting the SiO_2-isolation gap width or the thickness of the Pd layer. These dependences and their physical origins are presented and discussed in the following.

Effects of varying SiO_2-isolation gap width

Figures 4.8 (a–c) show the variation of sensor resistance versus H_2 concentration (balanced in Ar) measured at 40^{o}C for samples of a 400-nm Pd film on the templates with increasing SiO_2-isolation gap widths of 100, 150 and 300 nm, referring to Sample A, B and C, respectively.

First, the base resistance R_o increases drastically from 86 to 338 Ω and then to 3.35×10^{11} Ω.

Second, the threshold H_2 concentration corresponding to the onset of steep resistance rise increases with increasing SiO_2-isolation gap width. Below the threshold H_2 concentration, HILE does not occur. In this region, the resistance rise is due to the "resistivity-mechanism" of the Pd film. Above the threshold H_2 concentration, HILE effect starts to dominate and gives significant drops of sensor's resistance. The magnitude of resistance drop slows down for further increase in H_2

concentration. Figure 4.9 shows the plot of the sensor response of Sample A and B against H_2 concentration. It illustrates the abovementioned features, and in addition, it shows that Sample A with a smaller SiO_2-isolation gap width has a larger sensor response in the low H_2 concentration region, which is due to the better starting connectivity of the Pd film.

Thirdly, Sample C of a largest SiO_2-isolation gap width of 300 nm does not show any measurable response to H_2 below a concentration of 6% [Figure 4.8 (c)]. With this behavior, it can be used as switching-type gas sensor as if the one based on single Si pillar described in Section 4.1.

The maximum sensor response increases with increasing SiO_2-isolation gap width due to the rise in R_o. It varies from 3.61 to 18, and finally to 1.02×10^9 for the three samples in sequence. Sample C has a normalized sensor response NS = 17000/ppm, which is the highest among all the HILE-type H_2 sensors reported so far.

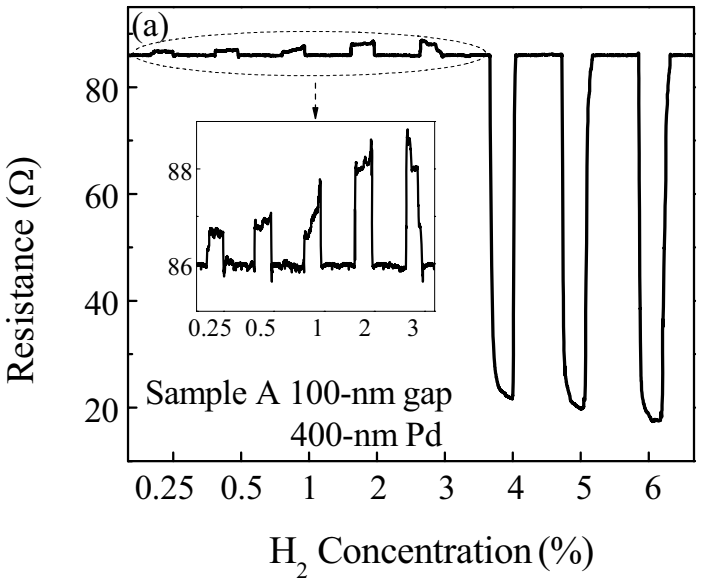

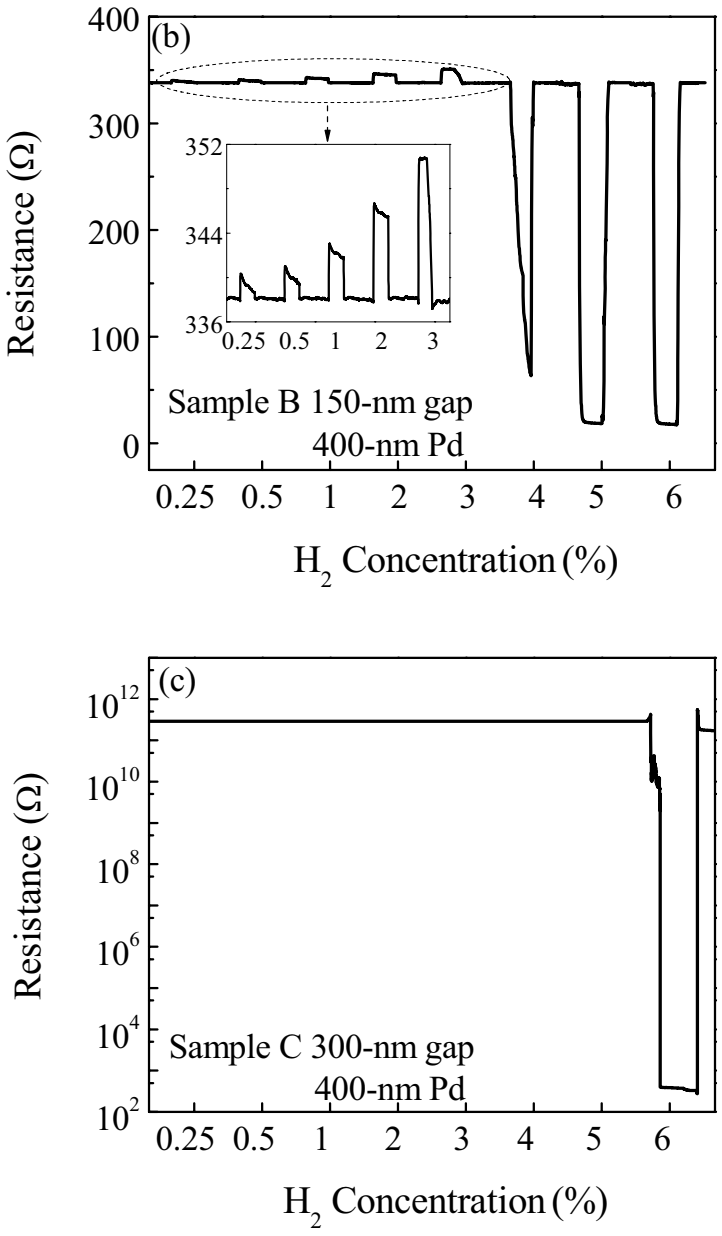

Figure 4.8 Resistive response against H_2 concentration (balanced in Ar) at 40°C for sensors of a 400-nm Pd film on pillar arrays with SiO_2-isolation gap widths equal to 100, 150, and 300 nm.

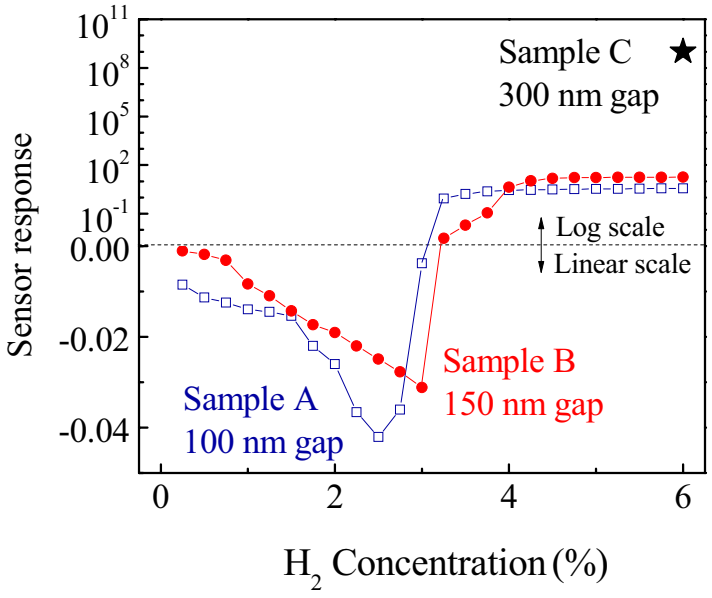

Figure 4.9 Sensor response against H_2 concentration of Sample A, B and C.

Effects of varying the Pd layer thickness.

The next is to compare the H_2 sensing performance of Sample C of a 400-nm Pd film and a Sample D of a 800-nm Pd film deposited on Si pillar arrays of the same SiO_2-isolation gap width of 300 nm (Table 4.2). Figure 4.10 (a) shows that R_o of Sample C is very high, i.e. 3×10^{11}, which is reduced to 90 Ω of Sample D. In addition, secondly, as shown in Figure 4.11 for the plots of sensor response against H_2 concentration, Sample D starts to show reliable sensor response S at a H_2 concentration of 0.5%, whereas Sample C only cannot give detectable sensor response S until the H_2 concentration rises to 6%. Figure 4.11 also shows that the maximum S of sample D is only 2.13, which is $1/5x10^8$ of that of sample C. All these

results are explainable by referring to the better connectivity of the thicker Pd film in Sample D, which leads to a low base resistance R_o. The practical meaning of these results is to confirm that the sensor properties of the film can be adjusted by varying the thickness of the Pd film.

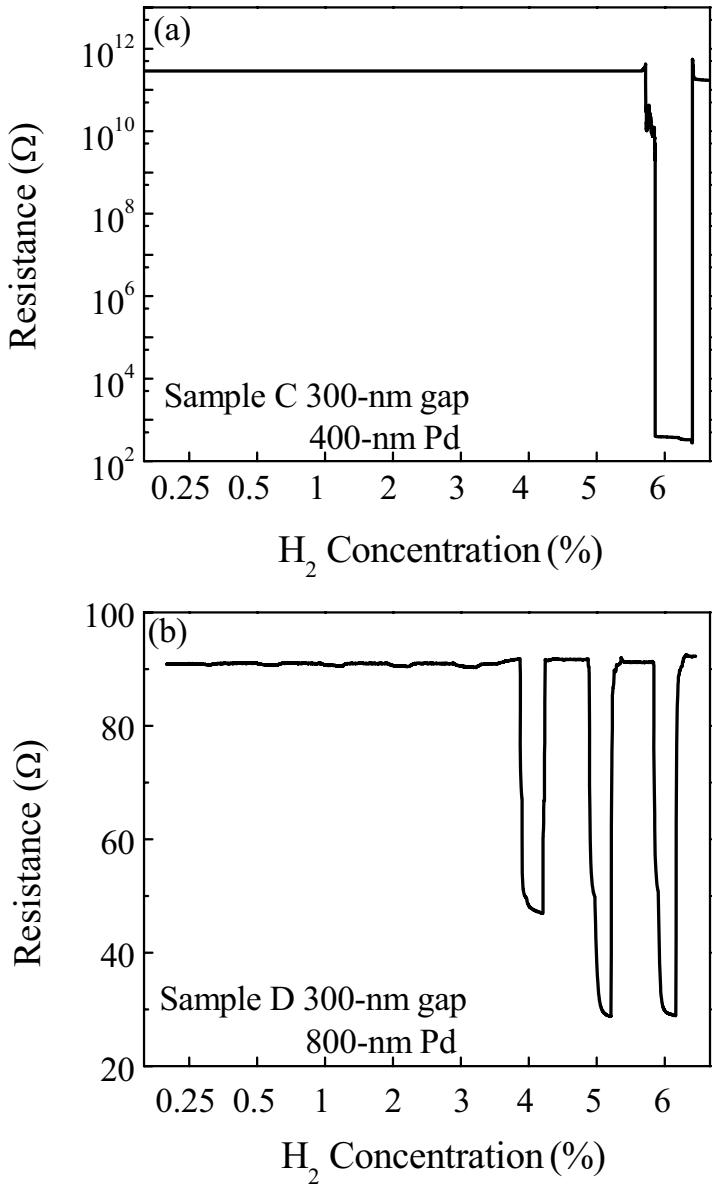

Figure 4.10 (a–b) Resistance change of a sensor against H_2 concentration (balanced in Ar) at 40°C having Pd films of thicknesses equal to 400 and 800 nm on 2-D Si pillar arrays for the same SiO_2-isolation gap width equal to 300 nm.

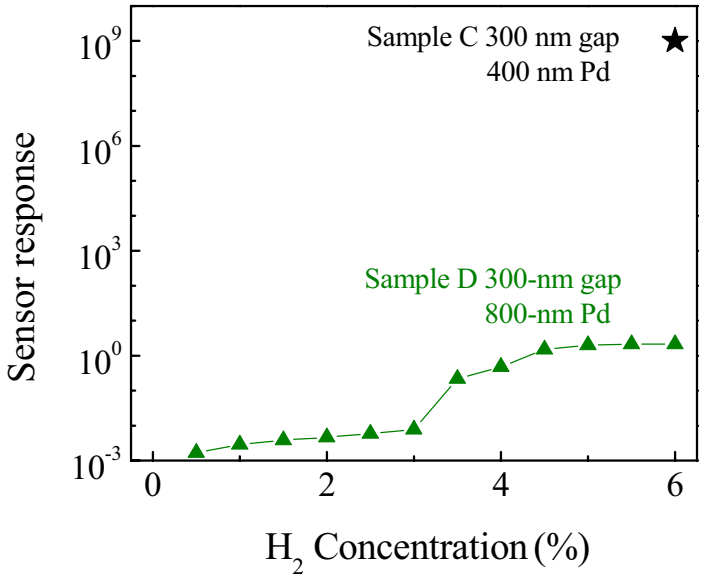

Figure 4.11 Sensor response against H_2 concentration for Sample C and D.

Practical meaning of controllability of the connectivity of the Pd film

According to the results of Sample A–D, one may conclude that the sensor response and its H_2 concentration dependence can be controlled by adjusting the connectivity of the Pd film, and the connectivity of the Pd film is precisely controllable by modifying the SiO_2-isolation gap width and Pd film thickness.

In fact, not only the performance of a single sensor of this type becomes tailorable, but also a certain number of sensors with Pd films having a spectrum of connectivity can be assembled to form a tailor-made multisensory array with any desired detection range of H_2 concentration.

The feasibility of this idea can be illustrated by referring to Figure 4.12, in which the plots of the sensor response versus H_2 concentration for Sample A to D are shown. Each of the curves of Sample A, B and D shows a sigmoidal transition part in

a specific range of H_2 concentration, but it is fairly well approximated by the linear relationship and can be readily handled with simple electronic circuits or microprocessors. More interestingly, the threshold H_2 concentration associated with the on-set point of the curves is systematically changeable according to the connectivity of the Pd film, or the transition region is "movable". Therefore, by integrating a group of sensors with different degrees of Pd film connectivity, like the sensor array containing nine sensor elements in a chip as shown in Figure 4.7 (h), the assembly can give very high senor response over a broad detection range of H_2 concentration. This is plan of the work in our future research plan.

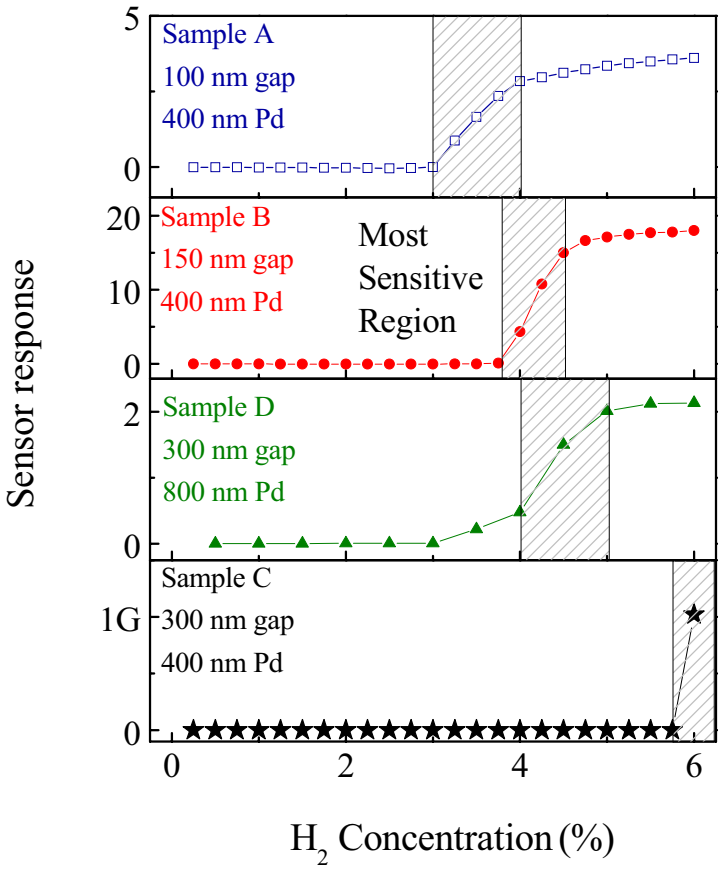

Figure 4.12 S-H_2 concentration curves of Sample A–D, shaded area indicates the most sensitive H_2 concentration range of individual sensors

4.2.2.2 Effect of Au/Cr buffer layer

Knowing that the overall resistance change of a sensor of this type is a joint result from the "resistivity-mechanism" and "HILE-mechanism", which are always interweaved together during operation. In this section, we describe how the former one can be eliminated by adding an 50-nm Au/5-nm Cr buffer layer between the SiO_2 buffer layer and the Pd film, such that a conductive three-layered structure Pd/Au/Cr is formed disregarding the degree of hydridation of the Pd film. Hence, the resistance change is entirely from HILE effect.

The resistance change and sensor response of Sample E and A, with and without a Au/Cr buffer layer respectively, against H_2 concentration are plotted in Figures 4.13 (a–b), with key information tabulated in Table 4.2.

Firstly, the based resistance R_o of Sample E, 35 Ω, is lower than that of Sample A, 86 Ω, because of the presence of the Au/Cr buffer layer in the former, considering that Au has a lower resistivity compared to Pd.

Secondly, in the low H_2 concentration region before the onset of HILE effect, the resistance of Sample E drops during hydrogenation, indicating the success of eliminating the contribution from the "resistivity-mechanism" by the presence of the Au/Cr buffer layer, which is still discernible in the corresponding plot of Sample A.

Thirdly, the maximum sensor response S of Sample E is smaller than that of Sample A, because part of the contribution from the HILE effect is cancelled out due

to the electrical shorting effect by the Au/Cr layer.

Furthermore, the sensor response of Sample E was observed in a broad range of H_2 concentration. Results show that it can give very clear response at 20 ppm of H_2 (Figure 4.14), which is lower than the lower detection limit of all the HILE-type H_2 sensors reported in literature so far. The sensor response then increases monotonically by 6% with increasing H_2 concentration up to the highest H_2 concentration employed in the test without showing saturation as observed by the other HILE-type sensors.

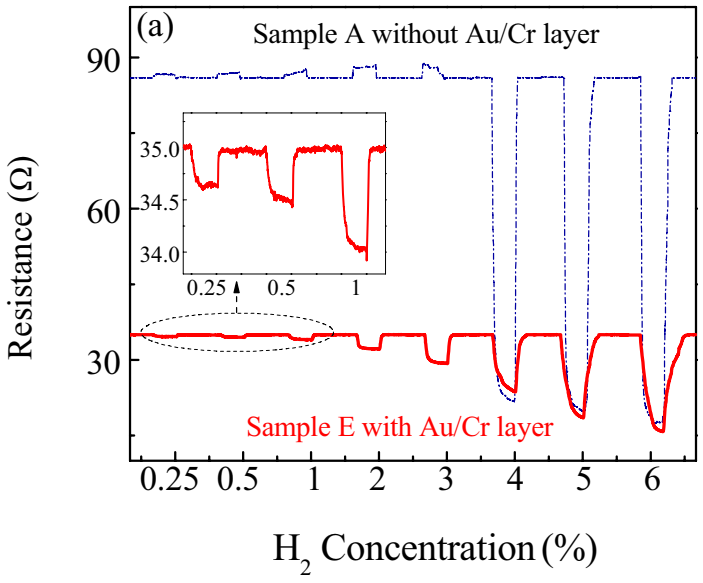

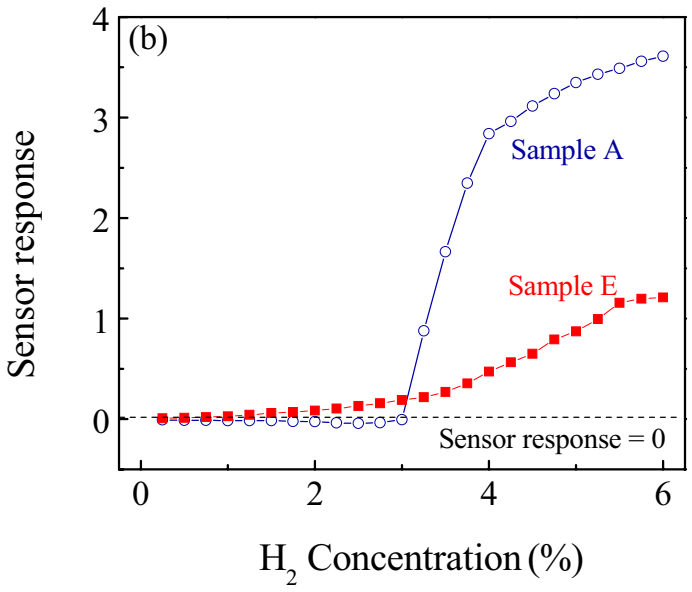

Figure 4.13 (a) Resistance change and (b) sensor response of Sample A and E against H_2 concentration based in argon at 40°C.

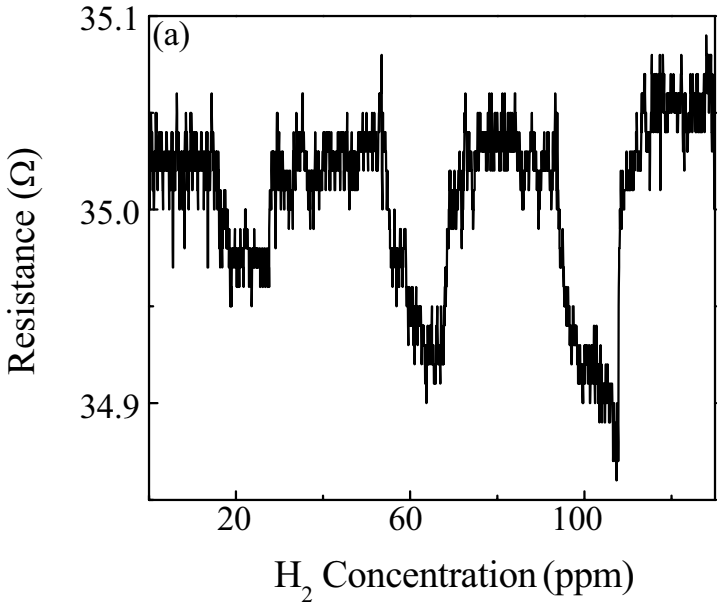

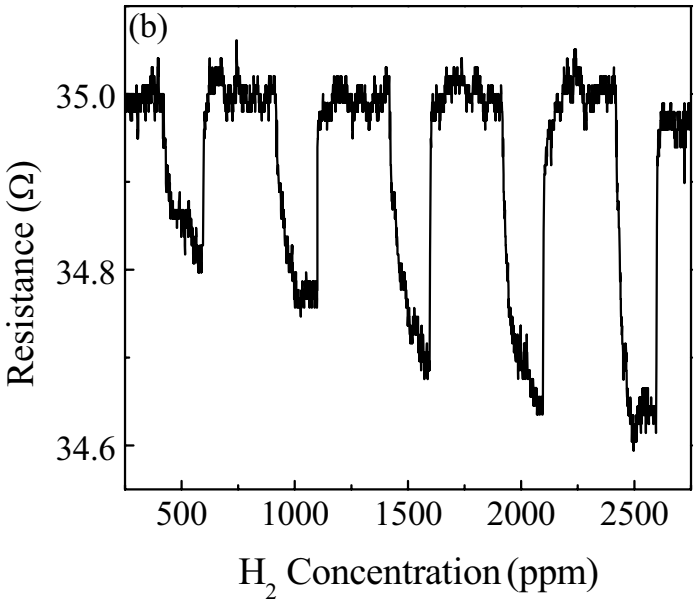

Figure 4.14 Resistance change of Sample E against H_2 concentration (balanced in argon) in the range of (a) 20–100 ppm and (b) 500–2500 ppm, measured at 40°C.

4.2.2.3 Effect of the operating temperature $T_{operate}$ on the sensor performance

The effect of $T_{operate}$ on the performance of a sensor was demonstrated by the results of Sample as an example. Figure 4.15 shows the resistance change of the sample in a hydrogenation process (with 4% H_2 in argon) and dehydrogenation (in air) measured at 20, 40 and 60°C, respectively. The performance indexes extracted from the results and tabulated in Table 4.3.

Firstly, the base resistance of the sensor R_o decreases from 90.6 to 80 Ω when $T_{operate}$ increases from 20 to 60°C. This trend is a result of two competing mechanisms. The rise in temperature would lead to thermal expansion of the Pd clusters at the tips of the pillars to result in a better electrical connectivity and a

lower R_o. On the other hand, the electrical resistivity of Pd would also increases with temperature to give a higher R_o. Obviously, the former mechanism dominates in this case to result in an overall drop of R_o.

Secondly, the stabilized resistance at hydrogenated state, $R_{4\%H_2}$, increases with $T_{operate}$. Similar trend is also found for the sensor of one single Si pillar (Section 4.1), whereas the explanation given in Section 4.1.2.1 is also applicable for in this case. In brief, the H content in the film drops with increasing $T_{operate}$, and HILE prevails the drop of the film resistance from R_o, which is reduced to give a rise in $R_{4\%H_2}$ and a monotonic drop of senor response S from 3.98 to 0.27.

At last, both $t_{respond}$ and $t_{recover}$ decrease with increasing $T_{operate}$ which can be attributed to the accelerated adsorption, dissociation and dissolution of H_2 (and the reverse of these processes) at a higher $T_{operate}$.

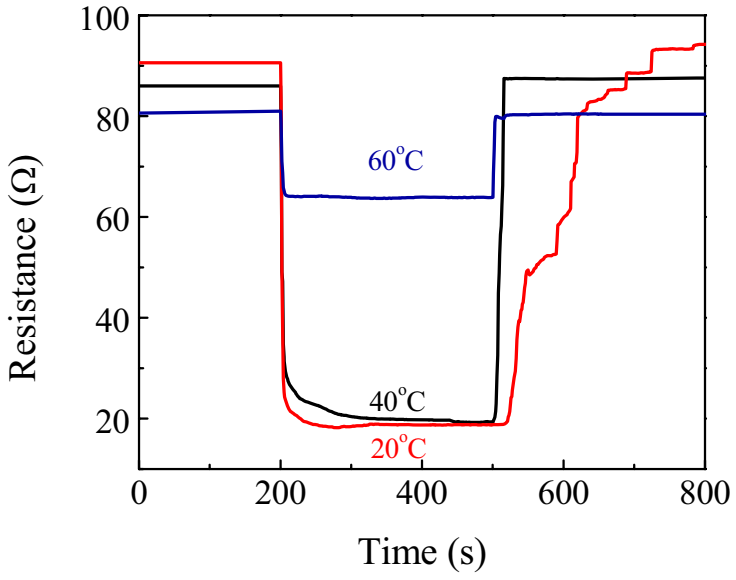

Figure 4.15 Resistance change of Sample A hydrogenated by 4% H_2 in argon and dehydrogenated in air measured at 20, 40 and 60°C.

Table 4.3 Summary of sensor performance indexes of Sample E measured at 20, 40 and 60°C.

$T_{operate}$ (°C)	R_o (Ω)	$R_{4\%H_2}$ (Ω)	S	$t_{respond}$ (s)	$t_{recover}$ (s)
20	90.6	18.2	3.98	5	150
40	86	19.2	3.48	4	23
60	81	63.8	0.27	3	3

4.2.2.4 Effect of the test ambient on the sensor performance

Figures 4.16 (a) and (b) show the resistive change and sensor response against H_2 concentration balanced in argon and air, respectively, at 40°C for Sample E. Results show that both of the parameters are stronger for H_2 balanced in argon, while the response and recovery times remain almost unchanged. It is believed that the presence of oxygen in air can reduce the equilibrium H content in the hydride. The HILE effect and hence the sensor response are weaker.

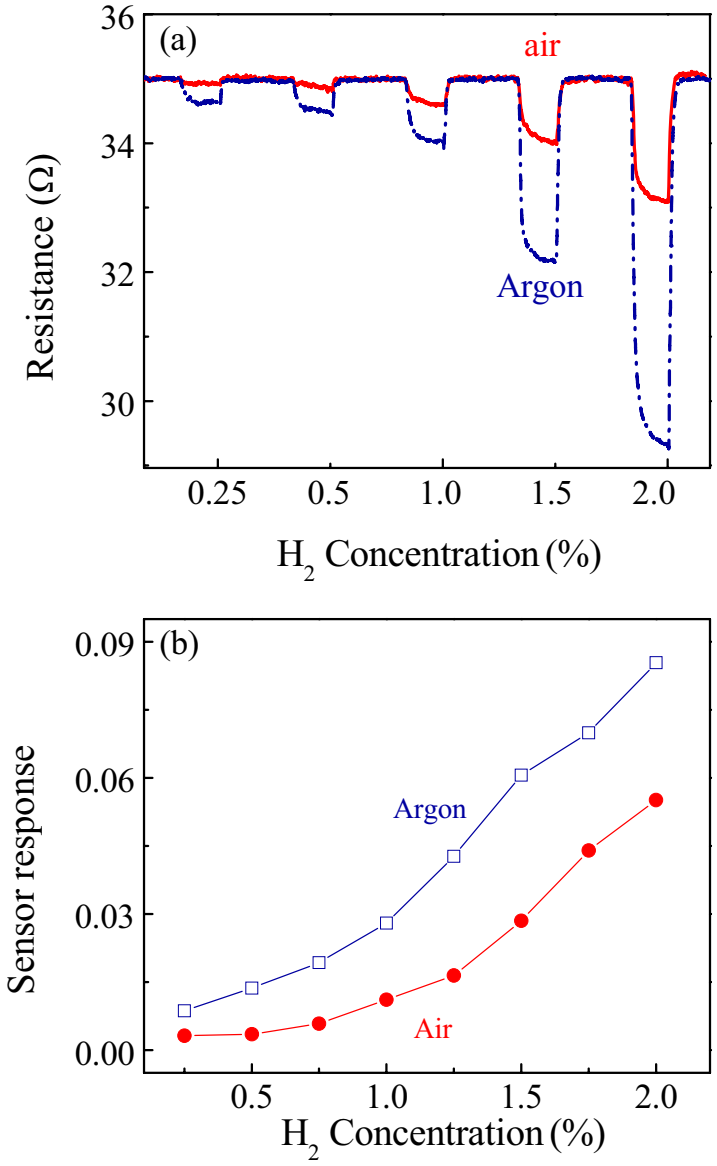

Figure 4.16 (a) Resistance change and (b) sensor response versus H_2 concentration balanced in Ar and air for Sample E at 40°C

4.2.2.5 Stability test

Figure 4.17 shows the resistance change of Sample D observed in a cyclic test performed at 50°C. The sensor was exposed to 5% H_2 in argon and synthetic air

alternatively for hydrogenation and dehydrogenation processes. The sensor response decreased by about 10% after 30 cycles. Such a result is still superior to most of other HILE-type H_2 sensors reported in literature. The deterioration of the sensor response is explained as follows. For Sample D with a SiO_2-isolation gap width of 300 nm, the Pd materials located on the tips of adjacent Si pillars could have the initial contact. When HILE effect occurs to build up stresses among them, the stresses generated from the Pd materials could be built up to reach the yield stress of the material and cause irreversible deformation. The H_2 concentration used in this test may have reached this level and hence progressive degradation of the sensor's properties is resulted. Addition of a polymer buffer layer under the Au/Cr may allow more compressive stresses to be released through elastic deformation of the polymer layer.

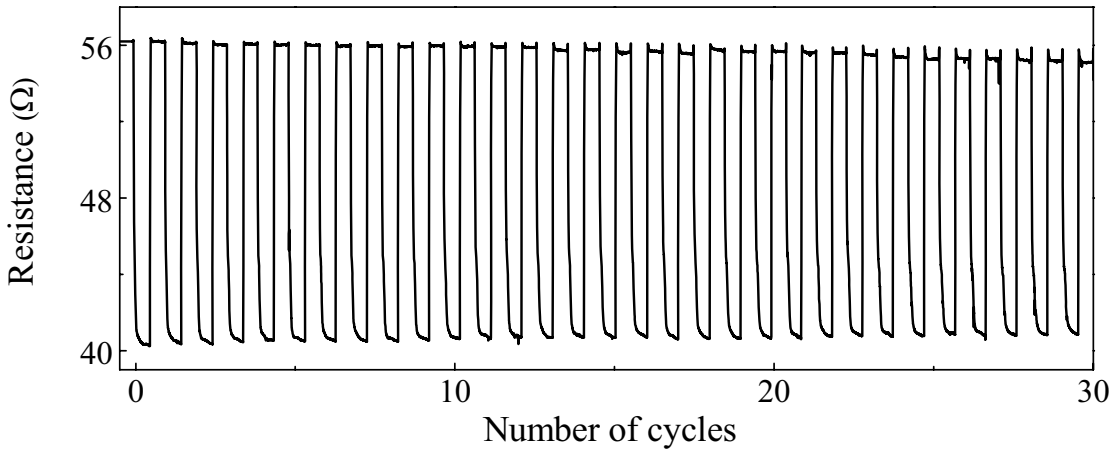

Figure 4.17 Resistance change of Sample D observed in a cyclic test performed at 50°C. The sample was exposed to 5% H_2 in argon and synthetic air alternatively for hydrogenation and dehydrogenation processes.

4.3 Comparison of sensor performance

4.3.1 Comparison with HILE sensors reported in literatures

Results of our Pd-coated Si pillar and Pd-coated 2-D pillar array are compared with those of some representative HILE-type sensors reported in literature. The structural information and performance indexes of all these sensors are tabulated in Table 4.4.

We note that the HILE-type sensors published in literature and selected for comparison are classified into two groups. Group 1 contains sensors made of Pd nanowire arrays, in which isolation gaps are generated by stresses during successive hydrogenation and dehydrogenation processes [61-70]. For example, as-fabricated Pd nanowires were continuous initially, but become more fragmented after performing a certain number of switching circles. The width of the isolation gaps in the Pd-based substance is enlarged successively from 50 to 500 nm. This makes the nanowire assembly to be more resistive and has a high base resistance R_o. The Pd-isolation gaps are hard to be closed, unless the H_2 concentration in the surrounding rises to a high level of ~ 2% (at 300K), where α-to-β phase transition occurs to induce substantial HILE to close the gaps and result in a great drop of the sensor's resistance. The normalized sensor response NS of this Group I of sensors is very large. On the other hand, after all the isolation gaps are closed, the connectivity of

the Pd nanowires is hardly to be enhanced further, explaining the fact that the sensor starts to be saturated when H_2 concentration > 5%. As a consequence, the detection range of sensor of this type is rather narrow (2–5% H_2), and NS is very large. The sensors are more suitable to serve as a H_2 leakage monitor rather than a H_2 concentration indicator. The response time ($t_{respond}$) of this group of sensors strongly depends on the compliance of the substrate. A more compliant substrate facilitates absorbing strains induced in the detection process. A $t_{respond}$ < 1 s can be achieved. $t_{respond}$ as long as 60 s is detected for Pd nanowires deposited on a rigid substrate.

Group II refers to (i) discontinuous thin film formed by isolated Pd islands on a substrate [71-78], and (ii) porous Pd films [79-83] or nanowires [84, 85] made of loosely connected Pd nanoparticles. A sensor of this group contains partially closed gaps. The connectivity is readily affected by the volume change of the Pd film, such that the lower detection limit LDL can be as low as several ppm [78]. On the other hand, the upper detection limit UDL can be made to reach 100% with appropriate number density of the Pd islands on the substrate surface [82]. Furthermore, due to the small gap width, the base resistance R_o is generally smaller than that of a Group I sensor. $t_{respond}$ depends strongly on the compliance of the substrate. It can be much shorter than 1 s by depositing Pd on a substrate coated with siloxane monolayer [78], and can be as long as 79 s for a Pd film deposited on a glass substrate [76].

Our H_2 sensor with a Pd film on single Si pillar is designed to have larger

isolation gap width, and hence is more analogous to a Group I sensor. They have comparable lowest detection limit LDL, upper detection limit UDL and normalized sensor response NS, which are mainly affected by the width of the isolation gaps in the Pd-based sensor element. In particular, NS of these sensors are estimated to be > 0.025. $t_{respond}$ and $t_{recover}$ of our sensor at 4% H_2 are about 1 s and 3 s respectively, which are slightly longer than those of a Group I sensor fabricated on epoxy substrates, and much shorter than those of another one fabricated on a SiN_x/Si substrate.

Our H_2 sensor made of a Pd film on a 2-D Si pillar array is more analogous to Group II sensors. The LDL of our sensor is as low as 20 ppm, which is smaller than those of all the sensors as listed in Table 4.4. The UDL of our sensor is 6% H_2, which is the highest achievable setting in our test, but the actual one could be even higher (as implied by Figure 4.13). It is smaller than those of two Group II sensor types as shown in Table 4.4. NS of our sensor is larger than those of all Group II sensors as shown. $t_{respond}$ and $t_{recover}$ of our sensor is shorter than those of two sensor types with rigid substrates, but is longer than those of a sensor made of Pd nanowire and a discontinuous film of Pd islands deposited on a siloxane layer. Even though the $t_{respond}$ and $t_{recover}$ of our film is not the fastest compared to the Group II sensors, they are already short enough to be used in many occasions, like hydrogen refuel stations, hydrogen plants, hydrogen pipe lines and semiconductor labs and industries et al.

The above comparison seems to indicate that not every performance index of our H_2 sensors made with a Pd film of Si pillar(s) prevails that of other HILE-type H_2 sensors reported in literature, but our sensors have the following distinctive superiorities which have not been achieved by others.

First, the H_2 sensing performance of our sensors is precisely controllable by accurate adjustment of the isolation gap width. On the contrary, in a typical Group I sensor, the isolation gaps in the Pd material are generated naturally during operation with no predictable geometry and distribution, such that the performance of the products produced with their approaches are entirely uncontrollable. Even worse, the sensor properties of a Group II sensor is very sensitive to the number density of the Pd islands or nanoparticles, which is usually needed to be close to the percolation threshold to make the response and response times fall in a reasonable range. Hence, even a small fluctuation of the uniformity of thickness of the sensor element would result in large variation of the gas sensing performance. One example is the sensor with an ultrathin Pd film onto a siloxane layer [78], where a tiny variation of the Pd thickness from 2.3 to 4.3 nm would cause the base resistance R_o to rise by 10000 times. Though the optimal one is known to be 3.3 nm, it is very difficult to achieve this dimension in an accurate and reproducible manner in mass production processes.

Second, the cyclic stability of our sensors is prominently superior to those of Group I and Group II sensors. For example, a sensor based on a single Si pillar can

have no degradation of sensor response over 30 switching circles, but many Group I sensors showed very poor cyclic stability after running a few switching cycles [62, 84, 95]. The cyclic stability of our sensors is attributed to the the highly compliant Si pillar(s) which deforms to release stresses generated in the Pd film. Also, the operation relies mainly on the out-of-plane strains of the Pd film, unlike many other HILE-type sensors rely on in-plane strains such that the shear stresses induced at Pd/substrate interface tend to affect the adhesion of Pd nanowires and films, or to alter configuration of the isolation gaps in the nanowires or films and hence the stability of the sensor performance.

Third, our sensors are fabricated by using standard Si micromachining and sputtering techniques, which ensure the reproducibility and high throughput of mass production. One roughly estimates that over 7000 Pd/Si pillar and pillar-array sensors can be fabricated on one 4-inch Si wafer. Differently, some other HILE-type sensors are fabricated with processes which are not convenient to be scaled up, like Pd nanowire-based sensors which need to be deposited on a conducting substrate and then transferred to another insulating substrate with the use of epoxy [61-63, 65]; or a discontinuous Pd film which uniformity and number density of Pd islands on the substrate surface can affect the sensing properties significantly [73, 75-80, 82, 83].

Another potential advantage of our sensor is the possibility of making sensor array by assembling a certain number of sensor elements of different isolation gap

widths on a single chip, which can give high sensor response to the target gas over a very broad range of concentration.

Table 4.4 Summary of the structural information and performance indexes of HILE-type H_2 sensors.

Structural Information			**Sensing Performance**				
Morphology	Substrate	Gap size [nm]	LDL [%]	UDL [%]	NS @ H_2 concentration [/ppm]	$t_{respond}$ [s]	$t_{recover}$ [s]
Our study—Pd film coated on Si single pillar or pillar array							
Pd film (this study)	Flexible Si pillar	300	4	4	0.025 @ 4%	< 1	3
		Partially closed	0.002	> 6%	9×10^{-5} @ 4%	3–4	3–23
Group I: Nanowires with stress induced fracture—large gap size, high sensor response							
Compliant substrate—short response time							
Nanowires [62]	Epoxy	50	2.25	5	> 0.025 @ 5%	0.07	0.07
Nanowires [70]	Epoxy	200–400	2	5	> 0.025 @ 5%	< 1	< 1
Nanowires [63]	Epoxy	100–300	3	4	0.01 @ 4%	< 1	< 1
Rigid substrate—long response time							
Nanowires [66]	SiN_x/Si	500 c.a.	4	4	0.005 @ 4%	60	60
Group II: Island films, porous film/nanowires—small gap size, low sensor response							
Compliant substrate—short response time							
Island film [78]	Siloxane	Partially closed	0.0027	5	2.5×10^{-5} @ 2%	0.07	0.6
Rigid substrate—long response time							
Island film [76]	Glass	Partially closed	1	10	5×10^{-6} @ 10%	79	103
Porous film [82]	SiO_2/Si		0.4	100	2×10^{-5} @ 100%	2–30	30
Nanowires [85]	SiO_2/Si		0.02	5	2×10^{-7} @ 5%	1–10	1–10

4.3.2 Comparison with commercialized H_2 sensors

The H_2 sensing properties of the Pd/Si pillar and pillar-array sensors are compared with those of the commercialized H_2 sensors. Data are tabulated in Table 4.5.

(i) The lowest detection limit LDL of a Pd/Si pillar(s) sensor is about 20 ppm, which is lower than those of all commercialized H_2 sensors. Furthermore, its upper detection limit UDL is only smaller than those of thermal conduction (TC) type and Pd-based resistivity-type sensors. More importantly, we have demonstrated that the detection range of H_2 concentration of a Pd/Si pillar(s) sensor is adjustable through controlling the width of the isolation gaps in the sensor material. In addition, a number of Pd/Si pillar arrays can be assembled to form a multisensor system to give high sensor response covering the full measurement range of H_2 concentration from 0 to 100%.

(ii) The normalized sensor response NS of a Pd/Si pillar(s) sensor is only smaller than that of MO_x-type H_2 sensor, and is much larger than those of other sensor types. The greatest advantage of the Pd/Si pillar(s) sensor over the commercialized H_2 sensor is its ultrafast response rate (< 1 s). Such a short response time makes the sensor an ideal H_2 leakage monitor in H_2-driven vehicles.

(iii) Currently, the durability of the Pd/Si pillar(s) sensor is satisfactory based on the fact that the H_2 sensing properties of a sensor prototype fabricated one year ago do not show any significant change up to date. Moreover, the cyclic stability of a Pd/Si pillar(s) sensor is good enough for many practical applications.

(iv) The operate temperature $T_{operate}$ and hence the power consumption of the Pd/Si pillar(s) sensor are much lower than those of other commercialized sensor types except for the ones belonging to the electrochemical (EC) ones.

(v) The Pd/Si pillar(s) sensor can be fabricated by mature Si-based micromachining techniques. Therefore, the sensor is readily miniaturerized and fabricated with great reproducibility, such that production cost can be lowered. We have demonstrated that the sensor volume can be less than 1 mm^3, which is much smaller than all existing sensors and facilitates its use in devices powered by hydrogen fuel cells. Furthermore, the samples were fabricated by applying Si-based micromachining technique. One roughly estimates that over 7000 sensors can be produced one a 4-inch Si wafer. This corresponds to a cost of around one US dollar per sensor.

Other performances of the Pd/Si pillar(s) sensor, such as relative humidity dependence, environmental temperature dependence and the ambient pressure dependence will be examined in the near future.

Table 4.5 Performance indexes of major existing types of H_2 sensor products and the Pd coated Si pillar(s).

	MO_x-type sensor	**EC-type sensor**	**CC-type sensor**	**TC-type sensor**	**Pd resistivity type sensor**	**Pd/Si pillar**	**Pd/Si pillar array**
LDL	50 ppm	100 ppm	> 100 ppm	1000 ppm	5000 ppm	40000 ppm	20 ppm
UDL	≤ 2 %	≤ 4 %	≈ 4 %	≤ 100 %	≤ 100 %	4% ppm	> 6% ppm
NS (ppm^{-1})	0.15/ppm at 2% H_2 [51]	0.002/ppm at 1.15% H_2 [55]	5.3×10^{-4}/ppm at 1% H_2 [57]	2.5×10^{-6}/ppm at 10% He [60]	7.6×10^{-7}/ppm at 2% H_2 [35]	0.025/pppm at 4%H_2	9×10^{-5} /ppm at 4% H_2
$t_{respond}$	5–20 s	30–60 s	10–30 s	10–50 s	< 60 s	<1	3–4
Static lifetime Cyclic lifetime	5 years no data	2 years no data	3–5 years no data	5 years no data	5–10 years no data	no data >30	no data >30
Selectivity	affected by reducing gases	affected by reducing gas_{es}	affected by combustible gases	good	good	good	good
Atmospheric pressure dependence	strong (80–20 kPa)	mild (90–110 kPa)	weak (80–120 kPa)	weak (70–130 kPa)	no data (80–100 kPa)	no data no data	no data no data
$T_{operate}$ $T_{environ}$ $T_{environ}$ dependence	400–500°C -20 to 80°C strong	-20–50°C ditto moderate	400–500°C -20–80°C weak	100–200°C 0–50°C strong	120°C -20–0°C strong	60°C no data	40–60°C no data
RH dependence (observed range)	strong (10–95%)	weak (15–90%)	nil (0–95%)	weak (0–95%)	nil (0–95%)	no data	no data
Batch–to–batch reproducibility	poor	poor	good	good	good	good	good
Miniaturizability	difficult	difficult	difficult	difficult	yes	yes	yes
Power consumption	> 500 mW	< 100 mW	> 500 mW			< 100 mW	
Unit price (USD)	300–500 USD	1200 USD	1700 USD	> 1000 USD	> 2000 USD	≈ US 1 (material cost)	

4.4 Conclusions

In summary, HILE-type H_2 sensors were fabricated by deposition a Pd film on a single Si pillar or a 2-D Si pillar array. This approach has the follow important features:

(i) The width and distribution of the isolation gaps in the Pd film can be precisely controlled to tailor the sensor performance. The connectivity of the Pd film and the degree of compliance of the Si pillar can be adjusted to achieve the desired response rate. Excellent cyclic durability can be achieved via absorption of strains in the Pd layer through the bending of the Si pillar(s).

(ii) The designs allow the products to be miniaturized, for the production process to be scaled up with high batch-to-batch reproducibility. Note that the advantages mentioned in Point (i) and (ii) have not been achieved concomitantly by other methods employed so far for fabricating HILE-type sensors.

(iii) An Au/Cr buffer layer can be added between the Pd film and substrate to eliminate the influence of the resistivity-mechanism, which gives an opposite resistive response to that due to the HILE-mechanism.

(iv) The sensor response, response time and recovery time decrease with rising $T_{operate}$. These results are all explained by the reduced H content in the Pd-H hydride at the equilibrium stage.

(v) The sensor response to H_2 is reduced if the gas is balanced in oxygen instead of an inert gas like argon.

From application point of view, a Pd coated single Si pillar has a large sensor response (> 1000); short response time (< 1 s); short recovery time (3 s); and excellent stability over 30 circles. It is thereby suitable for the use of giving H_2 leakage warning signal. The Pd coated 2-D Si pillar array has very broad detection range of H_2 concentration covering 20 ppm to over 6%; high normalized sensor response exceeding those of other HILE-type sensors; short response time of 3–4 s and short recovery time of 3–23 s. It is thereby suitable for the use of direct measurement of H_2 concentration.

The results obtained in this part of study inspire us to propose a research topic on developing multisensor array by assembling the sensor elements of different isolation gap widths for making a sensor system capable of detecting H_2 with concentration varying in a very broad range.

Chapter 5 Hydrogen sensors made of palladium-coated nanocluster-assembled highly porous tungsten oxide films

In this study, we hope to realize the idea of producing high-quality metal-oxide (MO_x) thin film gas sensors made of a-few-nanometer grains and having an extremely high porosity. This is inspired by the finding that rare research type gas sensors claimed to be "nano" can possess these two features concomitantly. However, if the grain size is close to the thickness of the oxide's depletion layer, the grains are deeply depleted in air to show a high resistance, but become rather conductive when a reducing gas appears to remove the oxygen ions. The high porosity allows the gas to diffuse much faster.

The idea was implemented by producing thin film hydrogen (H_2) sensors made of loosely connected tungsten oxide (WO_3) nanoclusters deposited by using supersonic cluster beam deposition (SCBD) coated with a thin palladium (Pd) film deposited by using sputtering to enhance catalytic dissociation of H_2. The general concept of the fabrication process of an SCBD film has been described in Chapter 2. The H_2 sensing performance of the sensors, including sensor response, response and recovery rates, cyclic stability, ambient pressure dependence, relative humidity dependence, selectivity against various organic compound (VOC) vapours etc. were

measured. Possible physical mechanisms involved in the detection processes are discussed.

Also considering that a conventional MO_x gas sensor usually needs to operate at temperature $T_{operate}$ of 300–500^oC which may cause material annealing effect and subsequent thermal drift of the sensor's output, many recent studies are performed to pursue lowering of $T_{operate}$ for MO_x gas sensors. Room temperature operation condition is confirmed to be achievable, but further investigations are carried out in this study to optimize the overall performance of the sensors at some moderate $T_{operate}$.

5.1 Film structure

An as-deposited film was a metal tungsten film showing a dark appearance. After annealed at 250^oC for 12 hrs, it became highly transparent and was expected to be oxidized. To investigate the oxidation stage, measurements of the film's optical transmission were carried out. As shown in Figure 5.1 (a), a high transmittance exceeding 90% was observed in the visible range. Figure 5.1 (b) further shows the Tauc plot, from which the film's optical band gap is estimated to be 3.1 eV. This value is consistent with that of crystalline WO_3 [124, 125], suggesting that the film is fully oxidized to the WO_3 stoichiometry.

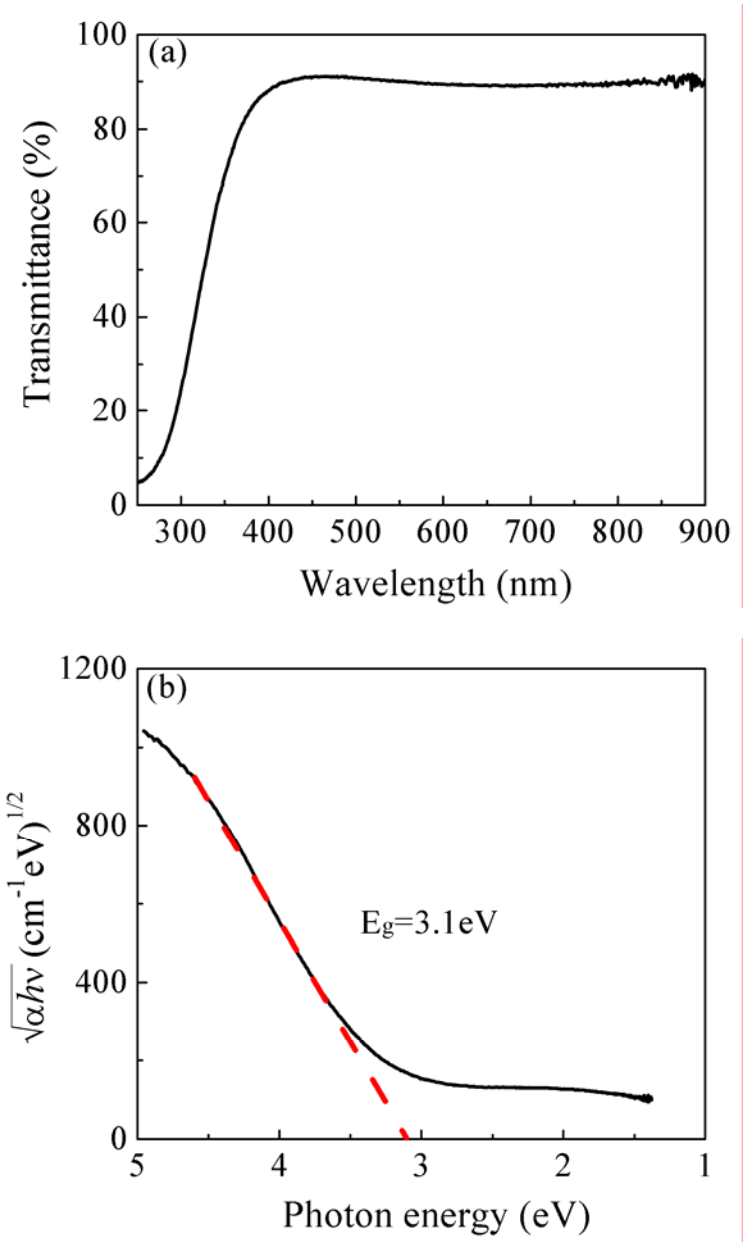

Figure 5.1 (a) Transmittance and (b) Tauc plot of an annealed SCBD WO_3 film.

The next is to investigate the presence of nanoclusters in the oxide film and their size. Figure 5.2 (a) is an SEM image of an annealed SCBD WO_3 film without a Pd coating. It shows that the film surface is very rough and has many nano-sized pores. Figure 5.2 (b) is a cross-sectional TEM image showing the layered structure

of the film. One sees clearly the presence of a 5-nm Pd surface coating on the top of a 140-nm WO_3 layer. Figure 5.2 (c) is another cross-sectional TEM image with a larger magnification selected from a region close to the film surface. It shows the presence of Pd gains. The inset shows a mixed electron diffraction patterns of them. Figure 5.2 (d) is a cross-sectional TEM image selected from a region located deeper under the film surface. It shows the presence of 3~5 nm WO_3 nanoclusters. Lattice plains are found in some regions indicating that extremely tiny crystallites are formed.

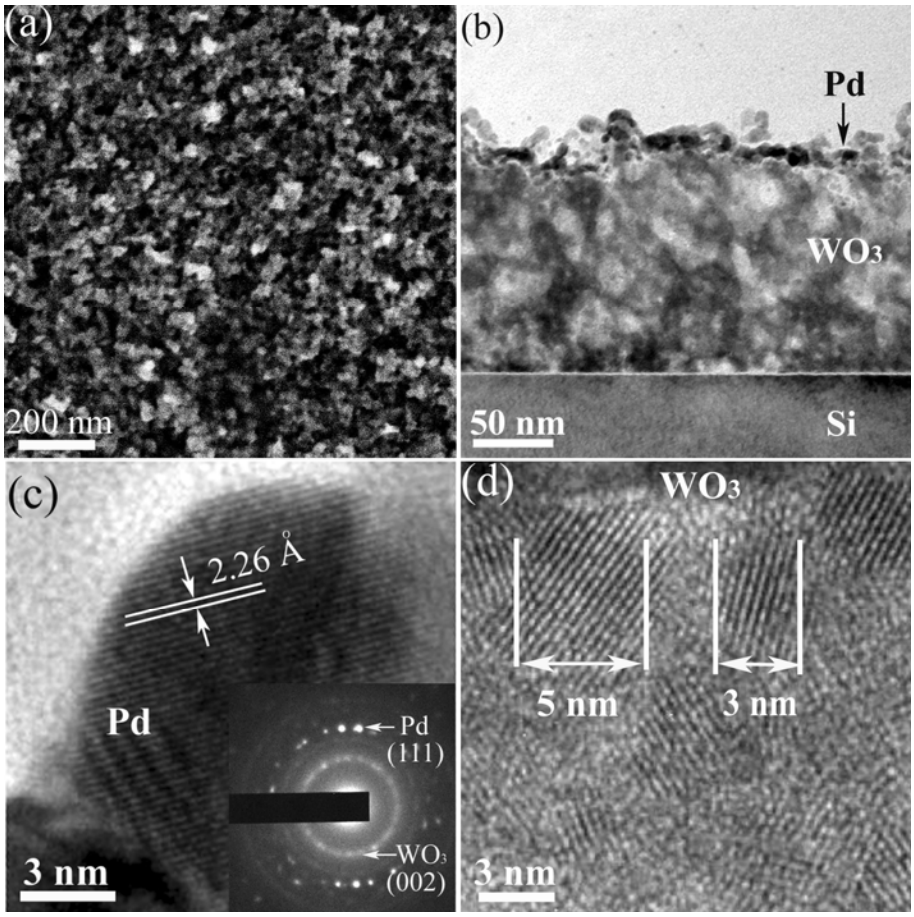

Figure 5.2 (a) SEM and (b–d) TEM images of a Pd/SCBD WO_3 film. Inset in (c) is a selected area electron diffraction pattern.

We also attempted to observe the cluster size with XRD experiment. The spectrum does not show any observable diffraction peak (Figure 5.3). This suggests that the crystallite size is too small to generate observable diffraction peak.

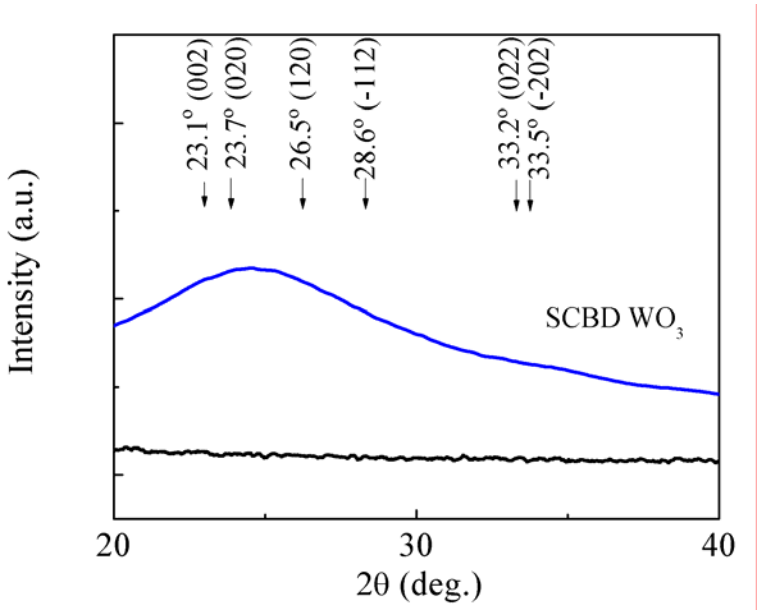

Figure 5.3 XRD pattern of a Pd/SCBD WO_3 film.

The next is to investigate the porosity of the SCBD WO_3 film structure. Two methods were employed. The first one starts from measuring the mass-equivalent thickness of an as-deposited tungsten metal film with a quartz monitor, which was found to be t_W = 14.1 nm. The density of tungsten (D_W = 19300 kg m^{-3}) was used in the calculation. If it is oxidized to a form a dense structure with a density equal to that of crystalline WO_3, D_{WO_3} = 7160 kg m^{-3}, knowing the atomic weight of tungsten, Z_W = 183.85, and molecular weight of WO_3, Z_{WO_3} = 231.85, the mass equivalent-

thickness of the WO_3 film is calculated to be $t_{WO_3} = (t_W \times Z_{WO_3} \times D_W)/(Z_W \times D_{WO_3}) = 48$ nm. On the other hand, the actual film thickness was measured from the TEM image and determined to be $t_{WO_3\text{-TEM}}$ =140 nm. It is highly consistent with that observed with a surface profiler, namely 143 nm. Comparing the mass-equivalent film thickness and real film thickness of an SCBD WO_3 layer, its porosity is estimated to be $(t_{WO_3\text{-TEM}} - t_{WO_3})/t_{WO_3\text{-TEM}} = 66\%$.

The second method relies on the measurement of the refractive index of the SCBD WO_3 film n_f. It was found to be 1.7 by using the prism coupling technique. By putting it into the Clausius-Mosotti equation (Chapter 3), the porosity of the film is calculated to be 39%. This value is underestimated due to densification caused by the use of a compressive stress of 50 psi for holding the sample during measurement, so that the film is severely densified. We thereby suggested that the porosity of an SCBD WO_3 film is 66%, or more conservatively, not less than 39%.

The Raman spectrum of the film (Figure 5.4) provides more structural information on the WO_3 nanoclusters. The spectrum contains a component at 957 cm^{-1}, which is attributed to the stretching mode of W^{6+}=O terminal bonds located around the cluster surfaces [125-127]. The spectrum also contains a component at 791 cm^{-1}, which is a mergence of two components originating from the stretching modes of W^{6+}-O bonds like that in crystalline WO_3 [128, 129]. The ratio of the intensity of the first component to that of the second one is inversely proportional to

the average size of the WO_3 nanoclusters [126]. For our SCBD WO_3 film, this ratio is 0.54 and is larger than most published values of other nano WO_3 materials [126, 128-132].

Combining the above results, the structure of the Pd/SCBD WO_3 film should have the following features.

(i) The WO_3 clusters are genuine "nanoclusters" having a dimension of a few nanometers.

(ii) A nanocluster has a disordered structure with tiny crystallites embedded inside.

(iii) The nanoclusters are loosely connected with disordered inter-cluster regions containing mainly W^{6+}=O terminal bonds.

(iv) Porosity of the WO_3 film is as high as 66%.

(v) The surface roughness z_{rms} is as high as 12 nm due to the random packing of the nanoclusters (as seen in the AFM image shown in Figure 5.5).

(vi) The Pd coating on the WO_3 surface is ragged and cannot give a good coverage on this surface as seen in the TEM image Figure 5.2 (b).

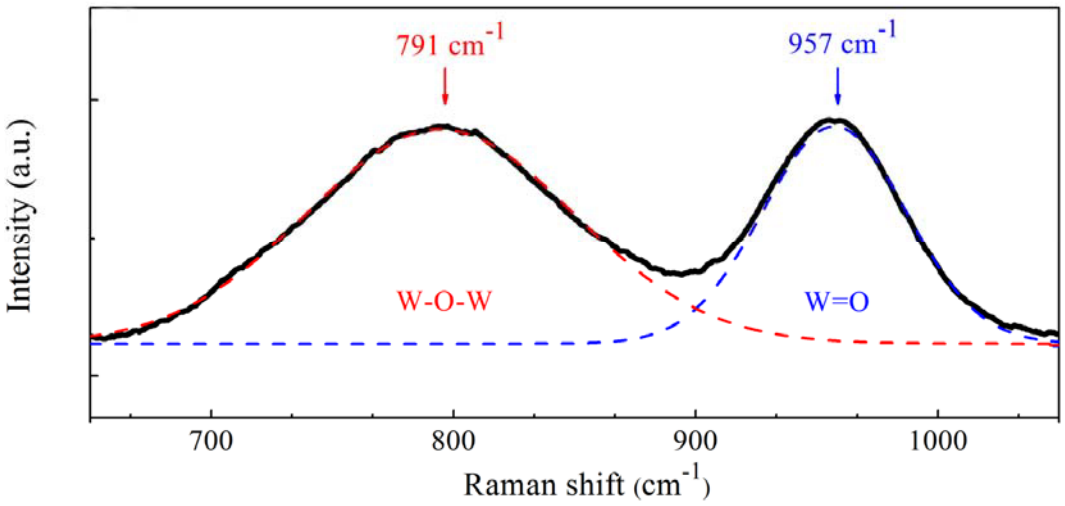

Figure 5.4 Micro-Raman spectrum of a Pd/SCBD WO_3

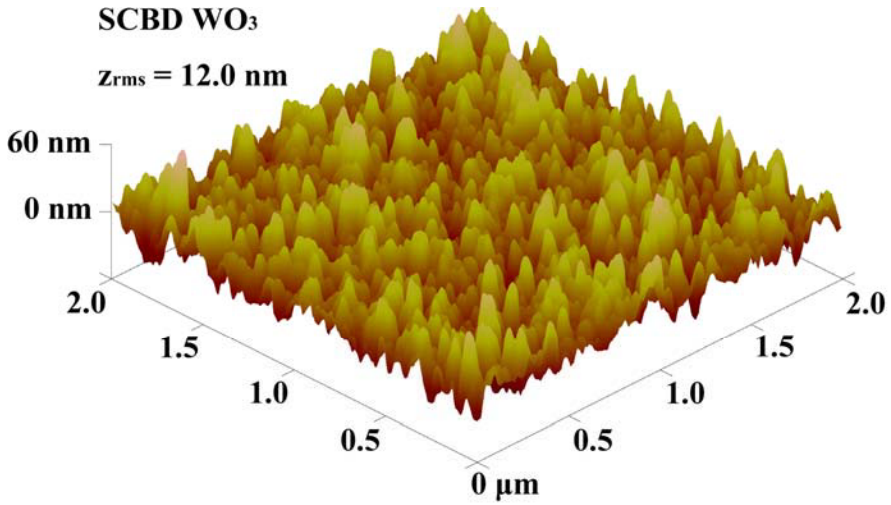

Figure 5.5 AFM image of an SCBD WO_3 film

5.2 H_2 sensing performance

5.2.1 Optimization of operation temperature

In a primary test of the H_2 sensing response of a Pd/SCBD WO_3 film performed at $T_{operate}$ = 20°C, the loading time was set to be 60 min. The time dependence of the film resistance R_{H_2} with increasing H_2 concentration from 4 to 3000 ppm was plotted in Figures 5.6 (a–b). At this temperature, the response rate is slow. R_{H_2} cannot reach equilibrium in this period. However, when $T_{operate}$ was slightly increased to 80°C, the response rate was much faster and R_{H_2} was stabilized in a much shorter period of 5 min. Measurements were carried out again at 80°C with loading time of 5 min, Results obtained are plotted in Figures 5.6 (c–d).

We define the sensor response as $S = (R_{H_2} - R_o)/ R_{H_2}$ with R_o and R_{H_2} being the film resistance measured in a H_2-free environment and at the end of the loading period respectively. The data of film resistance show in Figures 5.6 (a–d) were used to derive the sensor responses for the two temperatures, denoted as S_{20} and S_{80}, Results are plotted in Figure 5.7 (a) as functions of H_2 concentration. Although S_{80} is apparently larger than S_{20}, one notices that the response rate of the film resistance at 20°C is low, so that R_{H_2} measured at the end of the loading period may have not reached the equilibrium value, and hence the value of S_{20} thus derived could be severely underestimated.

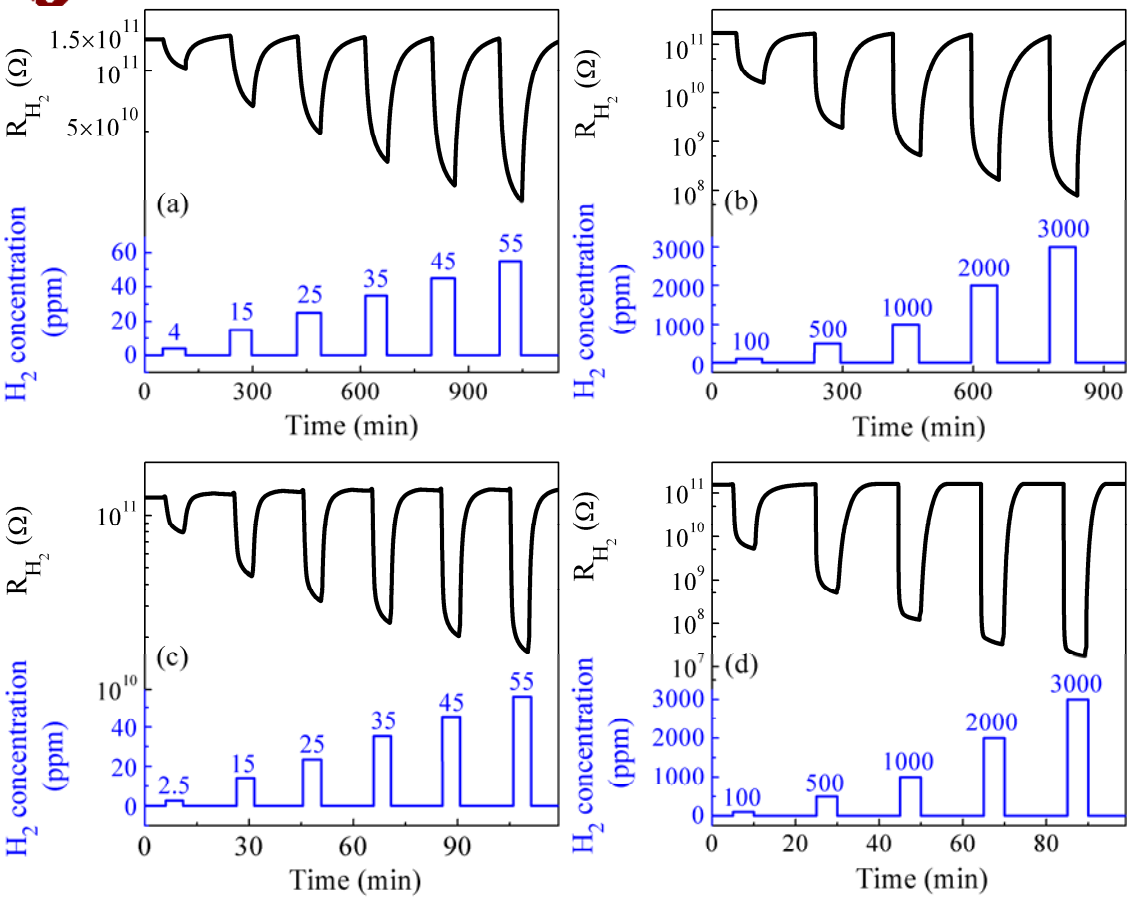

Figure 5.6 (a–d) Resistive response of a Pd/SCBD WO_3 film with increasing H_2 concentration measured at $T_{operate}$ = 20 and 80°C, respectively.

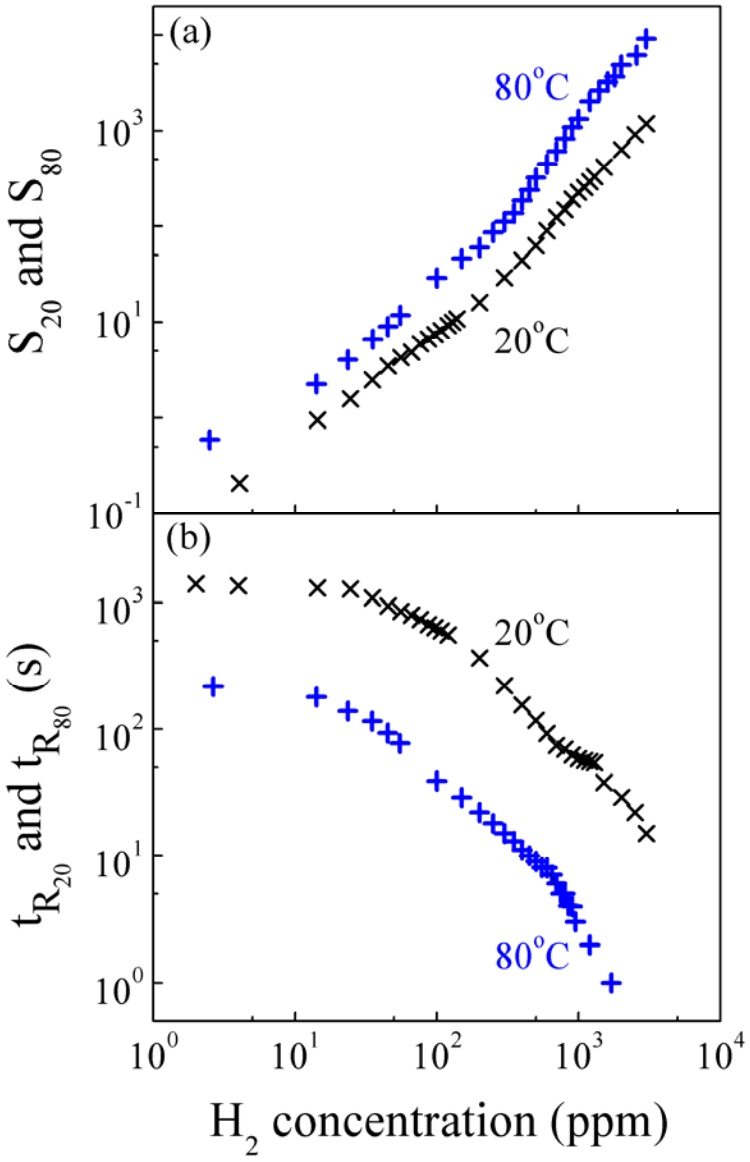

Figure 5.7 (a–b) Plots of S_{20}, S_{80}, $t_{R_{20}}$ and $t_{R_{80}}$ of a Pd/SCBD WO_3 film versus H_2 concentration.

This conjecture was primarily supported by the data shown in Figure 5.7 (b), which indicates that the response time measured at 20°C, $t_{R_{20}}$, is much longer than that of 80°C, $t_{R_{80}}$ (< 1 s), consistent with the viewpoint that at 20°C a period of time should be waited for the film resistance to reach equilibrium. In other words, if longer duration is waited for R_{H_2} to be stabilized, a larger S_{20} can be observed. A more direct evidence is from the observations of the change of film resistance with time in prolonged hydrogenation processes (exceeding 2 hrs) performed at three $T_{operate}$ = 20, 80 and 140°C, respectively. A H_2 concentration of 20000 ppm in air was used in these tests. Results are shown in Figure 5.8. The film samples used for the tests were deposited on substrates having inter-digital electrodes (IDE) in order to lower their base resistances. The structure and fabrication process of IDE are described in Section 2.2.2. In these tests, R_{H_2} has enough time to reach equilibrium, Results show that the sensor response dropped from $S_{20} = 1.8\times10^5$ to $S_{80} = 1.6\times10^5$, and finally to $S_{140} = 2.3\times10^4$ when $T_{operate}$ increases successively from 20 to 80 and then to 140°C. This trend contradicts to the apparent one as presented in Figure 5.7 (a), and is more likely to reflect the true result. Therefore, we believe that S_{80} and $t_{R_{80}}$ should be the real sensor response and response time of the film at 80°C. They are mainly used for discussion in this thesis. Results obtained from the tests at $T_{operate}$ = 20°C are just for reference use only.

Figure 5.8 also illustrates that both R_o and R_{H_2} drop with increasing $T_{operate}$. This

is because more free charge carriers are generated to make the oxide more conductive; causing reduction of the populations of surface sorbed oxygen species (mainly O_2 molecules and O_2^- ions below 150°C [38-40]), and subsequent thinning of depletion layer on the oxide surface. It happens that the difference between the two resistance values decreases with increasing $T_{operate}$, so that the sensor response depending on the fractional change of the resistance is lowered. Furthermore, the drop of $t_{respond}$ with increasing $T_{operate}$ is attributed to the faster dissociation rate, diffusion rate and reaction rate of the reactant gas molecules, and larger mobility of charge carriers in the oxide at a higher temperature environment.

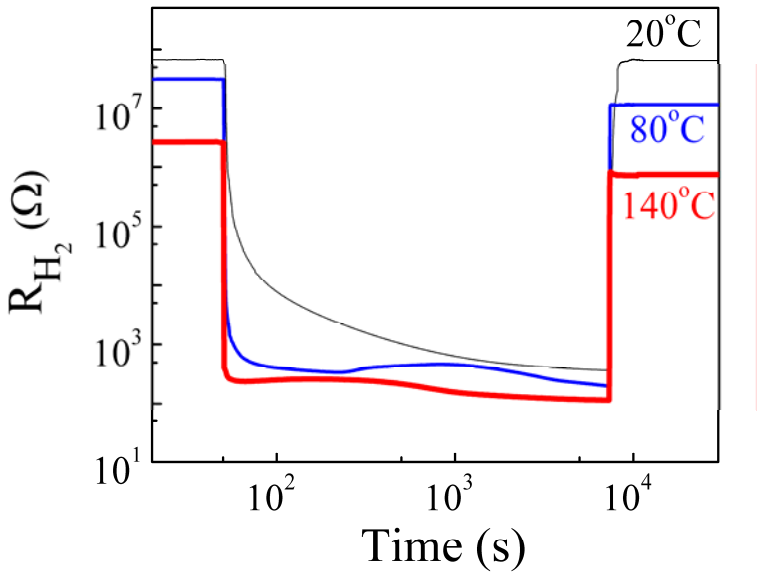

Figure 5.8 R_{H_2} of a Pd/SCBD WO_3 film versus time of measurement observed at 20, 80 and 140°C respectively. A H_2 concentration of 20000 ppm in air was used for hydrogenation.

5.2.2 Sensor response and response time

Based on the above discussion, the data of S_{80} and $t_{R_{80}}$ shown in Figures 5.7 (a–b) are regarded to be the real sensor response and response time of a Pd/SCBD WO_3 at 80°C. They are used in the discussion and comparison presented in the following.

Results of S_{80} are further used to derive the lowest detection limit of H_2 concentration of a Pd/SCBD WO_3 at 80°C. This limit is derived semi-theoretically, and could be smaller than the lowest available setting of H_2 concentration used in the measurements. Figure 5.9 shows that S_{80} depends almost linearly on H_2 concentration below 55 ppm, and can be described by a linear fit of S = 0.2× H_2 concentration. The estimated lowest detectable limit of H_2 concentration is assumed to be equal to the H_2 concentration leading to an S_{80} close to three times of the noise level, i.e. S_{noise} [133, 134]. S_{noise} was determined experimentally as $R_{niose}/\langle R_o \rangle$, where R_{niose} was the standard deviation of 600 data points of R_o measured in an H_2-free environment, and $\langle R_o \rangle$ was the mean. Results show that S_{noise} at 80°C was 0.002. From the slope of the plot in Figure 5.9, the lowest detectable limit of H_2 concentration at 80°C was $3S_{noise}/0.2$ = 0.03 ppm, which is lower than those of most nano-MO_x based H_2 sensor prototypes reported in literatures.

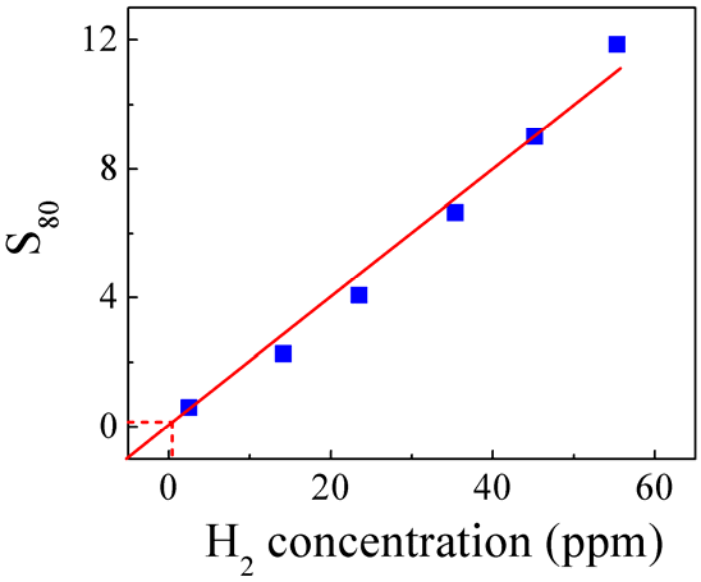

Figure 5.9 A plot of S_{80} of a Pd/SCBD WO_3 film against H_2 concentration in the range of 2.5–55 ppm. The red line is a linear fit to the data point.

Now, let us compare S_{80} and $t_{R_{80}}$ of a Pd/SCBD WO_3 film with the reported values of other nano H_2 sensors operating at room temperature [16, 65, 96-103] as shown in Figures 5.6 (a–b) and Table 5.1. Most of the nano-MO_x based H_2 sensors reported in literature can be classified into two groups, namely,

(i) The first group includes those containing small nanoclusters embedded in a rather dense matrix [65, 96, 101-103].

(ii) The second group includes those made of loosely packed one-dimensional (1-D) elements [16, 97-100], like wires, fibres, and belts. Note that the thicknesses of these 1-D elements, denoted as the characteristic lengths L of their geometries, are actually rather thick and fall in the range of 30~300 nm.

The data of these two groups of sensors are presented by solid and hollow symbols in the Figures 5.10 (a–b). One sees that S_{80} of our Pd/SCBD WO_3 film in the H_2 concentration range employed in the measurements is much higher than those of Group 2 sensors composed of thick 1-D elements [16, 97-100]. In addition, $t_{R_{80}}$ of the Pd/SCBD WO_3 film is much shorter than those of Group 1 sensors having dense matrixes containing nanoclusters [65, 96, 101-103]. Only one sensor composed of loosely packed ZnO nanorods [16] can be able to respond a bit faster than the Pd/SCBD WO_3 film.

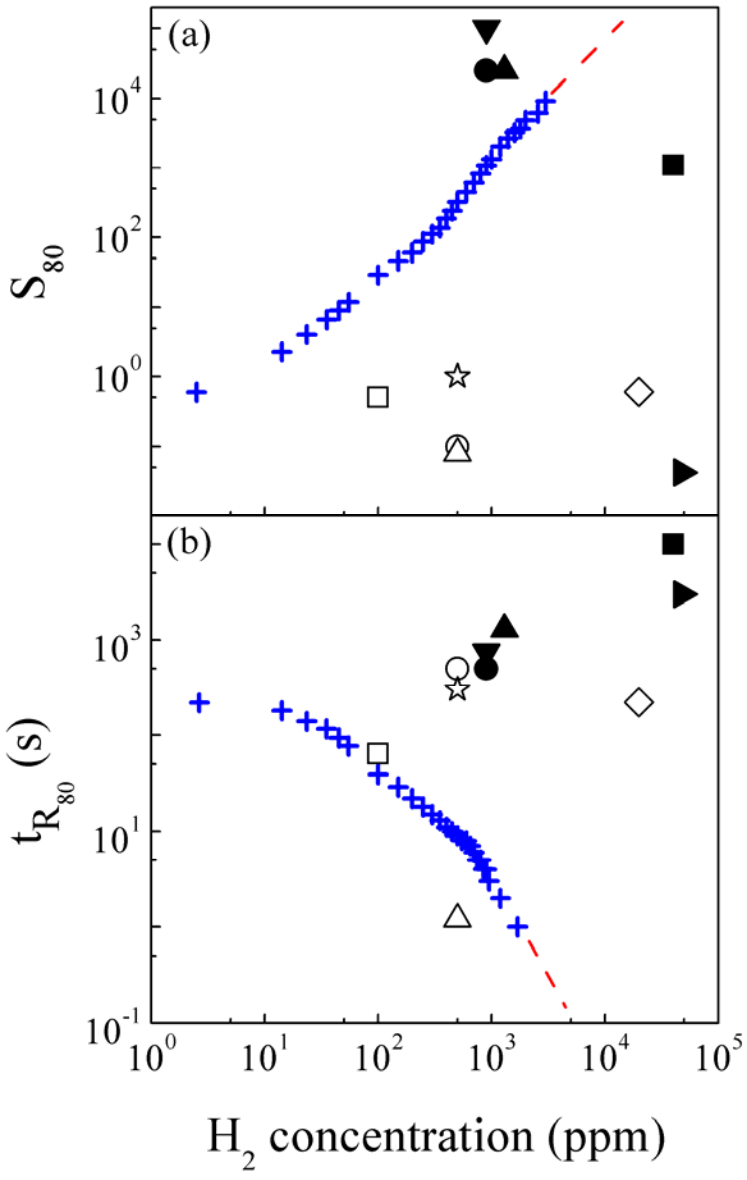

Figure 5.10 (a–b) Comparison of S_{80} and t_{R80} of a Pd/SCBD WO_3 film with those of other reported nano-MO_x H_2 sensors at room temperature. Solid and hollow symbols are data of nano-MO_x H_2 sensors made of nanoclusters and 1-D sensing materials respectively.

× Pd/SCBD WO_3 ▶ Pt/WO_3 [96] ▲ Pd-WO_3 [101] ■ Pt/$InSnO_2$ [102]
● Pt/$InSnO_2$ [103] ▼ Pt/$InSnO_2$ [65] ○ Pt/ZnO [97] △ ZnO [16]
□ ZnO [98] ◇ SnO_2 [99] ☆ TiO_2 [100]

Table 5.1 Summary of nano-MO_x H_2 sensor operating at different $T_{operate}$.

Geometry	**Material**	**L (nm)**	$T_{operate}$ (^oC)	**S**	**Measurement condition**	$t_{respond}$ (s)	**Ref.**
nanoclusters	Pd/SCBD WO_3	3–5	80	1.9×10^5	20000 ppm in air	< 1	
nanoclusters	Pt/WO_3	35–65	20	0.89	pure H_2	3000	[96]
	Pd-WO_3	20		2.5×10^4	1300 ppm in air	1300	[101]
	Pt/$InSnO_2$	6–7		1.1×10^3	40000 ppm in air	10000	[102]
	Pt/$InSnO_2$	3		2.0×10^5	900 ppm in N_2	500	[103]
	Pt/$InSnO_2$	—		1.0×10^5	900 ppm in N_2	750	[65]
nanorods	Pt/ZnO	50–150		0.10	500 ppm H_2 in N_2	500	[97]
nanorods	ZnO	30–150		0.08	500 ppm H_2	1–2	[16]
nanowires	ZnO	100		0.52	100 ppm H_2 in air	64	[98]
nanobelts	SnO_2	80		0.65	20000 H_2 in N_2	220	[99]
nanofibers	TiO_2	300		1	500 ppm H_2	300	[100]
nanoclusters	Pt/TiO_2	~ 20	500	90	500 ppm in N_2	5–10	[135]
	SnO_2	4	350	140	1000 ppm in air	0.15	[120]
	SnO_2-SWCNT	15	250	1.5	1500 ppm	2–3	[136]
	Au/WO_3	—	262	370	10000 ppm in air	30–60	[137]
	Pt-WO_3-TiO_2	55	200	20	1000 ppm in air	60	[138]
	Pd/WO_3	33	300	391	2300 ppm	102	[139]
	Pt-WO_3/ZrO_2	0.5–0.9	300	48	16000 ppm in air	10–20	[140]
	WO_3-MWCNT	42.3	300	1.2	12000 ppm in air	3	[141]
	Ag-TiO_2	22	360	3.6	200 ppm in air	23	[142]
nanobelt	Pd/SnO_2	50–80	200	3.4	13ppm in vacuum	120	[143]
nanotubes	$MgZnFe_2O_4$	20–25	350	10	1660 ppm in air	60	[144]

We further compare S_{80} and $t_{R_{80}}$ of a Pd/SCBD WO_3 film with those of other reported nano H_2 sensors operating at elevated temperature $T_{operate} \geq 200^oC$ [120, 135-144]. Data are plotted in Figures 5.11 (a–b), and are tabulated in Table 5.1. One sees that even operating at a lower $T_{operate}$, S_{80} of a Pd/SCBD WO_3 film is considerably larger than those of others in the range of H_2 concentration concerned. In addition, $t_{R_{80}}$ of the Pd/SCBD WO_3 film is mostly shorter or comparable to those of others operating at much higher $T_{operate}$.

Combining the insights gained from the above comparison, we assert that high sensor response and fast response rate of the SCBD WO_3 film are mainly due to the genuine nanocluster size and extremely high porosity of the film structure.

We further note that manufacturers of H_2 fuel cell driven vehicles are asking for advanced H_2 sensors having a $t_{respond} < 1$ s [6]. However, most existing H_2 sensor products fail to meet this requirement. The only H_2 sensor capable of giving $t_{respond}$ in the order of 1s known so far is that made of MO_x materials [120], but the sensor needs to work at a rather higher $T_{operate}$ (250~350^{o}C) and hence is readily interfered by other co-existing flammable reducing gases [5, 6, 120]. Results show that $t_{R_{80}}$ of our Pd/SCBD WO_3 film can be reduced from 218 to 3 s when H_2 concentration in air increases from 2.5 and 1000 ppm. It further drops to below the shortest acquisition time of the measurement system, i.e. 1s, when H_2 concentration exceeds 1700 ppm. Therefore, a Pd/SCBD WO_3 film can satisfy the requirement for the said application.

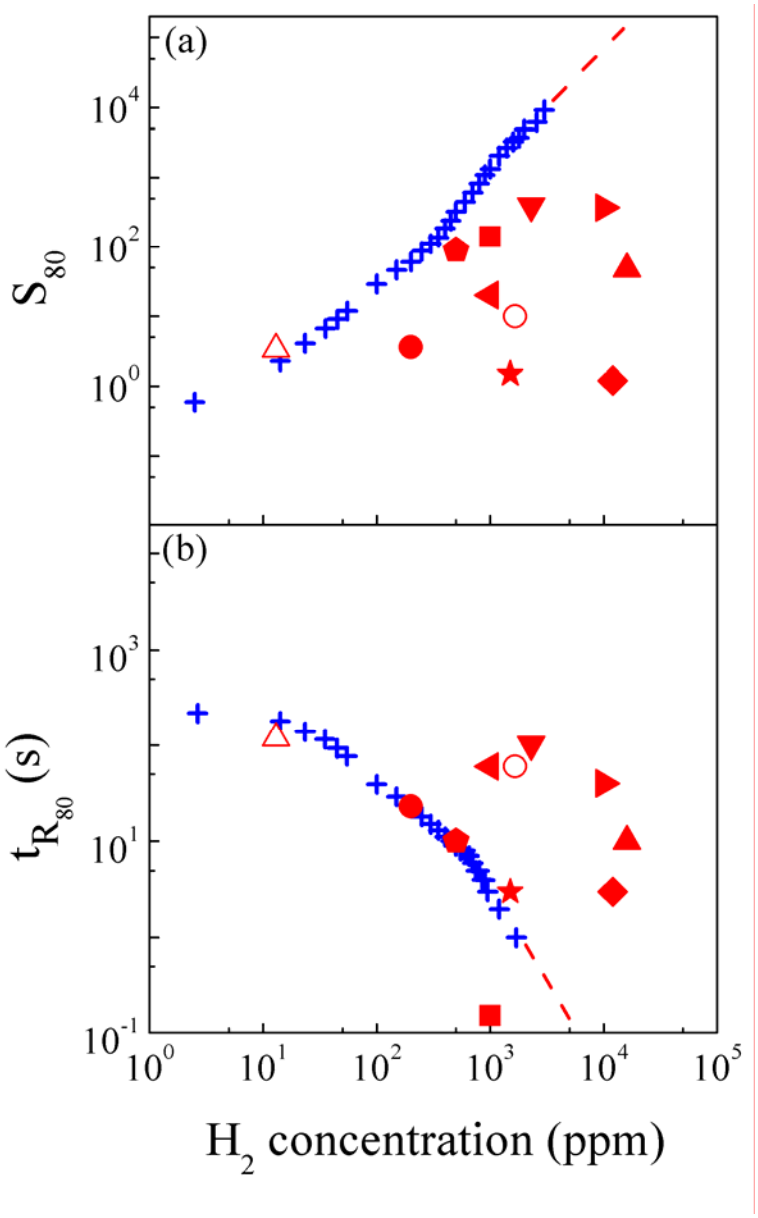

Figure 5.11 (a–b) Comparison of S_{80} and t_{R80} of a Pd/SCBD WO_3 film with those of other reported nano-MO_x H_2 sensors operating at $T_{operate} \geq 200^oC$. Solid and hollow symbols are data of nano-MO_x H_2 sensors made of nanoclusters and 1-D sensing materials respectively.

⬟ Pt/TiO_2 [135] ■ SnO_2 [120] ★ SnO_2-CNT [136] ▶ Au/WO_3 [137]
◀ Pt-WO_3-TiO_2 [138] ▼ Pd/WO_3 [139] ▲ Pt-WO_3/ZrO_2 [140] ◆ WO_3 [141]
● Ag-TiO_2 [142] △ Pd/SnO_2 [143] ○ $MgZnFe_2O_4$ [144]

5.2.3 Cyclic stability

Instability of the output of a chemical sensor is constantly a critical problem affecting the performance of the device [47, 145-147]. It can be caused by many reasons. Particularly for those required to operate at elevated $T_{operate}$, oxygen vacancies tend to be relocated, or the concentration of vacancies or elemental composition is altered, or the size of the grains grows due to annealing. Instability of the performance of a gas sensor is manifested by the drift of the output—in this case the base resistance R_o and/or hydrogenated resistance R_{H_2}—even when the concentration of the target gas is fixed. The response of the sensor is thereby unstable. Different from S and $t_{respond}$, studies on stability of gas sensors are much more seldom reported [78, 103, 148, 149], because durability tests are very time consuming and there is no measurement standard to follow. Therefore, we designed an experiment to investigate the stability of the H_2 sensing response of our Pd/SCBD WO_3 films. In the tests, the film was repeatedly exposed to 20000 ppm H_2-air mixture for 1 min and synthetic air for 14 min over a large number of cycles. Also, the film was shunted with a 20-GΩ resistor in order to cap the maximum film resistance.

Figure 5.12 shows the resistive responses of selected switching cycles observed at different stages of the cyclic tests performed at $T_{operate}$ = 20 (for reference mainly)

and 80^{o}C respectively. Result shows that for both of the two measurement temperatures, the resistive response is highly repeatable over 2400 switching cycles. One notices that the resistance change observed at 20^{o}C is much smaller than that observed at 80^{o}C, because for the test at 20^{o}C the film resistance has not reached equilibrium in the loading period. The excellent cyclic durability of the film sensor is attributed to the use of moderate $T_{operate}$ in the tests, where post-annealing effect usually encountered by an MO_x-based sensor operating at high $T_{operate}$ does not occur. In particular, at 80^{o}C the overall resistance dropped from 20 GΩ to 4.75 MΩ within 1 min during hydrogenation. This amplitude of drop does not deviate from the initial one by more than ±5% after 2400 switching cycles.

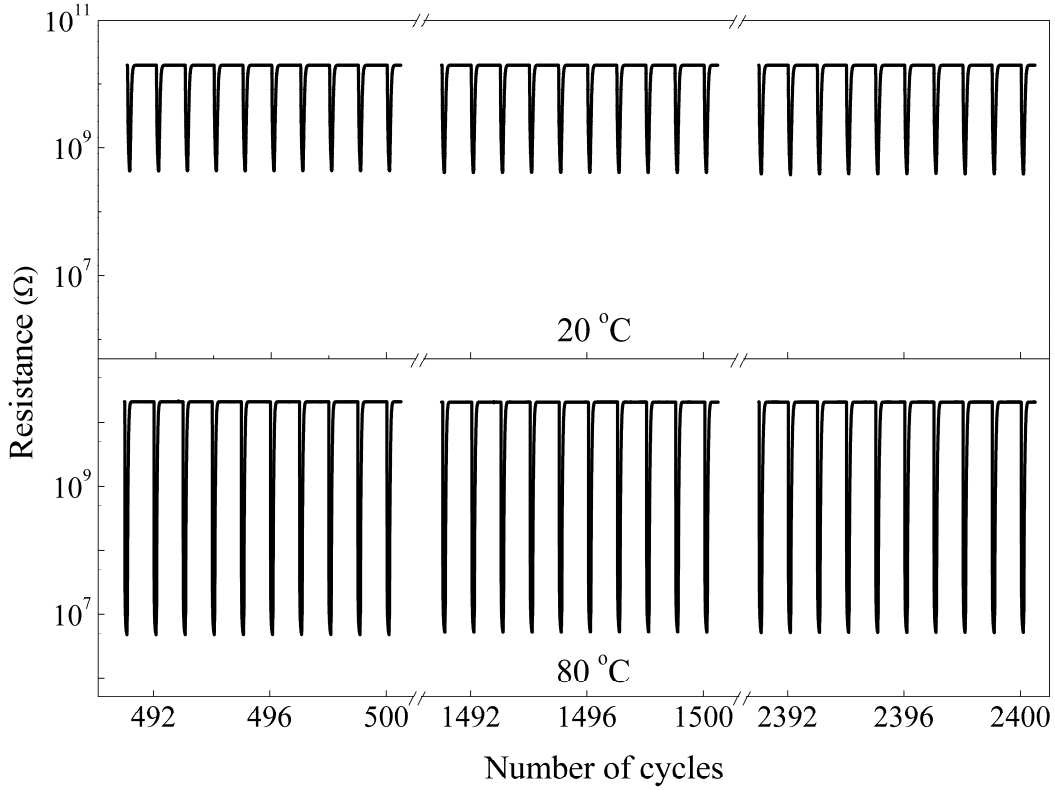

Figure 5.12 Resistive response of the sample observed in cyclic tests performed at 20 and 80°C. A H_2 concentration of 20000 ppm in air was used for hydrogenation.

5.2.4 Selectivity

Figure 5.13 shows the resistive response of a Pd/SCBD WO_3 at 20 and 80°C to various organic compound (VOC) vapours at a concentration of 100000 ppm (=10%) in air, including methanol, ethanol, isopropanol (IPA), formaldehyde (FD) and acetone. The change of resistance is negligibly small compared with that associated with 20000 ppm H_2 in air at both 20 and 80°C. Conservatively speaking, the interference caused by these VOCs would not be more than 1.1×10^{-5} of the signal due to H_2. This result is directly related to the moderate-operation-temperature condition, where no combustion of the VOCs can happen to affect the output, and the Pd layer mainly dissociates H_2 molecules to assist hydrogenation of the oxide layer, but not effect on the VOC vapors.

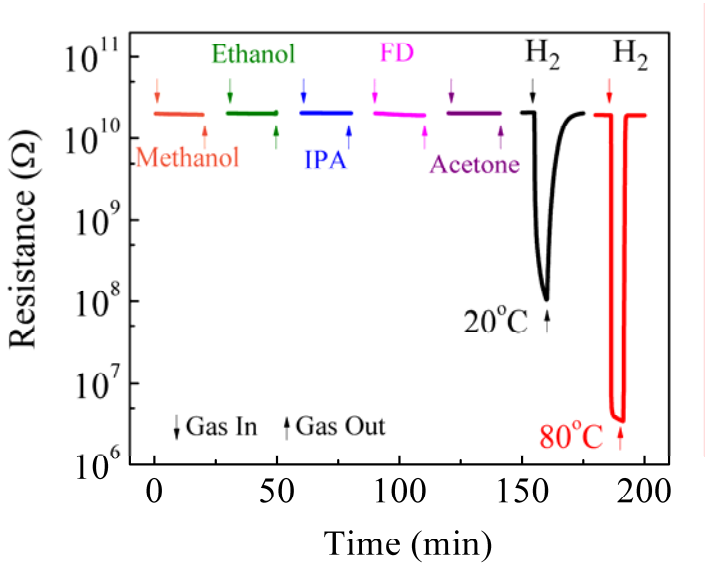

Figure 5.13 Selectivity of the sample at 20 and 80°C against vapours of several VOCs at a concentration of 100000 ppm in air, including methanol, ethanol, iso-propanol (IPA), formaldehyde (FD), acetone. Both the resistive responses to 20000 ppm H_2 in air at 20 and 80°C are shown.

5.2.5 Dependence on relative humidity

Figures 5.14 (a–b) show the influence of relative humidity (RH) on the resistive response of a Pd/SCBD WO_3 film at $T_{operate}$ = 20 (for reference mainly) and 80^{o}C, respectively, with the hydrogenation processes performed at 20000 ppm H_2 in air. All the gases were from bottles and assumed to be dry with an RH of 0%. The gas can be guided to pass through a water-containing chamber. As such the RH of the gas can be set to reach 90%. The film was shunted with a 20-GΩ resistor to lower the resistance of the film for easing the measurements.

For the case of $T_{operate}$ = 20^{o}C, the resistance of the sample in humid air was 10 times lower than that in dry air. This is because moisture was present on the film surface can lower the sample's resistance. Evacuation of the measurement chamber also removed the moisture inside, such that the measured resistance returned to 20 G promptly. When humid H_2-air admixture was admitted, the sample's resistance first drops rapidly due to the influence of moisture; and then further drops due to hydrogenation of WO_3 layer. However, the measured resistance was higher than that measured in dry H_2-air gas. This is because when water molecules are adsorbed on the film surface, H_2 molecules would be blocked to reach the WO_3 layer to cause further drop of the resistance. Therefore, a Pd/SCBD WO_3 film is hardly used for determining H_2 concentration in a humid environment.

At $T_{operate}$ = 80^{o}C, the variations of the film resistance in the loading processes

performed at RH = 0 and 90% were found to show very similar sensor response and short $t_{respond}$ (< 1s). We explain this finding by assuming that the moderate $T_{operate}$ of 80°C is able to remove most physisorbed water molecules from the sensor's surface, but this $T_{operate}$ is not high enough to initiate chemisorption of water molecules which may cause the resistance of a MO_x to drop substantially [38]. It is also noticed that the recovery time of the resistance in the hydrogenation process is shortened markedly from 226 to 60 s with RH increased from 0 to 90%. The effect is explained by the phenomenon observed by other research groups [148, 150, 151], who claimed that the presence of moisture in the detected area can be adsorbed on the surface of WO_3 to form a "water bridge", which facilitates hydrogen species to hop through and hence their mobility on the oxide surface is prominently enhanced [150, 151].

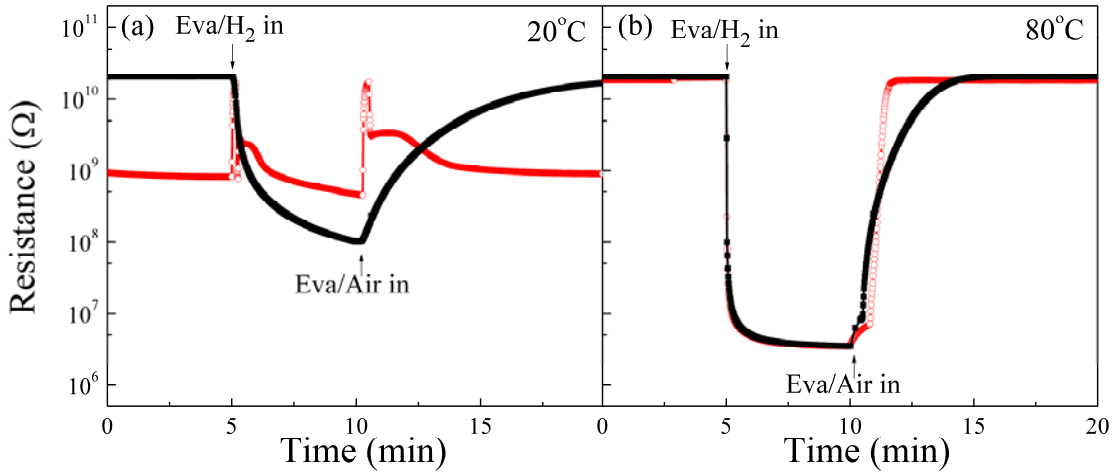

Figure 5.14 (a-b) Resistive response of the sample in dry (RH = 0%) and humid (RH = 90%) environment measured at 20 and 80°C, respectively.

5.2.6 Pressure dependence

One possible application of H_2 sensors is for detecting leakage of H_2 from a fuel cell driven vehicle. Such a vehicle is generally required to be able to travel across a height at least 4000 m from the sea level. As such, a H_2 sensor installed inside the vehicle must be less sensitive to the corresponding span of ambient pressure, namely, ranging from one atmospheric pressure to 62 kPa [6]. Most existing H_2 sensors do not meet this requirement [6]. For research type nano-MO_x based H_2 sensors, Shukla et. al. reported a typical example indicating that the sensor response of nanocrystalline $InSnO_2$ measured at 101 kPa is double of that measured at 26 kPa [152].

Referring to this background, we performed an experiment to investigate how S_{20} and S_{80} of a Pd/SCBD WO_3 film depend on ambient pressure over a range of 30.7 to 101.2 kPa for simulating the change of condition that the sensor would encounter if it is used over a vertical range from sea level to an elevation of 9000 m. H_2 concentration of 20000 ppm in air was used in hydrogenation process. Each hydrogenation process was set to last for 5 min. A 20 GΩ resistor was shunted to the film sample to facilitate resistance measurements.

Figure 5.15 shows how the resistance of the film measured at 20 and 80^{o}C depends on ambient pressure. For both values of $T_{operate}$, the variation of the amplitude of resistive change is mild and below 9%. In particular, the resistive

response measured at 20°C has not been stabilized in the loading process. This condition allows the sensor to be used to alert H leakage if accurate determination of H_2 concentration is not necessary.

We further suggest that due to the highly porous structure, both hydrogen and oxygen molecules can diffuse in the film agilely with similar rates, such that a pressure change in the environment would not cause significant variation in their molar ratio everywhere inside. This helps to diminish the ambient pressure dependence of the response. If this inference is correct, the ambient pressure dependence of a more porous nano-MO_x based H_2 sensor would be less significant.

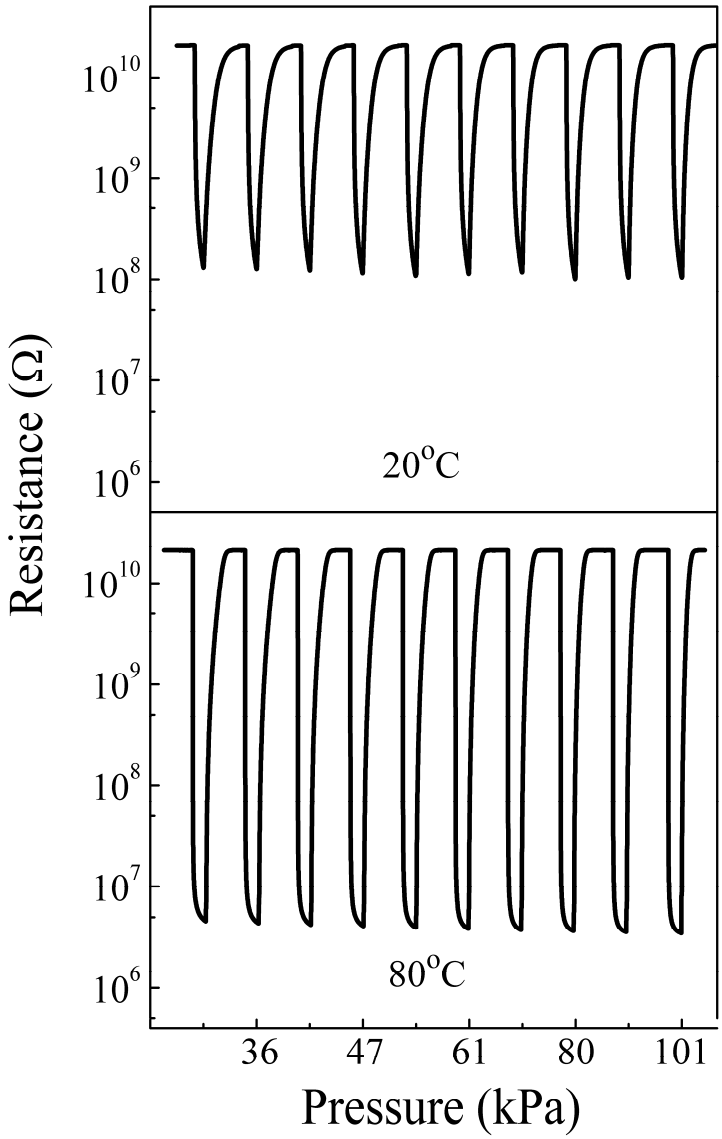

Figure 5.15 Ambient air pressure dependence of resistive response of the sample measured at 20 and 80°C, respectively.

5.3 Comparison with commercialized H_2 sensors

A comparison of the H_2 sensing properties of the Pd/SCBD WO_3 film sensor measured at 80°C with those of the commercialized H_2 sensors is highlighted in the

following, with data tabulated in Table 5.2.

(i) The measured lower detection limit LDL of the Pd/SCBD WO_3 film sensor is 2 ppm. The theoretical limit is even lower at 0.03 ppm. They are much lower than those of the commercialized sensors. The measured upper detection limit UDL of the Pd/SCBD WO_3 film sensor is about 2%, which is larger than those of commercialized MO_x-type H_2 sensors. The actual value could be larger but not measured due to safety consideration.

(ii) The normalized sensor response NS of the Pd/SCBD WO_3 film sensor is about 50 times larger than those of commercialized MO_x-type sensors, and is about one million times larger than that of the thermal conduction- (TC-) type and Pd-based resistivity-type sensors.

(iii) The response time of the Pd/SCBD WO_3 film sensor is less than 1 s, which is much shorter than those of the commercialized sensors. Therefore, the Pd/SCBD WO_3 film sensor can be used in hydrogen driven vehicles and spacecrafts where the requirements for the H_2 sensors are most stringent among all related applications.

(iv) The Pd/SCBD WO_3 film sensor performed as well as it was just fabricated three years ago from now. This allows us to assert that the static lifetime is longer than three years. Furthermore, its performance does not show any degradation

after 2400 testing cycles. We further claim that the durability of the sensor is better than that of most other H_2 sensors.

(v) The selectivity of the Pd/SCBD WO_3 film sensor is much better than the commercialized MO_x-type, electrochemical- (EC-) type and catalytic combustion- (CC-) type H_2 sensors. It also showed better resistance against the variations of relative humidity and ambient pressure compared with the commercialized H_2 sensors.

(vi) The operate temperature $T_{operate}$ and hence the power consumption of the Pd/SCBD WO_3 film sensor is much lower than those of the commercialized sensors except for the electrochemical (EC) type ones.

At last, the SCBD and sputtering technique are compatible to Si-based micromachining techniques. Therefore, the sensor is readily miniaturized and can be fabricated with high batch-to-batch reproducibility with low production cost. We have demonstrated the feasibility of fabricating sensor with a size of 2.5×2.5×0.5 mm^3 on interdigited electrode (IDE), which is much smaller than the commercialized H_2 sensors. With this size, more than 1000 sensor can be fabricated on a 4-inch Si wafer. The material cost for making one such a sensor is about 0.1 USD (much lower than the quoted prices of the commercialized products).

Table 5.2 Performance indexes of major existing types of H_2 sensor products and the Pd/SCBD WO_3 sensor.

	MO_x-type sensor	**EC-type sensor**	**CC-type sensor**	**TC-type sensor**	**Pd resistivity type sensor**	**Pd/SCBD WO_3 Sensor**
LDL	50 ppm	100 ppm	> 100 ppm	1000 ppm	5000 ppm	< 2 ppm
UDL	≤ 2 %	≤ 4 %	≈ 4 %	≤ 100 %	≤ 100 %	> 2%
NS (ppm^{-1})	0.15/ppm at 2% H_2 [51]	0.002/ppm at 1.15% H_2 [55]	5.3×10^{-4}/ppm at 1% H_2 [57]	2.5×10^{-6}/ppm at 10% He [60]	7.6×10^{-7}/ppm at 2% H_2 [35]	8/ppm at 2%H_2
$t_{respond}$	5–20 s	30–60 s	10–30 s	10–50 s	< 60 s	<1
Static lifetime Cyclic lifetime	5 years no data	2 years no data	3–5 years no data	5 years no data	5–10 years no data	> 3 years >2400 circles
Selectivity	affected by reducing gases	affected by reducing gas_{es}	affected by combustible gases	good	good	good
Atmospheric pressure dependence	strong (80–20 kPa)	mild (90–110 kPa)	weak (80–120 kPa)	weak (70–130 kPa)	no data (80–100 kPa)	weak (30–100 kPa)
$T_{operate}$ $T_{environ}$ $T_{environ}$ dependence	400–500°C -20–80°C strong	-20–50°C ditto moderate	400–500°C -20–80°C weak	100–200°C 0–50°C strong	120°C -20–0°C strong	80°C no data
RH dependence (observed range)	strong (10–95%)	weak (15–90%)	nil (0–95%)	weak (0–95%)	nil (0–95%)	nil (0–95%)
Batch-to-batch reproducibility	poor	poor	good	good	good	good
Miniaturizability	difficult	difficult	difficult	difficult	yes	yes
Power consumption	> 500 mW	< 100 mW	> 500 mW			<100 mW
Unit price (USD)	300–500 USD	1200 USD	1700 USD	> 1000 USD	> 2000 USD	≈ 0.1 USD (material cost)

5.4 Conclusions

$T_{operate}$ dependence of the H_2 sensing properties of Pd/SCBD WO_3 films was investigated. At low $T_{operate}$, sensor response is larger, but the response time is too long for the resistive response to reach equilibrium within a reasonable loading period. Slightly rising $T_{operate}$ to 80°C, the sensor response only drops mildly, but the response is substantially reduced to be around 5 min. A Pd/SCBD WO_3 hydrogen sensor operating at 80°C shows more other advantages and is recognized to be very useful in practice.

Sensor response and response time measured at 80°C are compared with other reported nano-MO_x based H_2 sensors reported in literature. These sensors are either made of small nanoclusters embedded in dense matrixes, or are made of loosely packed 1-D nano-sized elements (e.g. nanowires, nanofibres and nanobelts). The former mostly has large sensor response, but the response time is longer due to prolonged diffusion process of gas molecules in the dense matrix. On the other hand, the latter has a faster response rate, but the sensor response is lower because the 1-D species are actually rather thick. A Pd/SCBD WO_3 film is constructed of genuine 3 to 5-nm nanoclusters and has a very high porosity around 66%, such that it can give both large sensor response and faster response rate simultaneously. Its overall performance is superior to most reported nano-MO_x based H_2 sensors operating at room or elevated temperatures ≥ 200°C.

A Pd/SCBD WO_3 film sensor operating at 80°C was also found to have high cyclic stability over more than 2400 cycles without any sign of degradation. It also showed strong interference resistance against vapours of a number of VOCs. Importantly, the sensor operating at 80°C eliminates most influence from moisture which severely affects the sensing properties of the sensor at 20°C. Moreover, the recovery rate is much faster at 80°C. Ambient pressure dependence of the sensing performance is mild. The film also has other advantages including miniaturizability; compatible with silicon-based micro fabrication techniques, scalability in mass production; high batch-to-batch reproducibility based on the basic features of the SCBD technique.

Chapter 6 Hydrogen sensors made of palladium-coated sputtered tungsten oxide films

This part of study is aimed at examining how Pd-coated WO_3 films prepared by using sputtering technique can be made to have satisfactory sensor response, response and recovery times in H_2 sensing. Sputtering technique is concerned because it is a broadly used thin film fabrication technique, and is flexible in tailoring the film structure and properties through adjusting substrate temperature and sputtering pressure for deposition.

In our study, the material structure is characterized in terms of the crystallite size; porosity, surface roughness and thickness of the sputtered WO_3 films; and the thickness and continuity of the Pd coatings. Their gas sensing properties are compared with those of the Pd/SCBD WO_3 films presented in Chapter 5.

The most important finding is that a Pd/sputtered WO_3 film prepared at a lower temperature and higher sputtering pressure tends to have a more disordered and porous structure. These features lead to a high sensor response, and shorter response and recovery times ($t_{respond}$ and $t_{recover}$), which are comparable to those of the Pd/SCBD WO_3 film. Possible mechanisms responsible for the findings are discussed in this chapter.

6.1 Classification and naming of samples

The films samples used for this part of study were classified according to the settings of substrate temperature T_s and sputtering pressure P_s used in the deposition processes. As shown in Table 6.1, they can be classified into:

(i) four groups corresponding to four P_s values (3, 10, 30 and 60 mTorr), with each including samples deposited at T_s = 50, 350 and 550^{o}C for investigating the substrate temperature effect;

(ii) three groups corresponding to three T_s values (50, 350 and 550^{o}C), with each including samples deposited at P_s = 3, 10, 30 and 60 mTorr for investigating the sputtering pressure effect.

The name of a sample is designed to illustrate the values of T_s and P_s. For example, Sample WO50-3 refers to the film deposited at 50^{o}C and 3 mTorr.

Table 6.1 Classification and naming of samples.

P_s (mTorr) / T_s (^{o}C)	3	10	30	60
50	WO50-3	WO50-10	WO50-30	WO50-60
350	WO350-3	WO350-10	WO350-30	WO350-60
550	WO550-3	WO550-10	WO550-30	WO550-60

6.2 Structure of Pd/sputtered WO_3 films

6.2.1 Substrate temperature dependence

In this section, we present the T_s dependence of the structure of the Pd/sputtered WO_3 films in terms of their crystallite size (L), porosity (θ), thickness of the WO_3 layer (t_{WO_3}), surface roughness (z_{rms}) and Pd layer thickness (t_{Pd}). The data involved in the discussion are tabulated in Table 6.2.

Data of the sample group with P_s = 10 mTorr are presented to illustrate the main findings of the T_s effect, which are common to all other three sample groups of other P_s values. Their XRD spectra are shown in Figure 6.1 (a). It is seen that the structure of the film deposited at T_s = 50°C is highly disordered. Diffraction peaks of crystallites are seen when $T_s \geq 350$°C. Their intensities are stronger with further increase in T_s. The size of the crystallites (L) estimated from the widths of the peaks was found to increase monotonically with T_s (Table 6.2).

Raman spectra of the samples as shown in Figure 6.2 (a) give more structural information. The intensity of the 957-cm^{-1} component associated with the surface terminal W^{6+}=O bonds [125-127] diminishes with increasing T_s. This result is attributed to successive enhancement of inter-cluster connection accompanying with the growth of the crystallites [153-155]. The process starts with initial bridging at the contact area between adjacent nanoclusters (necking effect) [153, 154], followed by

further thickening of the linkages associated with the shrinkage of the inter-cluster area.

The films' porosity θ was estimated by substituting their refractive indexes measured by using prism coupler technique into the Clausius-Mosotti equation [118]. Their values were tablated in Table 6.2 for analysis. We note that with increasing T_s, the value of θ drops and the film thickness decreases concomitantly because of the densification of the film structure [156, 157]. Moreover, the AFM images (Figure 6.3) and surface roughness z_{rms} show that the films are scraggier, because larger crystallite facets and edges appear due to grain growth. This also makes the Pd coating more discontinuous when T_s increases. Though being fragmented, such a Pd film is still assigned to have a nominal thickness t_{Pd} of 1.2 nm according to the coating of Pd in a sputtering process.

Finally, we note that the structure of the films of all the four sample groups prepared at P_s = 3, 10, 30 and 60 mTorr show similar T_s dependences (Table 6.2). The main features are presented graphically in Figure 6.4.

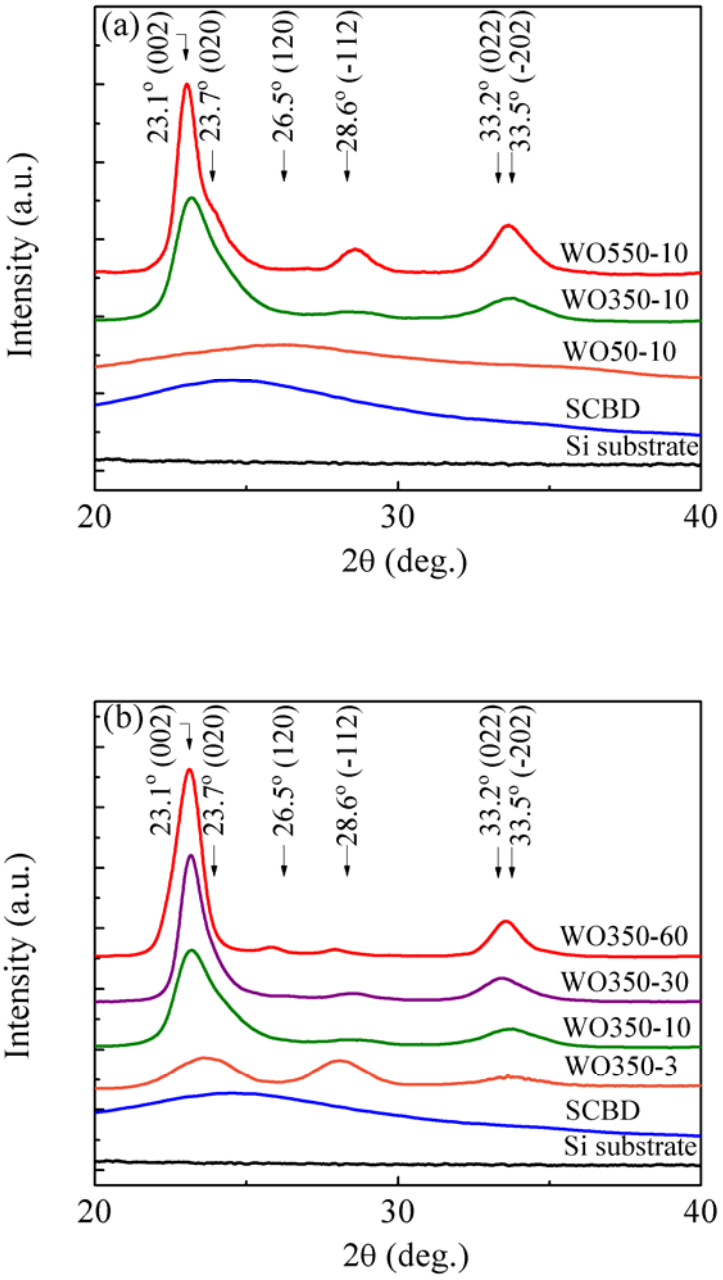

Figure 6.1 XRD pattern of a Pd/SCBD WO_3 film; and representative XRD patterns of a Pd/sputtered WO_3 films versus (a) T_s and (b) P_s.

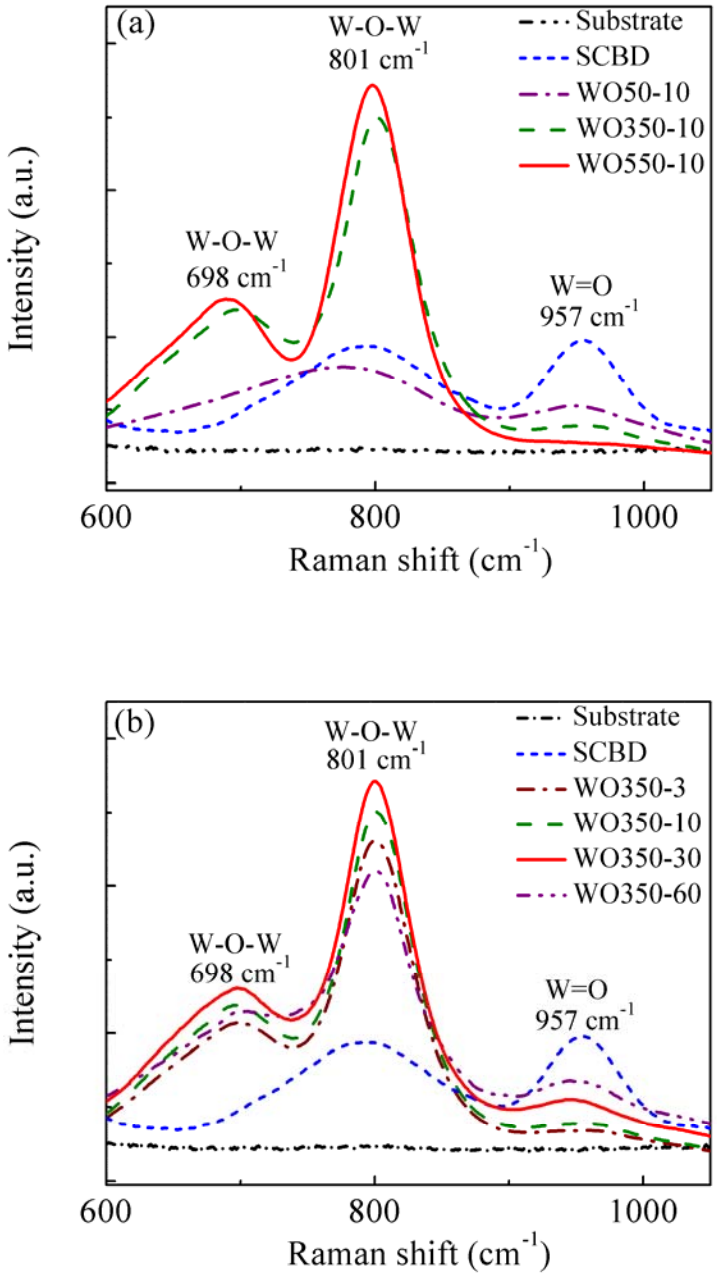

Figure 6.2 Raman spectrum of a Pd/SCBD WO_3; and representative Raman spectra of Pd/sputtered WO_3 films versus (a) T_s and (b) P_s.

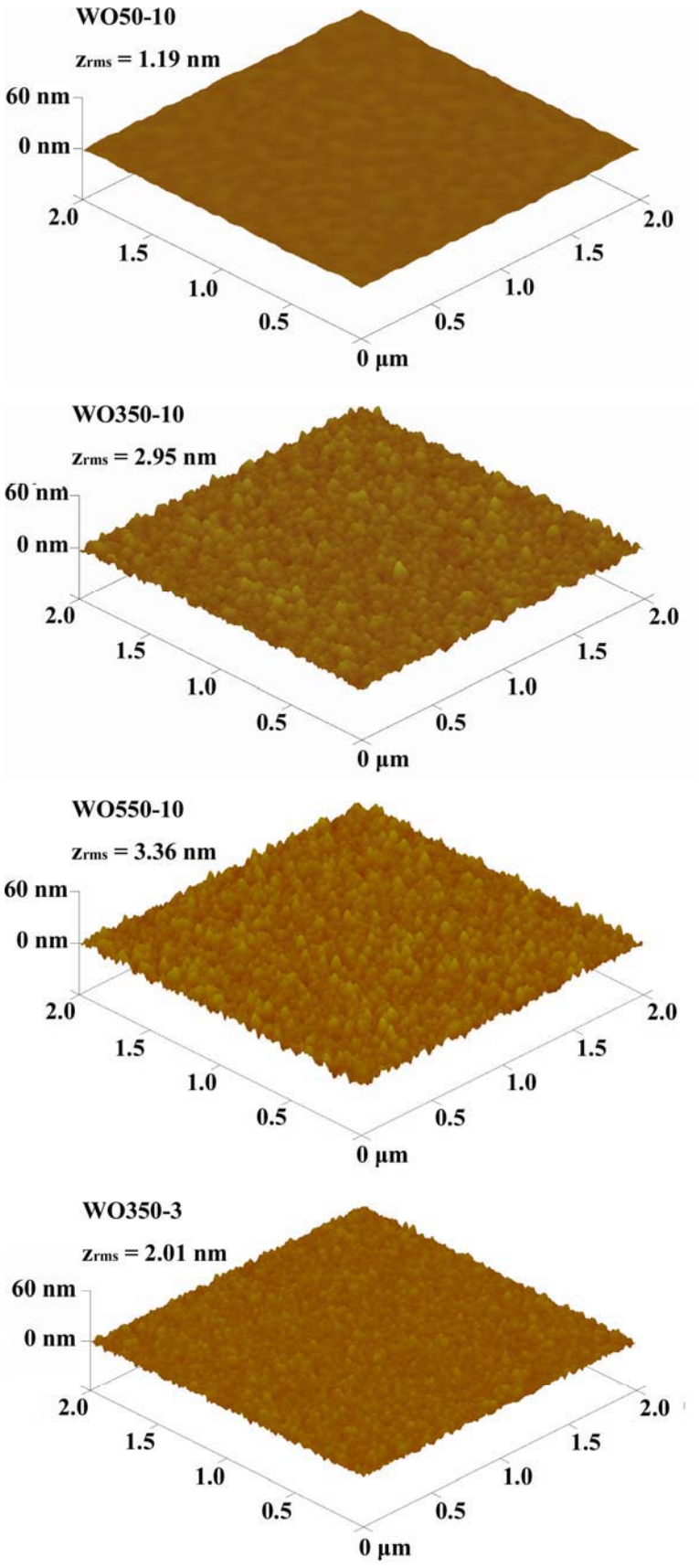
WO50-10
zrms = 1.19 nm
60 nm
0 nm
2.0
1.5
1.0
0.5
0 µm
WO350-10
zrms = 2.95 nm
WO550-10
zrms = 3.36 nm
WO350-3
zrms = 2.01 nm

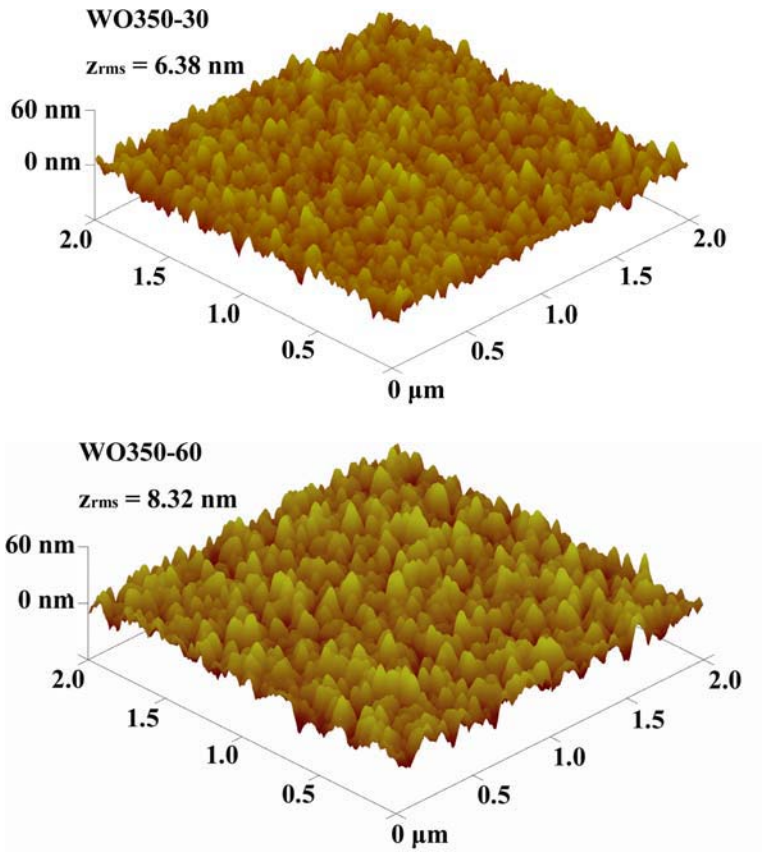

Figure 6.3 AFM images of sputtered WO_3 films.

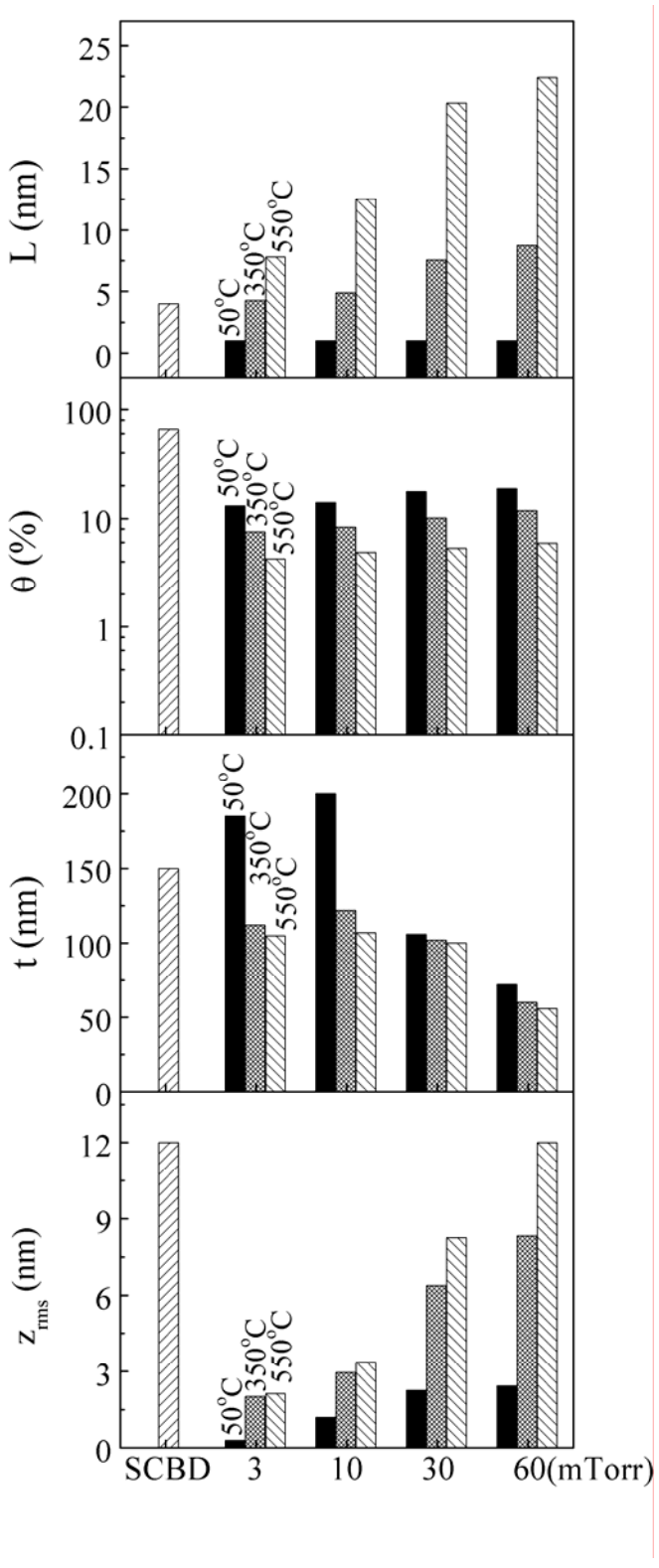

Figure 6.4 Structural parameters of an SCBD WO_3 film; and those of sputtered WO_3 films against T_s and P_s.

Table 6.2 Structure and H_2 sensing properties of Pd/SCBD WO_3 film and Pd/sputtered WO_3 films.

Sample	Structure						Gas sensing				
	L (nm)	n_f	θ (%)	t_{WO_3} (nm)	z_{rms} (nm)	t_{Pd} (nm)	R_o (GΩ)	R_{H_2} (kΩ)	S	$t_{respond}$ (s)	$t_{recover}$ (min)
SCBD	3–5 cluster	1.7	66	140	12.0	5	3660	3020	1.2×10^6	≤ 1	10
WO50-3	—	2.17	13.1	185	0.29	1.2	0.27	100	2.7×10^3	6	15
WO50-10	—	2.15	14.0	200	1.19	1.2	1.22	259	4.7×10^3	3	12
WO50-30	—	2.07	17.7	106	2.26	1.2	2.81	519	5.4×10^3	2	5
WO50-60	—	2.05	18.9	72	2.43	1.2	6.12	816	7.5×10^3	≤ 1	4
WO350-3	4.25	2.30	7.52	112	2.01	1.2	10.2	1.5	6.8×10^6	≤ 1	1350
WO350-10	4.9	2.28	8.34	122	2.95	1.2	23.7	3.1	7.6×10^6	≤ 1	1100
WO350-30	7.55	2.22	10.1	102	6.38	1.2	101	8.8	1.1×10^7	≤ 1	850
WO350-60	8.75	2.20	11.8	60	8.32	1.2	591	68	8.7×10^6	≤ 1	300
WO550-3	7.8	2.38	4.24	105	2.13	1.2	0.16	1.2	1.3×10^5	≤ 1	>2 days
WO550-10	12.5	2.37	4.89	107	3.36	1.2	0.41	2.5	1.6×10^5	≤ 1	>2 days
WO550-30	20.3	2.35	5.32	100	8.26	1.2	0.78	2.9	2.7×10^5	≤ 1	>2 days
WO550-60	22.4	2.34	5.91	56	12.0	1.2	0.86	5.1	1.7×10^5	≤ 1	>2 days

6.2.2 Sputtering pressure dependence

In this section, we present the sputtering pressure (P_s) dependence of the structure of the Pd/sputtered WO_3 films, in terms of crystallite size (L), porosity (θ), thickness of the WO_3 layer (t_{WO_3}), surface roughness (z_{rms}) and Pd layer thickness (t_{Pd}). All the data involved are tabulated in Table 6.2.

We selected the results of the sample group deposited at T_s = 350°C to present the main findings of the sputtering pressure P_s dependence of the film structure, which is common to other sample groups with different T_s values. Crystallite size (L) is estimated from the widths of X-ray diffraction peaks [Figure 6.1(b)], which is larger with increasing P_s. This result is understood by comparing the mean free path of a particle in a sputtering process with the distance from the target to the substrate (= 8.5 cm in our case). Consider a case of a low P_s = 3 mTorr. The mean free path of a particle is 2.7 cm (Figure 6.5) [69]. It experiences three times of scattering on average before reaching the target. Most of its kinetic energy, typically ≈ a few tens eV [157], is retained before landing. The energy level is strong enough to cause radiation damage to limit the growth of grain size [158-160]. Consider another case of a higher P_s = 60 mTorr. The mean free path is as short as 0.14 cm. A particle needs to experience 62 times of scattering before reaching the substrate. A substantial part of its kinetic energy is dissipated. Less radiation damages can be caused in the

deposits, allowing larger grains to be formed [158-160].

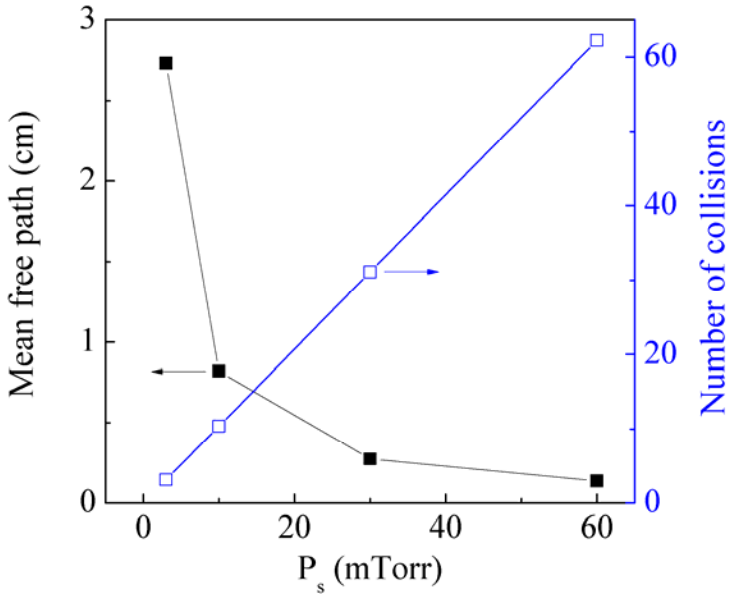

Figure 6.5 P_s dependence of mean free path and number of collisions for a particle travelling through a distance from the target to the substrate.

Raman spectra of the samples of this group are shown in Figure 6.2 (b). The 957-cm^{-1} component associated with the surface terminal W^{6+}=O bonds is observed in all the spectra. This result indicates that although a film deposited at a higher P_s level contains larger grains, the volume fraction of inter-cluster region is still unnegligible. When P_s increases, the inter-cluster connection is weakened and film structure becomes more porous. Unlike the effect of rising T_s, necking among nanoclusters may not occur.

The thickness of the WO_3 layer (t_{WO_3}) was found to rise with P_s first and then

dropped. The initial rise of t_{WO_3} is due to alleviated re-sputtering effect in a higher pressure environment [157, 159]. However, further increase in P_s aggravates scattering of the particles travelling towards the substrate. A lower deposition rate is resulted to produce a thinner WO_3 film (or smaller t_{WO_3}) [156].

AFM images of the film surfaces (Figure 6.3) show that their roughness z_{rms} increases with increasing P_s (Table 6.2). This is first due to the appearance of facets associated with grain growth [160]. Second, the increase of the volume fraction of the inter-cluster region also aggravates surface undulation. One more consequence is that the Pd coating becomes more uneven and fragmented.

Finally, we note that the structure of all the three sample groups prepared at T_s = 50, 350 and 550^{o}C show similar P_s dependences. The respective situations are presented graphically in Figure 6.4. Quantitative results are listed in Table 6.2.

6.3 Hydrogen sensing properties of Pd/sputtered WO_3 films

6.3.1 Substrate temperature dependence

In this section, we present the substrate temperature (T_s) dependences of the H_2 sensing properties of the Pd/sputtered WO_3 films in terms of their base resistance (R_o), hydrogenated film resistance (R_{H_2}), sensor response (S), response and recovery times ($t_{respond}$ and $t_{recover}$). These performance indexes are calculated from the

resistive response of Pd/sputtered WO_3 films as shown in Figure 6.6. The relationships between these performance indexes and the T_s are presented graphically in Figure 6.7. Quantitative results are tabulated in Table 6.2.

Consider R_o first. For the sample group deposited at a specific pressure P_s, with increasing T_s, the value of R_o rises first and then drops (Figure 6.7). The initial rise of R_o is attributed to increasing discontinuity of the Pd coating when the WO_3 layer becomes rougher. The ensuing drop of R_o is due to the enhanced crystallization of the WO_3 layer. Stronger crystallization may be associated with the presence of larger grain size. As such the volume fraction of the crystalline part in a grain with respect to that of the resistive depletion layer on the grain surface increases [38-40]. The charge carrier mobility is larger. Crystallization is also accompanied with stronger inter-cluster connection. The process starts with inter-cluster necking effect, where linkages between adjacent nanoclusters appear first with a size narrower than 2 times of the depletion layer of the WO_3 [37-40]. At this stage, the contact area remains depleted, so that the inter-cluster bridging does not cause any increase in electrical conductance and R_o remains high. When T_s increases to 550^oC, the inter-cluster linkages are thickened to a dimension such that it is not completely depleted in air. A drop of R_o starts to be observable. The use of even higher T_s further densifies the film structure, causing more gains to aggregate together and more prominent drop in R_o.

In a hydrogenation process, the resistance of the sensor changes by orders of magnitude, and hence is believed to be caused by the resistive change of the WO_3 layer rather than the Pd layer. Therefore, the drop of R_{H_2} with increasing T_s is explained by the enhancement of crystallization, which leads to larger grain size and modified inter-cluster connection as described above.

Consider sensor response S defined as $(R_o - R_{H_2})/ R_{H_2}$. When T_s increases from 50 to 350°C, the values of R_o and R_{H_2} are found to vary in an opposite manner, so that S is increased as a result. Meanwhile, the inter-cluster linkages grow but are still thinner than two times of the thickness of a depletion layer, so that R_o remains high. When the film is exposed to H_2, the inter-cluster linkages are deeply hydrogenated to set up conduction paths, causing the film resistance to drop across a broader range to result in a lower R_{H_2}. A larger S is thus achieved. For $T_s \geq 350$°C, both R_o and R_{H_2} drop with increasing T_s. R_o drops more prominently due to the stronger inter-cluster connection. The difference of $R_o - R_{H_2}$ is reduced to result in a drop of S.

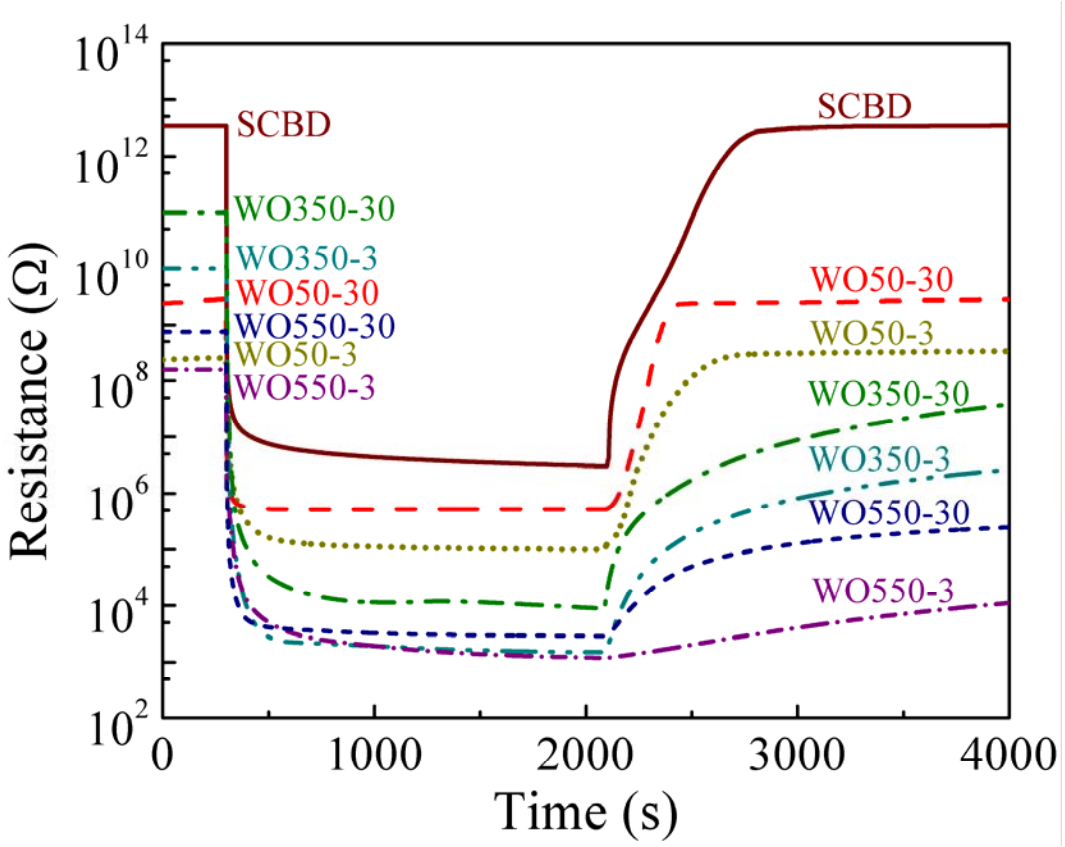

Figure 6.6 Resistive response of a Pd/SCBD WO_3 film and Pd/sputtered WO_3 films when hydrogenated in 2%H_2-air admixture and dehydrogenated in dry air at 80°C.

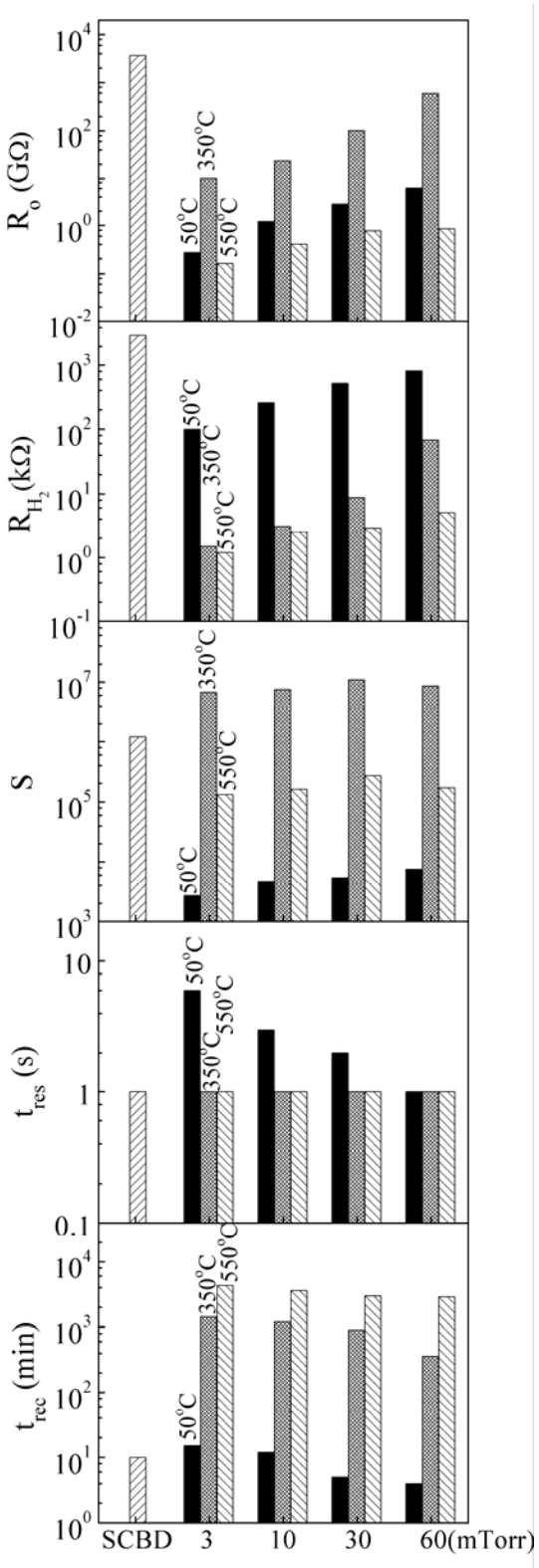

Figure 6.7 Gas sensing properties of a Pd/SCBD WO_3 film and Pd/sputtered WO_3 films versus T_s and P_s.

$t_{respond}$ is the time required for a thin surface layer of the WO_3 film to be hydrogenated. It is shorter when T_s increases. This phenomenon is attributed to enhancement of crystallization, involving the increase in grain size and improved inter-cluster connection.

$t_{recover}$ increases markedly from a few min to more than 2 days with increasing T_s. This is the time for most of the H atoms in a hydrogenated film to leave the film. Based on the argument presented in Section 4.1, along with the growth of grain size when T_s increases from 50 to 550^oC, the volume fraction of the inter-cluster region shrinks. As a consequence, it is hardly for oxygen species to migrate through the inter-cluster region. On the other hand, H^+ ions located inside the grains at different depths need to move and reach the film surface before they can meet and react with the oxygen species. This process limits effectively the reaction rate between the H^+ ions and oxygen species. Furthermore, H^+ ions may also be trapped somewhere in the film structure such that their motion is rather sluggish. These mechanisms explain why a film prepared at a higher T_s has a longer $t_{recover}$.

6.3.2 Sputtering pressure dependence

In this section, we present the sputtering pressure (P_s) dependences of the H_2 sensing properties of the Pd/sputtered WO_3 films. The relationships are presented graphically in Figure 6.7. Quantitative results are tabulated in Table 6.2.

For the sample group deposited at a specific substrate temperature T_s, the base resistance R_o increases monotonically with P_s. This tendency is attributed to

(i) more severe discontinuity or fragmentation of the Pd coating;

(ii) the increase of contact resistance among the WO_3 nanoclusters due to degraded inter-cluster connection as reflected by the results of Raman scattering analysis; and

(iii) the increase in porosity leading to a higher effective resistivity of the oxide.

The last two points are also applicable to explain the increase of R_{H_2} with increasing P_s.

As mentioned above, both R_o and R_{H_2} increase with increasing P_s. It happens that their difference rises at first and then drops with increasing P_s, such that the sensor response S defined according to their difference also exhibits similar P_s dependence. At last, we note that both $t_{respond}$ and $t_{recover}$ tend to drop with increasing P_s, because the porosity θ of the film structure increases to facilitate the movement of hydrogen and oxygen species.

6.3.3 Comparison with Pd/SCBD WO_3 films

The H_2 sensing properties of the Pd/Sputtered WO_3 films are compared with those of the Pd/SCBD WO_3 films. Referring to Figure 6.7 and the data tabulated in Table 6.2:

(i) The base resistance R_o of a Pd/SCBD WO_3 film is 3.66×10^{12} Ω, which is much higher than those of the Pd/sputtered WO_3 film samples. This is explained by considering that the SCBD WO_3 film is very rough so that the Pd coating on its surface is fragmentary and cannot provide a conductive pathway for charge carriers. Furthermore, the dimension of the nanoclusters in the Pd/SCBD WO_3 film is close to the thickness of the depletion layer of an MO_x material, namely ~ 3 nm [37-41], so that the nanoclusters are basically depleted in air and are highly resistive. Moreover, the SCBD WO_3 film structure is highly disordered, such that the mobilities of the charge carriers (including H^+ ions, electrons and oxygen vacancies) in the oxide are very low. At last, the poor inter-cluster connection generates additional contact resistance. The last two points also contribute to the high value of $R_{H_2} = 3.02\times10^6$ Ω. The sensor response of the SCBD WO_3 film, depending on the magnitude of $R_o - R_{H_2}$, reaches a level of 1.2×10^6, which is higher than the those of the Pd/Sputtered WO_3 films deposited at T_s = 50 and 550°C, but is lower than those deposited at 350°C.

(ii) The response time $t_{respond}$ of the Pd/SCBD WO_3 film is shorter than 1 s, which is a result of the small cluster size (3–5 nm) and the highly porous film structure (66%). Such a short $t_{respond}$ is comparable to those of the Pd/sputtered WO_3 films deposited at T_s = 350 and 550°C which are crystallized; and to that of the sputtered film deposited at 50°C and 60 mTorr with a highly porous structure.

(iii) The recovery time $t_{recover}$ of the Pd/SCBD WO_3 film is around 10 min. It falls in the range of $t_{recover}$ of the Pd/sputtered WO_3 films deposited at low T_s = 50°C, and is much shorter than those deposited at T_s = 350 and 550°C. The observed moderate $t_{recover}$ of the Pd/SCBD WO_3 film is due to the fast diffusion rate of H ions in a highly disordered WO_3 structure compared with that of a crystallized WO_3 film [161]; the fast spillover rate of oxygen species on the surfaces of the WO_3 nanoclusters [143, 162-164]; and formation of water molecules on the surfaces of the WO_3 nanoclusters to facilitate H ions to bridge across them [148, 151, 165, 166] and react with the oxygen species.

6.4 Conclusions

In conclusion, this study helps to get a comprehensive understanding on how the structure of a bi-layered Pd-coated sputtered WO_3 film affects its H_2 sensing properties, where the structure of the material is specified by crystallite size (L), porosity (θ), surface roughness (z_{rms}), and the thicknesses of the WO_3 layer and Pd coating. Importantly, the material structure can be effectively tailored by proper selection of fabrication conditions. Guidelines for pursuing specific H_2 sensor properties of this material system are summarized as follows.

In general, a H_2 sensor is preferred to have a large sensor response S, short response time $t_{respond}$ and recovery time $t_{recover}$. A sensor of these features is useable

for real-time monitoring and control of H_2 concentration in many industrial processes, like H_2 welding, metal heat treatment, hydrogen plasma-assisted material processing etc. In addition, since the H_2 sensor has fast response and recovery rates, it is highly reusable and is particularly suitably used for H_2 leakage alarming in a closed or indoor area such as a semiconductor lab, a H_2-fuel cell driven vehicle or a hydrogen plant etc. According to our results, a Pd-coated WO_3 based H_2 sensor can meet these requirements if its structure is made (i) to be highly disordered; (ii) to have a porosity ≥ 14% to facilitate spillover of H^+ ions during hydrogenation, and migration of both oxygen and H species to speed up their reaction during dehydrogenation; and (iii) to have a surface roughness z_{rms} exceeding the thickness of Pd catalyst layer for getting a high base resistance R_o. With these structural features, the value of S is in the range of 4.7×10^3–7.5×10^3, and $t_{respond}$ and $t_{recover}$ are shorter than 3 s and 12 min respectively. These requirements can be achieved by magnetron sputtering processes carried out at a low T_s, e.g. 50°C, and higher 20% Ar-80% O_2 pressure in the range of 10–60 mTorr.

In some applications where a disposable H_2 sensor of a higher sensor response and fast response rate are required, e.g. in a process where safety is more important than accurate control of H_2 gas concentration, a WO_3-based sensor prepared with sputtering technique at T_s = 350–550°C and 20% Ar-80% O_2 pressure between 3–60 mTorr is recommended. A WO_3 film produced with this condition contains narrow

inter-cluster linkages for the resistance varying in a moderate range suitable for measurements. The sensor response is fairly high. $t_{respond} \leq 1$ s and is fast enough for the needs of most applications. However, $t_{recover}$ is very long, i.e. 300 min to longer than two days, so that the sensor is not unsuitable for real-time monitoring application or to be reused after exposure to H_2.

Chapter 7 Conclusions and future work

7.1 HILE-type H_2 sensors

The first type of H_2 sensors developed in this project is based on the HILE effect. It is made by depositing a Pd film on a Si pillar or a 2-D Si pillar array, with the pillar(s) having large height-to-thickness ratio up to 30 : 1.

A sensor of this type has three advantages that have not been achieved concomitantly by other HILE-type sensors. First, the sensor's performance can be tailored by controlling the connectivity of the Pd film through tuning the size of the spacing around the pillars and Pd film thickness in a precise manner so as to suit the requirement of different applications. On one hand, for the use of generating fast warning signal due to H_2 leakage, the sensor can be made of a Pd layer deposited on a single Si pillar with isolation gaps of around 300 nm. Such a sensor is expected to be capable of giving a resistance drop by more than 1000 times within 1 s when exposed to air containing 4% of H_2, and recover to the base resistance within 3 s when H_2 is removed. On the other hand, a sensor of this type can be designed to give senor response with magnitudes depending on the H_2 concentration varying in a broad range of 0.002% to 6%. This can be achieved by depositing the Pd film on an array of more tightly spaced Si pillars for the Pd film to have higher structural and

electrical connectivity.

Second, the underlying Si pillar(s) is compliant, such that it can be bent and release part of the stresses generated by the HILE effect of Pd films during hydrogenation and dehydrogenation processes. Furthermore, the related normal compressive stress in the Pd required to close the gap is below the yield strength of Pd-H, i.e. 100 MPa. As a consequence, the sensor response is more durable, with the gas sensing performance to be more stable and reproducible over a long period of use. The addition of an Au/Cr buffer layer directly under the Pd layer helps to alleviate the resistance change due to the plastic deformation and/or peeling off of Pd film. Note that the Au/Cr also helps to eliminate the response due to the change of resistivity associated with hydridation of the Pd film, which induces a drop of the sensor resistance which is opposite to response caused by the HILE effect.

Moreover, the response and response times of the sensor are found to decrease with increasing $T_{operate}$. These results can be attributed to the reduced solubility of H atoms in Pd-H hydride at a specified elevated temperature. We further point out that the sensor response in an environment containing oxygen is weaker than that in an oxygen free one, because oxygen molecules can react with hydrogen species and obstruct them to adhere to the oxide surface. The resistance change of the oxide due to hydrogen is thereby suppressed.

Third, the adoption of micro fabrication process and physical vapor deposition

methods as employed in this study would allow miniaturization and mass production of the sensors.

7.2 Nanocluster-assembled highly porous Pd/SCBD WO_3 film H_2 sensors

The second type of H_2 sensors developed in this study is Pd/SCBD WO_3 film sensors, which are made to be constructed of loosely packed 3–5 nm oxide clusters and have an extremely high porosity of 66% concomitantly. Such a film structure can give both high sensor response and fast response rate. We found that such a character has not been achieved by most other MO_x hydrogen sensing materials reported so far and claimed to have "nano" structures.

$T_{operate}$ dependence of the H_2 sensing properties of Pd/SCBD WO_3 films was investigated. At low $T_{operate}$, the sensor response is higher, but the response time is too long for the response to reach equilibrium in a reasonable period of time. However, if the measurement temperature $T_{operate}$ is slightly increased, say to 80°C, the sensor response is reduced mildly, but the response time is substantially shortened to around 5 min. A Pd/SCBD WO_3 hydrogen sensor operating at 80°C shows more other advantages and is recognized to be very useful in practice.

Sensor response and response time measured at 80°C are compared with other nano-MO_x based H_2 sensors reported in literature. These sensors are either made of

small nanoclusters embedded in dense matrixes, or are made of loosely packed 1-D nano-sized elements (e.g. nanowires, nanofibres and nanobelts). The former mostly has large sensor response but long response time due to prolonged diffusion process of gas molecules in the dense matrix; and the latter have faster response rate but the sensor response is lower because the 1-D elements are actually rather thick. A Pd/SCBD WO_3 film is constructed of genuine 3 to 5-nm nanoclusters and has a very high porosity around 66%, such that it can give both larger sensor response and faster response rate simultaneously. Its overall performance is superior to most reported nano-MO_x based H_2 sensors operating at room or elevated temperatures ≥ 200^{o}C.

The Pd/SCBD WO_3 film sensor was also found to have high cyclic stability over more than 2400 cycles without showing any sign of degradation. It also showed strong interference resistance against a number of VOC vapours. Importantly, the sensor operating at 80^{o}C is entirely unaffected by the change of relative humidity, which can cause severe interference to the same sensor operating at 20^{o}C. Ambient pressure dependence of the sensing performance is mild. The film also has other advantages including miniaturizability; compatible with silicon-based micro fabrication techniques, scalability in mass production; high batch-to-batch reproducibility adherent to the physical nature of an SCBD process.

7.3 Attainability of high-quality Pd/sputtered WO_3 film H_2 sensors

High-quality H_2 sensors can be made of Pd-coated sputtering WO_3 thin films. The finding has practical meaning because sputtering is a broadly used technique in material processing, and has great flexibility in controlling the composition of the deposits.

Results show that the structure of sputtered WO_3 films can be controlled by varying the substrate temperature T_s and sputtering pressure P_s in broad ranges of 50–550^oC and 3–60mTorr respectively. The changes of the film structure lead to corresponding changes of the H_2 sensing properties. Results also help to understand how physical mechanisms correlating the structure of a Pd/sputtered WO_3 films and the H_2 sensing properties. The guidelines for attaining a Pd/sputtered WO_3 film of certain features of H_2 sensing properties are set up and summarized as follows.

A Pd/sputtered WO_3 film sensor with a strong sensor response S, short response time $t_{respond}$ and recovery time $t_{recover}$ for the use of real-time monitoring or control of H_2 concentration is required to be highly disordered and have a porosity ≥ 14% to facilitate spillover of H^+ ions and speed up migration of both oxygen and H species. It is also required to have a rough surface for the Pd coating to become fragmentary, such that the sensor can have a high base resistance R_o to give a strong sensor response. With these structural features, the value of S is in the range of 4.7×10^3–

7.5×10^3, and $t_{respond}$ and $t_{recover}$ are shorter than 3 s and 12 min respectively. These requirements can be achieved by a magnetron sputtering processes carried out at a low T_s of 50°C with higher sputtering pressure (of the 20% Ar-80% O_2 admixture) in the range of 10–60 mTorr.

In some other applications requiring a H_2 sensor of a higher sensor response and fast response rate but not particularly requiring a fast recovery rate, a Pd/sputtered WO_3 film sensor prepared at T_s = 350–550°C and sputtering pressure between 3–60 mTorr is recommended. A WO_3 film produced with this condition contains narrow inter-cluster linkages for the resistance varying in a moderate range suitable for measurements. The sensor response is fairly high. $t_{respond} \leq 1$ s and is fast enough for the needs of most of these applications. However, $t_{recover}$ is very long, i.e. 300 min to longer than two days, so that the sensor is not unsuitable for real-time monitoring application or to be reused after exposure to H_2.

7.4 Comments on the applications of three different types of hydrogen sensors

In general, a H_2 sensor is preferred to have a high sensor response S, short response time $t_{respond}$ and recovery time $t_{recover}$. A sensor of these features is useable for real-time monitoring and control of H_2 concentration in many industrial processes, like H_2 welding, metal heat treatment, hydrogen plasma-assisted material

processing etc. In addition, since the H_2 sensor has fast response and recovery rates, it is highly reusable and particularly suitable to be used for H_2 leakage alarming in a closed area such as a semiconductor lab, a H_2-fuel cell driven vehicle or a hydrogen plant etc. According to our results, the Pd/Si pillar array sensor, Pd/SCBD WO_3 film sensor and Pd/sputtered WO_3 film sensor fabricated at T_s = 50°C and a sputtering pressure P_s in the range of 10 - 60 mTorr can meet these requirements.

In some application where fast response rate is required, e.g. in a process where safety is more important than accurate control of H_2 gas concentration, the Pd/Si pillar sensor, Pd/SCBD WO_3 film sensor and Pd/sputtered WO_3 film sensor fabricated at T_s = 350 - 550°C and P_s = 10 - 60 mTorr can meet these requirements.

7.5 Future work

For Pd/Si pillar array sensor, the threshold H_2 concentration, corresponding to the on-set of the resistance-H_2 concentration curve, is controllable by varying the structural connectivity of the Pd film. This result inspires us to pursue a future study on developing multisensor array by assembling Pd sensor elements made to have different structural connectivity. The assembly can give very high senor response over a broad detection range of H_2 concentration.

For an MO_x-based gas sensor with the MO_x material in the form of particles or thin film, it is of great importance to control the oxide's dimension in the order of a

few nm (~ 3 nm) and at the same time the overall structure to have a large porosity. The charge carriers in the oxide material are basically depleted in air, because the said dimension is smaller than the thickness of the depletion layer. Furthermore, because of the high porosity, the gas molecules can diffuse into the interior of the sensor material agilely. Therefore, we expect that an ultrathin WO_3 film with thickness below 3 nm can also be considered as a material possessing gas sensing functions similar to those of a highly porous WO_3 material made of extremely small clusters. In a pilot experiment, we fabricated ultrathin WO_3 film by using SCBD and sputtering techniques respectively. The ultrathin WO_3 films were found to have higher sensor response, shorter response and recovery times compared with a thicker WO_3 film. This preliminary findings further motivate us to look for future study on the gas sensing properties of ultrathin MO_x films fabricated by using SCBD, sputtering and laser molecular beam expitaxy methods.

References

[1] A. Zuttel, A. Borgschulte, L. Schlapbach, Hydrogen as a future energy carrier, Wiley-VCH, Federal Republic of Germany, 2008, pp. 91.

[2] F. Yang, D.K. Taggart, R.M. Penner, Joule heating a palladium nanowire sensor for accelerated response and recovery to hydrogen gas, Small, 6 (2010) 1422-1429.

[3] L. Boon-Brett, J. Bousek, P. Castello, O. Salyk, F. Harskamp, L. Aldea, F. Tinaut, Reliability of commercially available hydrogen sensors for detection of hydrogen at critical concentrations: Part I - Testing facility and methodologies, Int. J. Hydrogen Energ. 33 (2008) 7648-7657.

[4] L. Boon-Brett, J. Bousek, P. Moretto, Reliability of commercially available hydrogen sensors for detection of hydrogen at critical concentrations: Part II - selected sensor test results, Int. J. Hydrogen Energ. 34 (2009) 562-571.

[5] T. Hubert, L. Boon-Brett, G. Black, U. Banach, Hydrogen sensors - a review, Sensor. Actuat. B: Chem. 157 (2011) 329-352.

[6] L. Boon-Brett, J. Bousek, G. Black, P. Moretto, P. Castello, T. Hubert, U. Banach, Identifying performance gaps in hydrogen safety sensor technology for automotive and stationary applications, Int. J. Hydrogen Energ. 35 (2010) 373-384.

[7] V.M. Aroutiounian, Hydrogen detectors, Int. Sci. J. Alter. Energ. and Ecolog. 23 (2005) 21-31.

[8] J. Tollefson, Fuel of the Future, Nature, 464 (2010) 1262-1264.

[9] M. Ball, M. Wietschel, The hydrogen economy: opportunities and challenges, Combridge university press, United Kingdom, 2009, pp. 68.

[10] Y.M. Tang, C.W. Ong, Analysis and improvement of cyclic stability of H_2 sensing properties of Pd/Mg-Ni films, Int. J. Hydrogen Energ. 36 (2011) 10188-10196.

[11] Y.M. Tang, C.W. Ong, Stability of hydrogen-induced optical switching properties of palladium-coated magnesium-nickel films, Solid State Ionics, 184 (2011) 88-91.

[12] M. Zhao, J.X. Huang, M.H. Wong, Y.M. Tang, C.W. Ong, Versatile computer-controlled system for characterization of gas sensing materials, Rev. Sci. Instrum. 82 (2011) 105001.

[13] R. Gupta, A.A. Sagade, G.U. Kulkarni, A low cost optical hydrogen sensing device using nanocrystalline Pd grating, Int. J. Hydrogen Energ. 37 (2012) 9443-9449.

[14] F.J. Ibanez, F.P. Zamborini, Chemiresistive sensing with chemically modified metal and alloy nanoparticles, Small, 8 (2012) 174-202.

[15] S.F. Silva, L. Coelho, O. Frazao, J.L. Santos, F.X. Malcata, A review of

palladium-based fiber-optic sensors for molecular hydrogen detection, IEEE Sens. J. 12 (2012) 93-102.

[16] L.G. Villanueva, F. Fargier, T. Kiefer, M. Ramonda, J. Brugger, F. Favier, Highly ordered palladium nanodot patterns for full concentration range hydrogen sensing, Nanoscale, 4 (2012) 1964-1967.

[17] J.H. Yoon, B.J. Kim, J.S. Kim, Design and fabrication of micro hydrogen gas sensors using palladium thin film, Mater. Chem. Phys. 133 (2012) 987-991.

[18] M.A. Lim, D.H. Kim, C.O. Park, Y.W. Lee, S.W. Han, Z.Y. Li, R.S. Williams, I. Park, A new route toward ultrasensitive, flexible chemical sensors: metal nanotubes by wet-chemical synthesis along sacrificial nanowire templates, ACS Nano, 6 (2012) 598-608.

[19] B.K. Duan, J.Y. Zhang, P.W. Bohn, Conductance-based chemical sensing in metallic nanowires and metal-semiconductor nanostructures, Anal. Chem. 84 (2012) 2-8.

[20] X.Q. Zeng, Y.L. Wang, H. Deng, M.L. Latimer, Z.L. Xiao, J. Pearson, T. Xu, H.H. Wang, U. Welp, G.W. Crabtree, W.K. Kwok, Networks of ultrasmall Pd/Cr nanowires as high performance hydrogen sensors, ACS Nano, 5 (2011) 7443-7452.

[21] X.Q. Zeng, M.L. Latimer, Z.L. Xiao, S. Panuganti, U. Welp, W.K. Kwok, T. Xu, Hydrogen gas sensing with networks of ultrasmall palladium nanowires

formed on filtration membranes, Nano Lett. 11 (2011) 262-268.

[22] N. Tasaltin, S. Ozturk, N. Kilinc, Z.Z. Ozturk, Investigation of the hydrogen gas sensing properties of nanoporous Pd alloy films based on AAO templates, J. Alloy Compd. 509 (2011) 4701-4706.

[23] B.L. Huy, S. Kumar, G.H. Kim, Manipulation of palladium nanoparticles in a 20 nm gap between electrodes for hydrogen sensor application, J. Phys. D: Appl. Phys. 44 (2011) 325402.

[24] F. Yang, S.C. Kung, M. Cheng, J.C. Hemminger, R.M. Penner, Smaller is faster and more sensitive: the effect of wire size on the detection of hydrogen by single palladium nanowires, ACS Nano, 4 (2010) 5233-5244.

[25] E. Lee, J.M. Lee, E. Lee, J.S. Noh, J.H. Joe, B. Jung, W. Lee, Hydrogen gas sensing performance of Pd-Ni alloy thin films, Thin Solid Films, 519 (2010) 880-884.

[26] K.J. Jeon, J.M. Lee, E. Lee, W. Lee, Individual Pd nanowire hydrogen sensors fabricated by electron-beam lithography, Nanotechnology, 20 (2009) 135502.

[27] F. Favier, Nanogaps for sensing, Procedia Chem. 1 (2009) 746-749.

[28] S. Mubeen, B. Yoo, N.V. Myung, Fabrication of nanoelectrodes and nanojunction hydrogen sensor, Appl. Phys. Lett. 93 (2008) 133111.

[29] D.Y. Ding, Z. Chen, A pyrolytic carbon-stabilized nanoporous Pd film for wide-range H_2 sensing, Adv. Mater. 19 (2007) 1996-1999.

[30] F.A. Lewis, The palladium hydrogen system, Academic Press, London, 1967, pp. 3.

[31] H.S. Nalwa, Nanoclusters and nanocrystals, American Scientific Publisher, Stevenson Ranch, California, USA, 2003, pp. 53.

[32] E.A. Owen, J.I. Jones, The effect of pressure and temperature on the occlusion of hydrogen by palladium, Proceedings of the Physical Society, 49 (1937) 587-602.

[33] J.C. Barton, F.A. Lewis, I. Woodward, Hysteresis of the relationships between electrical resistance and the hydrogen content of palladium, Trans. Faraday Soc. 59 (1963) 1201-1207.

[34] Y. Sakamoto, I. Takashima, Hysteresis behaviour of electrical resistance of the Pd-H system measured by a gas-phase method, J. Phys. Condens. Mater. 8 (1996) 10511-10520.

[35] M. Wang, Y. Feng, Palladium-silver thin film for hydrogen sensing, Sensor. Actuat. B: Chem. 123 (2007) 101-106.

[36] S. Akbar, P. Dutta, C.H. Lee, High-temperature ceramic gas sensors: a review, Int. J. Appl. Ceram. Tec. 3 (2006) 302-311.

[37] N. Barsan, D. Koziej, U. Weimar, Metal oxide-based gas sensor research: how to, Sensor. Actuat. B: Chem. 121 (2007) 18-35.

[38] N. Barsan, U. Weimar, Conduction model of metal oxide gas sensors, J.

Electroceram. 7 (2001) 143-167.

[39] M.E. Franke, T.J. Koplin, U. Simon, Metal and metal oxide nanoparticles in chemiresistors: does the nanoscale matter, Small, 2 (2006) 36-50.

[40] N. Yamazoe, New approaches for improving semiconductor gas sensors, Sensor. Actuat. B: Chem. 5 (1991) 7-19.

[41] G. Korotcenkov, Gas response control through structural and chemical modification of metal oxide films: state of the art and approaches, Sensor. Actuat. B: Chem. 107 (2005) 209-232.

[42] E. Comini, C. Baratto, G. Faglia, M. Ferroni, A. Vomiero, G. Sberveglieri, Quasi-one dimensional metal oxide semiconductors: preparation, characterization and application as chemical sensors, Prog. Mater. Sci. 54 (2009) 1-67.

[43] G. Eranna, B.C. Joshi, D.P. Runthala, R.P. Gupta, Oxide materials for development of integrated gas sensors - a comprehensive review, Crit. Rev. Solid State. 29 (2004) 111-188.

[44] X.J. Huang, Y.K. Choi, Chemical sensors based on nanostructured materials, Sensor. Actuat. B: Chem. 122 (2007) 659-671.

[45] A. Kolmakov, M. Moskovits, Chemical sensing and catalysis by one-dimensional metal-oxide nanostructures, Annu. Rev. Mater. Res. 34 (2004) 151-180.

[46] G. Korotcenkov, Metal oxides for solid-state gas sensors: what determines our choice, Mater. Sci. Eng. B: Solid, 139 (2007) 1-23.

[47] G. Korotcenkov, B.K. Cho, Instability of metal oxide-based conductometric gas sensors and approaches to stability improvement, Sensor. Actuat. B: Chem. 156 (2011) 527-538.

[48] J.G. Lu, P.C. Chang, Z.Y. Fan, Quasi-one-dimensional metal oxide materials - synthesis, properties and applications, Mater. Sci. Eng. R, 52 (2006) 49-91.

[49] A.C. Romain, J. Nicolas, Long term stability of metal oxide-based gas sensors for e-nose environmental applications: an overview, Sensor. Actuat. B: Chem. 146 (2010) 502-506.

[50] K. Sahner, H.L. Tuller, Novel deposition techniques for metal oxide: prospects for gas sensing, J. Electroceram. 24 (2010) 177-199.

[51] Y. Shimizu, T. Maekawa, Y. Nakamura, M. Egashira, Effects of gas diffusivity and reactivity on sensing properties of thick film SnO_2-based sensors, Sensor. Actuat. B: Chem. 46 (1998) 163-168.

[52] C.X. Wang, L.W. Yin, L.Y. Zhang, D. Xiang, R. Gao, Metal oxide gas sensors: sensitivity and influencing factors, Sensors-Basel, 10 (2010) 2088-2106.

[53] N. Yamazoe, G. Sakai, K. Shimanoe, Oxide semiconductor gas sensors, Catal. Surv. Asia. 7 (2003) 63-75.

[54] Y.T. Chao, S. Yao, W.J. Buttner, J.R. Stetter, Amperometric sensor for selective

and stable hydrogen measurement, Sensor. Actuat. B: Chem. 106 (2005) 784-790.

[55] G. Korotcenkov, S. Do Han, J.R. Stetter, Review of electrochemical hydrogen sensors, Chem. Rev. 109 (2009) 1402-1433.

[56] X.B. Lu, S.G. Wu, L. Wang, Z.X. Su, Solid-state amperometric hydrogen sensor based on polymer electrolyte membrane fuel cell, Sensor. Actuat. B: Chem. 107 (2005) 812-817.

[57] C.H. Han, D.W. Hong, S.D. Han, J. Gwak, K.C. Singh, Catalytic combustion type hydrogen gas sensor using TiO_2 and UV-LED, Sensor. Actuat. B: Chem. 125 (2007) 224-228.

[58] M. Nishibori, W. Shin, N. Izu, T. Itoh, I. Matsubara, S. Yasuda, S. Ohtani, Robust hydrogen detection system with a thermoelectric hydrogen sensor for hydrogen station application, Int. J. Hydrogen Energ. 34 (2009) 2834-2841.

[59] W. Shin, K. Imai, N. Izu, N. Murayama, Thermoelectric thick-film hydrogen gas sensor operating at room temperature, Jpn. J. Appl. Phys. 40 (2001) L1232-L1234.

[60] I. Simon, M. Arndt, Thermal and gas-sensing properties of a micromachined thermal conductivity sensor for the detection of hydrogen in automotive applications, Sensor. Actuat. A: Phys. 97-8 (2002) 104-108.

[61] M.Z. Atashbar, D. Banerji, S. Singamaneni, Room-temperature hydrogen

sensor based on palladium nanowires, IEEE Sens. J. 5 (2005) 792-797.

[62] F. Favier, E.C. Walter, M.P. Zach, T. Benter, R.M. Penner, Hydrogen sensors and switches from electrodeposited palladium mesowire arrays, Science, 293 (2001) 2227-2231.

[63] M.Z. Atashbar, S. Singamaneni, Room temperature gas sensor based on metallic nanowires, Sensor. Actuat. B: Chem. 111 (2005) 13-21.

[64] S. Cherevko, N. Kulyk, J. Fu, C.H. Chung, Hydrogen sensing performance of electrodeposited conoidal palladium nanowire and nanotube arrays, Sensor. Actuat. B: Chem. 136 (2009) 388-391.

[65] A. Gurlo, D.R. Clarke, High-Sensitivity Hydrogen Detection: hydrogen-induced swelling of multiple cracked palladium films on compliant substrates, Angew. Chem. Int. Edit. 50 (2011) 10130-10132.

[66] V. La Ferrara, B. Alfano, E. Massera, G. Di Francia, Palladium nanowires assembly by dielectrophoresis investigated as hydrogen sensors, IEEE Trans. Nanotechnol. 7 (2008) 776-781.

[67] J. Lee, J.S. Noh, S.H. Lee, B. Song, H. Jung, W. Kim, W. Lee, Cracked palladium films on an elastomeric substrate for use as hydrogen sensors, Int. J. Hydrogen Energ. 37 (2012) 7934-7939.

[68] J. Lee, W. Shim, E. Lee, J.S. Noh, W. Lee, Highly mobile palladium thin films on an elastomeric substrate: nanogap-based hydrogen gas sensors, Angew.

Chem. Int. Edit. 50 (2011) 5301-5305.

[69] C.W. Ong, Y.M. Tang, Sputtering pressure dependence of hydrogen-sensing effect of palladium films, J. Mater. Res. 24 (2009) 1919-1927.

[70] F. Yang, D.K. Taggart, R.M. Penner, Fast, sensitive hydrogen gas detection using single palladium nanowires that resist fracture, Nano Lett. 9 (2009) 2177-2182.

[71] M.J. Beliatis, N.A. Martin, E.J. Leming, S.R.P. Silva, S.J. Henley, Laser ablation direct writing of metal nanoparticles for hydrogen and humidity sensors, Langmuir, 27 (2011) 1241-1244.

[72] O. Dankert, A. Pundt, Hydrogen-induced percolation in discontinuous films, Appl. Phys. Lett. 81 (2002) 1618-1620.

[73] T. Kiefer, L.G. Villanueva, F. Fargier, F. Favier, J. Brugger, The transition in hydrogen sensing behavior in noncontinuous palladium films, Appl. Phys. Lett. 97 (2010) 121911.

[74] T. Kiefer, L.G. Villanueva, F. Fargier, F. Favier, J. Brugger, Fast and robust hydrogen sensors based on discontinuous palladium films on polyimide, fabricated on a wafer scale, Nanotechnology, 21 (2010) 505501.

[75] M. Ramanathan, G. Skudlarek, H.H. Wang, S.B. Darling, Crossover behavior in the hydrogen sensing mechanism for palladium ultrathin films, Nanotechnology, 21 (2010) 125501.

[76] S.T. Ren, Q. Wang, Y.S. Wang, S.L. Qu, Three distinct hydrogen sensing responses of palladium line patterns generated by femtosecond laser direct writing, J. Phys. D: Appl. Phys. 45 (2012) 285503.

[77] J. van Lith, A. Lassesson, S.A. Brown, M. Schulze, J.G. Partridge, A. Ayesh, A hydrogen sensor based on tunneling between palladium clusters, Appl. Phys. Lett. 91 (2007) 181910.

[78] T. Xu, M.P. Zach, Z.L. Xiao, D. Rosenmann, U. Welp, W.K. Kwok, G.W. Crabtree, Self-assembled monolayer-enhanced hydrogen sensing with ultrathin palladium films, Appl. Phys. Lett. 86 (2005) 203104.

[79] M. Khanuja, S. Kala, B.R. Mehta, F.E. Kruis, Concentration-specific hydrogen sensing behavior in monosized Pd nanoparticle layers, Nanotechnology, 20 (2009) 015502.

[80] M. Khanuja, D. Varandani, B.R. Mehta, Pulse like hydrogen sensing response in Pd nanoparticle layers, Appl. Phys. Lett. 91 (2007) 253121.

[81] Y.T. Lee, J.M. Lee, Y.J. Kim, J.H. Joe, W. Lee, Hydrogen gas sensing properties of PdO thin films with nano-sized cracks, Nanotechnology, 21 (2010) 165503.

[82] B. Xie, L.L. Liu, X. Peng, Y. Zhang, Q. Xu, M.Y. Zheng, T. Takiya, M. Han, Optimizing hydrogen sensing behavior by controlling the coverage in Pd nanoparticle films, J. Phys. Chem. C, 115 (2011) 16161-16166.

[83] B. Xie, S.S. Zhang, F. Liu, X. Peng, F.Q. Song, G.H. Wang, M. Han, Response behavior of a palladium nanoparticle array based hydrogen sensor in hydrogen-nitrogen mixture, Sensor. Actuat. A: Phys. 181 (2012) 20-24.

[84] Y.S. Hu, D. Perello, U. Mushtaq, M.H. Yun, A single palladium nanowire via electrophoresis deposition used as a ultrasensitive hydrogen sensor, IEEE Trans. Nanotechnol. 7 (2008) 693-699.

[85] Y. Im, C. Lee, R.P. Vasquez, M.A. Bangar, N.V. Myung, E.J. Menke, R.M. Penner, M.H. Yun, Investigation of a single Pd nanowire for use as a hydrogen sensor, Small, 2 (2006) 356-358.

[86] R. Dasari, F.P. Zamborini, Hydrogen switches and sensors fabricated by combining electropolymerization and Pd electrodeposition at microgap electrodes, J. Am. Chem. Soc. 130 (2008) 16138-16139.

[87] T. Kiefer, A. Salette, L.G. Villanueva, J. Brugger, Large arrays of chemo-mechanical nanoswitches for ultralow-power hydrogen sensing, J. Micromech. Microeng. 20 (2010) 105019.

[88] W.Z. Jia, L. Su, Y. Ding, A. Schempf, Y. Wang, Y. Lei, Pd/TiO_2 nanotibrous membranes and their application in hydrogen sensing, J. Phys. Chem. C, 113 (2009) 16402-16407.

[89] K. Luongo, A.R. Sine, S. Bhansali, Development of a highly sensitive porous Si-based hydrogen sensor using Pd nano-structures, Sensor. Actuat. B: Chem.

111 (2005) 125-129.

[90] J.S. Noh, H. Kim, B.S. Kim, E. Lee, H.H. Cho, W. Lee, High-performance vertical hydrogen sensors using Pd-coated rough Si nanowires, J. Mater. Chem. 21 (2011) 15935-15939.

[91] J. Lee, W. Shim, J.S. Noh, W. Lee, Design rules for nanogap-based hydrogen gas sensors, Mater. Phys. chem. 13 (2012) 1395-1403.

[92] J.L. Zou, K.S. Iyer, C.L. Raston, Hydrogen-induced reversible insulator-metal transition in a palladium nanosphere sensor, Small, 6 (2010) 2358-2361.

[93] F.J. Ibanez, F.P. Zamborini, Ozone- and thermally activated films of palladium monolayer-protected clusters for chemiresistive hydrogen sensing, Langmuir, 22 (2006) 9789-9796.

[94] M. Moreno, F.J. Ibanez, J.B. Jasinski, F.P. Zamborini, Hydrogen reactivity of palladium nanoparticles coated with mixed monolayers of alkyl thiols and alkyl amines for sensing and catalysis applications, J. Am. Chem. Soc. 133 (2011) 4389-4397.

[95] T. Kiefer, F. Favier, O. Vazquez-Mena, G. Villanueva, J. Brugger, A single nanotrench in a palladium microwire for hydrogen detection, Nanotechnology, 19 (2008) 125502.

[96] H. Shanak, H. Schmitt, J. Nowoczin, C. Ziebert, Effect of Pt-catalyst on gasochromic WO_3 films: optical, electrical and AFM investigations, Solid State

Ionics, 171 (2004) 99-106.

[97] L.C. Tien, P.W. Sadik, D.P. Norton, L.F. Voss, S.J. Pearton, H.T. Wang, B.S. Kang, F. Ren, J. Jun, J. Lin, Hydrogen sensing at room temperature with Pt-coated ZnO thin films and nanorods, Appl. Phys. Lett. 87 (2005) 222106.

[98] J.S. Lin, D.P. Norton, S.J. Pearton, inventors; University of Flordia Research Foundation Inc., assignee. System for hydrogen sensing, World Patent, WO 2008/041983, 2008 Apr 10.

[99] O. Lupan, V.V. Ursaki, G. Chai, L. Chow, G.A. Emelchenko, I.M. Tiginyanu, A.N. Gruzintsev, A.N. Redkin, Selective hydrogen gas nanosensor using individual ZnO nanowire with fast response at room temperature, Sensor. Actuat. B: Chem. 144 (2010) 56-66.

[100] L.L. Fields, J.P. Zheng, Y. Cheng, P. Xiong, Room-temperature low-power hydrogen sensor based on a single tin dioxide nanobelt, Appl. Phys. Lett. 88 (2006) 263102.

[101] I. D. Kim, J.M. Hong, D.Y. Kim, S.M. Jo, inventors; Korea Institute of Science and Technology, assignee. Ultrasensitive metal oxide gas sensor and fabrication method thereof, World Patent, WO 2007/073111, 2007 Jun 28.

[102] S. Fardindoost, A.I. Zad, F. Rahimi, R. Ghasempour, Pd doped WO_3 films prepared by sol-gel process for hydrogen sensing, Int. J. Hydrogen Energ. 35 (2010) 854-860.

[103] S. Shukla, S. Seal, L. Ludwig, C. Parish, Nanocrystalline indium oxide-doped tin oxide thin film as low temperature hydrogen sensor, Sensor. Actuat. B: Chem. 97 (2004) 256-265.

[104] S. Shukla, P. Zhang, H.J. Cho, L. Ludwig, S. Seal, Significance of electrode-spacing in hydrogen detection for tin oxide-based MEMS sensor, Int. J. Hydrogen Energ. 33 (2008) 470-475.

[105] S. Seal, S. Shukla, L. Ludwig, C. Cho, inventors; University of Central Florida Research Foundation Inc., assignee. Room temperature hydrogen sensor, United States Patent, US 2010/0212403, 2010 Aug 26.

[106] C. Fischer, J.W. Menezes, S.A. Moshkalev, C. Verissimo, A.R. Vaz, J.W. Swart, Fabrication of high-aspect ratio silicon nanopillars and nanocones using deep reactive ion etching, J. Vac. Sci. Technol. B, 27 (2009) 2732-2736.

[107] K.J. Morton, G. Nieberg, S.F. Bai, S.Y. Chou, Wafer-scale patterning of sub-40 nm diameter and high aspect ratio (>50:1) silicon pillar arrays by nanoimprint and etching, Nanotechnology, 19 (2008) 345301.

[108] J. Ohara, K. Asami, Y. Takeuchi, K. Sato, Development of RIE-lag reduction technique for Si deep etching using double protection layer method, IEEJ Trans. Electr. Electr. 5 (2010) 125-130.

[109] J. Ohara, Y. Takeuchi, K. Sato, Improvement of high aspect ratio Si etching by optimized oxygen plasma irradiation inserted DRIE, J. Micromech. Microeng.

19 (2009) 095022.

[110] H. Rhee, H. Kwon, C.K. Kim, H. Kim, J. Yoo, Y.W. Kim, Comparison of deep silicon etching using SF_6/C_4F_8 and SF_6/C_4F_6 plasmas in the Bosch process, J. Vac. Sci. Technol. B, 26 (2008) 576-581.

[111] B.Q. Wu, A. Kumar, S. Pamarthy, High aspect ratio silicon etch: a review, J. Appl. Phys. 108 (2010) 051101.

[112] K. Wegner, P. Piseri, H.V. Tafreshi, P. Milani, Cluster beam deposition: a tool for nanoscale science and technology, J. Phys. D: Appl. Phys. 39 (2006) R439-R459.

[113] H.V. Tafreshi, P. Piseri, G. Benedek, P. Milani, The role of gas dynamics in operation conditions of a pulsed microplasma cluster source for nanostructured thin films deposition, J. Nanosci. Nanotechno. 6 (2006) 1140-1149.

[114] A.V. Singh, C. Lenardi, L. Gailite, A. Gianfelice, P. Milani, A simple lift-off-based patterning method for micro- and nanostructuring of functional substrates for cell culture, J. Micromech. Microeng. 19 (2009) 115028.

[115] P. Piseri, H.V. Tafreshi, P. Milani, Manipulation of nanoparticles in supersonic beams for the production of nanostructured materials, Curr. Opin. Solid St. Mater. Sci. 8 (2004) 195-202.

[116] P. Piseri, A. Podesta, E. Barborini, P. Milani, Production and characterization of highly intense and collimated cluster beams by inertial focusing in

supersonic expansions, Rev. Sci. Instrum. 72 (2001) 2261-2267.

[117] P. Milani, P. Piseri, E. Barborini, A. Podesta, C. Lenardi, Cluster beam synthesis of nanostructured thin films, J. Vac. Sci. Technol. A, 19 (2001) 2025-2033.

[118] M. Decarli, L. Lorenzelli, V. Guarnieri, E. Barborini, S. Vinati, C. Ducati, P. Milani, Integration of a technique for the deposition of nanostructured films with MEMS-based microfabrication technologies: application to micro gas sensors, Microelectron. Eng. 86 (2009) 1247-1249.

[119] E. Barborini, S. Vinati, M. Leccardi, P. Repetto, G. Bertolini, O. Rorato, L. Lorenzelli, M. Decarli, V. Guarnieri, C. Ducati, P. Milani, Batch fabrication of metal oxide sensors on micro-hotplates, J. Micromech. Microeng. 18 (2008) 055015.

[120] R.P. Feynman, R.B. Leighton, M. Sands, The Feynman lectures on physics, Addison-Wesley Publishing Company, Reading, 1964, pp. 32-7.

[121] W.P. Jakubik, Hydrogen gas-sensing with bilayer structures of WO_3 and Pd in SAW and electric systems, Thin Solid Films, 517 (2009) 6188-6191.

[122] T. Kida, T. Kuroiwa, M. Yuasa, K. Shimanoe, N. Yamazoe, Study on the response and recovery properties of semiconductor gas sensors using a high-speed gas-switching system, Sensor. Actuat. B: Chem. 134 (2008) 928-933.

[123] N. Matsuyama, S. Okazaki, H. Nakagawa, H. Sone, K. Fukuda, Response

kinetics of a fiber-optic gas sensor using Pt/WO_3 thin film to hydrogen, Thin Solid Films, 517 (2009) 4650-4653.

[124] C. Salinga, H. Weis, M. Wuttig, Gasochromic switching of tungsten oxide films: a correlation between film properties and coloration kinetics, Thin Solid Films, 414 (2002) 288-295.

[125] S. Shukla, S. Patil, S.C. Kuiry, Z. Rahman, T. Du, L. Ludwig, C. Parish, S. Seal, Synthesis and characterization of sol-gel derived nanocrystalline tin oxide thin film as hydrogen sensor, Sensor. Actuat. B: Chem. 96 (2003) 343-353.

[126] E. Washizu, A. Yamamoto, Y. Abe, M. Kawamura, K. Sasaki, Optical and electrochromic properties of RF reactively sputtered WO_3 films, Solid State Ionics, 165 (2003) 175-180.

[127] R. Sivakumar, C. Sanjeeviraja, M. Jayachandran, R. Gopalakrishnan, S.N. Sarangi, D. Paramanik, T. Som, Modification of WO_3 thin films by MeV N^+ ion beam irradiation, J. Phys. Condens. Mater. 19 (2007) 186204.

[128] T. Kubo, Y. Nishikitani, Deposition temperature dependence of optical gap and coloration efficiency spectrum in electrochromic tungsten oxide films, J. Electrochem. Soc. 145 (1998) 1729-1734.

[129] S.H. Lee, H.M. Cheong, P. Liu, D. Smith, C.E. Tracy, A. Mascarenhas, J.R. Pitts, S.K. Deb, Raman spectroscopic studies of gasochromic a-WO_3 thin films,

Electrochim. Acta, 46 (2001) 1995-1999.

[130] Y.P. He, Y.P. Zhao, Near-infrared laser-induced photothermal coloration in WO_3-H_2O nanoflakes, J. Phys. Chem. C, 112 (2008) 61-68.

[131] J.Y. Luo, S.Z. Deng, Y.T. Tao, F.L. Zhao, L.F. Zhu, L. Gong, J. Chen, N.S. Xu, Evidence of localized water molecules and their role in the gasochromic effect of WO_3 nanowire films, J. Phys. Chem. C, 113 (2009) 15877-15881.

[132] H.J. Chen, N.S. Xu, S.Z. Deng, D.Y. Lu, Z.L. Li, J. Zhou, J. Chen, Gasochromic effect and relative mechanism of WO_3 nanowire films, Nanotechnology, 18 (2007) 205701.

[133] W.B. Hu, Y.M. Zhao, Z.L. Liu, C.W. Dunnill, D.H. Gregory, Y.Q. Zhu, Nanostructural evolution: from one-dimensional tungsten oxide nanowires to three-dimensional ferberite flowers, Chem. Mater. 20 (2008) 5657-5665.

[134] S. Rajagopal, D. Nataraj, D. Mangalaraj, Y. Djaoued, J. Robichaud, O.Y. Khyzhun, Controlled growth of WO_3 nanostructures with three different morphologies and their structural, optical, and photodecomposition studies, Nanoscale Res. Lett. 4 (2009) 1335-1342.

[135] L. A. Currie, Nomenclature in evaluation of analytical methods including detection and quantification capabilities (IUPAC Recommendations 1995), Pure Appl. Chem. 67 (1995) 1699-1723.

[136] J. Li, Y.J. Lu, Q. Ye, M. Cinke, J. Han, M. Meyyappan, Carbon nanotube

sensors for gas and organic vapor detection, Nano Lett. 3 (2003) 929-933.

[137] C. Lu, Z. Chen, High-temperature resistive hydrogen sensor based on thin nanoporous rutile TiO_2 film on anodic aluminum oxide, Sensor. Actuat. B: Chem. 140 (2009) 109-115.

[138] J.W. Gong, J.R. Sun, Q.F. Chen, Micromachined sol-gel carbon nanotube/SnO_2 nanocomposite hydrogen sensor, Sensor. Actuat. B: Chem. 130 (2008) 829-835.

[139] S.J. Ippolito, S. Kandasamy, K. Kalantar-zadeh, W. Wlodarski, Hydrogen sensing characteristics of WO_3 thin film conductometric sensors activated by Pt and Au catalysts, Sensor. Actuat. B: Chem, 108 (2005) 154-158.

[140] G.N. Chaudhari, A.M. Bende, A.B. Bodade, S.S. Patil, V.S. Sapkal, Structural and gas sensing properties of nanocrystalline TiO_2:WO_3-based hydrogen sensors, Sensor. Actuat. B: Chem. 115 (2006) 297-302.

[141] E. Ghadiri, A. Iraji zad, F. Razi, Hydrogen sensing properties of pure and Pd activated WO_3 nanostructured films, Synth. React. Inorg. Me. 37 (2007) 453-456.

[142] K. Shimizu, I. Chinzei, H. Nishiyama, S. Kakimoto, S. Sugaya, H. Yokoi, A. Satsuma, Hydrogen sensor based on WO_3 subnano-clusters and Pt co-loaded on ZrO_2, Sens. Actuat. B: Chem. 134 (2008) 618-624.

[143] R. Ghasempour, A.I. Zad, Hybrid multiwalled carbon nanotubes and trioxide tungsten nanoparticles for hydrogen gas sensing, J. Phys. D: Appl. Phys. 42

(2009) 165105.

[144] W. Zeng, T.M. Liu, Hydrogen sensing characteristics and mechanism of nanosize TiO_2 dope with metallic ions, Physica B, 405 (2010) 564-568.

[145] A. Kolmakov, D.O. Klenov, Y. Lilach, S. Stemmer, M. Moskovits, Enhanced gas sensing by individual SnO_2 nanowires and nanobelts functionalized with Pd catalyst particles, Nano Lett. 5 (2005) 667-673.

[146] K. Mukherjee, S.B. Majumder, Hydrogen sensing characteristics of wet chemical synthesized tailored $Mg_{0.5}Zn_{0.5}Fe_2O_4$ nanostructures, Nanotechnology, 21 (2010) 255504.

[147] J. Jamnik, B. Kamp, R. Merkle, J. Maier, Space charge influenced oxygen incorporation in oxides: in how far does it contribute to the drift of Taguchi sensors, Solid State Ionics, 150 (2002) 157-166.

[148] B. Kamp, R. Merkle, J. Maier, Chemical diffusion of oxygen in tin dioxide, Sensor. Actuat. B: Chem. 77 (2001) 534-542.

[149] V.V. Sysoev, T. Schneider, J. Goschnick, I. Kiselev, W. Habicht, H. Hahn, E. Strelcov, A. Kolmakov, Percolating SnO_2 nanowire network as a stable gas sensor: direct comparison of long-term performance versus SnO_2 nanoparticle films, Sens. Actuat. B: Chem. 139 (2009) 699-703.

[150] H. Nakagawa, N. Yamamoto, S. Okazaki, T. Chinzei, S. Asakura, A room-temperature operated hydrogen leak sensor, Sensor. Actuat. B: Chem. 93 (2003)

468-474.

[151] P. Offermans, H.D. Tong, C.J.M. van Rijn, P. Merken, S.H. Brongersma, M. Crego-Calama, Ultralow-power hydrogen sensing with single palladium nanowires, Appl. Phys. Lett. 94 (2009) 223110.

[152] T.C. Arnoldussen, A model for electrochromic tungstic oxide microstructure and degradation, J. Electrochem. Soc. 128 (1981) 117-123.

[153] A. Georg, W. Graf, R. Neumann, V. Wittwer, The role of water in gasochromic WO_3 films, Thin Solid Films, 384 (2001) 269-275.

[154] S. Shukla, P. Zhang, H.J. Cho, S. Seal, L. Ludwig, Room temperature hydrogen response kinetics of nano-micro-integrated doped tin oxide sensor, Sensor. Actuat. B: Chem. 120 (2007) 573-583.

[155] Z.Z. Fang, H. Wang, Densification and grain growth during sintering of nanosized particles, Int. Mater. Rev. 53 (2008) 326-352.

[156] N. Izu, W. Shin, N. Murayarna, S. Kanzaki, Resistive oxygen gas sensors based on CeO_2 fine powder prepared using mist pyrolysis, Sensor. Actuat. B: Chem. 87 (2002) 95-98.

[157] K. Lu, Sintering of nanoceramics, Int. Mater. Rev. 53 (2008) 21-38.

[158] K.C. Park, D.Y. Ma, K.H. Kim, The physical properties of Al-doped zinc oxide films prepared by RF magnetron sputtering, Thin Solid Films, 305 (1997) 201-209.

[159] J.A. Thornton, The microstructure of sputter-deposited coatings, J. Vac. Sci. Technol. A, 4 (1986) 3059-3065.

[160] Y. Golan, L. Margulis, I. Rubinstein, Vacuum-deposited gold-films. 1: Factors affecting the film morphology, Surf. Sci. 264 (1992) 312-326.

[161] N. Martin, A.M.E. Santo, R. Sanjines, F. Levy, Energy distribution of ions bombarding TiO_2 thin films during sputter deposition, Surf. Coat. Tech. 138 (2001) 77-83.

[162] D.Y. Song, A.G. Aberle, J. Xia, Optimisation of ZnO:Al films by change of sputter gas pressure for solar cell application, Appl. Surf. Sci. 195 (2002) 291-296.

[163] J.P. Randin, R. Viennet, Proton diffusion in tungsten trioxide thin-films, J. Electrochem. Soc. 129 (1982) 2349-2354.

[164] W.C. Conner, J.L. Falconer, Spillover in heterogeneous catalysis, Chem. Rev. 95 (1995) 759-788.

[165] D. Martin, D. Duprez, Mobility of surface species on oxides. 1. Isotopic exchange $^{18}O_2$ with ^{16}O of SiO_2, Al_2O_3, ZrO_2, MgO, CeO_2, and CeO_2-Al_2O_3. Activation by noble metals. Correlation with oxide basicity, J. Phys. Chem. 100 (1996) 9429-9438.

[166] G. Vazquez, I. Gonzalez, Diffusivity of anion vacancies in WO_3 passive films, Electrochim. Acta, 52 (2007) 6771-6777.

[167] L.R. Merte, G.W. Peng, R. Bechstein, F. Rieboldt, C.A. Farberow, L.C. Grabow, W. Kudernatsch, S. Wendt, E. Lagsgaard, M. Mavrikakis, F. Besenbacher, Water-mediated proton hopping on an iron oxide surface, Science, 336 (2012) 889-893.

[168] J. Vondrak, J. Bludska, The role of water in hydrogen insertion into WO_3, Solid State Ionics, 68 (1994) 317-323.